INSTITUT FÜR
ENERGIETECHNIK
UND THERMODYNAMIK
Institute of Energy Systems and Thermodynamics

MEDIZINISCHE
UNIVERSITÄT WIEN

Master's Thesis

Multi-Stage vs. Single-Stage Rotodynamic Blood Pumps: Which Are More Suitable For Pediatric VADs?

under the supervision of

Assistant Prof. Dipl.-Ing. Bernhard Semlitsch
ap. Prof. Marcus Granegger, PhD
E302 - Institute of Energy Systems and Thermodynamics
Department of Cardiac Surgery

submitted to the Faculty of Mechanical and Industrial Engineering
of Technische Universität Wien
for the degree of Diplom-Ingenieur (Dipl.-Ing.)

by

Stefan Maric, BSc
Matr.Nr. 01431093

Statutory Declaration

This thesis is the result of my own work and includes nothing that is the outcome of work done in collaboration except as specified in the text.

It is not substantially the same as any that I have submitted, or, is being concurrently submitted for a degree or diploma or other qualification at Technische Universität Wien or any other university or similar institution except as specified in the text. I further state that no substantial part of my thesis has already been submitted, or, is being concurrently submitted for any such degree, diploma or other qualification at Technische Universität Wien or any other university or similar institution except as specified in the text.

Vienna, February 2024

. . [redacted]
(Stefan Maric, BSc)

Acknowledgements

First and foremost, I would like to express my gratitude to both of my supervisors Bernhard Semlitsch and Marcus Granegger, for not only providing support regarding the complex technical and medical questions but also guidance throughout the course of this thesis.

This thesis would not have been accomplished without the extensive help of Sarah Linnemeier and Bente Thamsen, by sharing their immense information and experience regarding their research and furthermore providing valuable help at any time. In this context, I want to thank every researcher I had contact with at the MUW for the countless conversations and the help that I received.

Special thanks deserves to be credited to my partner, Lucija, which supported me intensely throughout this journey and reignited my motivation when it was needed. I am also thankful for my family and friends, which showed consideration and support at all time.

Abstract

Objective The treatment of advanced heart failure in pediatric patients represents unique challenges, which are augmented by the limited options for suitable implantable Ventricular Assist Devices (VADs). The Medical University of Vienna is developing a new VAD solution for small pediatric patients that utilizes two pumping stages to build up the required pressure while decreasing the rotation rate. Hence, the circumferential speed is decreased, which may lower the shear stresses and expectably increase the hemocompatibility. The aim of this thesis is to evaluate the potential of a two-stage design by comparison with similar single-stage pumps.

Methods Two different single-stage pump concepts were designed and simulated, which are comparable to the two-stage pump (same specific speed/same diameter). These pumps operate with the same flow (Q_{2S}= 1.5 L/min) and build up a similar pressure head (H_{2S}= 54 mmHg) as the two-stage pump. Computational Fluid Dynamics (CFD) was employed to simulate the flow within each pump, using the results to iteratively refine each pump design. The simulation results were subjected to a mesh and time-step sensitivity study. Subsequent detailed CFD simulations on these refined designs provided insights into the shear stresses, normalized index of hemolysis (NIH), washout, and stagnation zones. The outcomes were compared to the results of the two-stage pump.

Results and Discussion The single-stage pumps generate similar pressure heads as the two-stage pump (H_1= 56 mmHg, H_2= 55 mmHg), but at lower efficiencies (η_1= 30%, η_2= 27% vs. η_{2S}= 32%). The occurring shear stresses reach higher magnitudes (up to 1600 Pa) than the two-stage pump. However, the volume of the two-stage pump is approximately 3 times larger than each single-stage pump.

The NIH in the single-stage pumps are higher (6.4 and 8.3 mg/100L) compared to the two-stage pump (3.7 mg/100L). The 90% washout of the single-stage pumps was achieved 2-3 times faster compared to the two-stage pump due to the lower volume. However, the detailed washout of the bearing should be subject to further examination in the future. Stagnation zones were only occurring at wall-near regions in all of the presented pump concepts.

Conclusion Despite a larger volume, the two-stage pump may have advantages in terms of hemolysis, NIH and washout. The lower hemolysis risk and NIH are attributable to the reduced shear stress magnitude, which is mainly caused by the lower circumferential speed of the impeller. The washout of the bearing geometry in the two-stage pump is advantageous, since a pressure gradient is present between both pump stages, which contribute to the enhanced washout. Therefore, the influence of the specific bearing design of the single-stage pumps need to be analyzed in more detail.

Kurzfassung

Ziel der Arbeit Die Behandlung von fortgeschrittener Herzinsuffizienz bei pädiatrischen Patienten, stellt eine besondere Herausforderung dar, welche durch die begrenzte Auswahl von geeigneten implantierbaren ventrikulären Unterstützungssystemen (VADs) verstärkt wird. Die Medizinische Universität Wien entwickelt eine neue VAD- Lösung für kleine pädiatrische Patienten, bei der zwei Pumpenstufen eingesetzt werden. Dabei wird der erforderliche Druck aufgebaut bei gleichzeitiger Verringerung der Rotationsgeschwindigkeit. Dadurch wird die Umfangsgeschwindigkeit des Rotors verringert, was die Scherspannungen verringert und somit die Hämokompatibilität erwartungsgemäß erhöht. Das Ziel dieser Arbeit ist es, die Vorteile eines zweistufigen Designs im Vergleich zu vergleichbaren einstufigen Pumpen zu bewerten.

Methodik Es wurden zwei unterschiedliche einstufige Pumpenkonzepte berechnet und konstruiert, welche mit der zweistufigen Pumpe vergleichbar sind (gleiche spezifische Drehzahl/gleicher Durchmesser). Diese Konzepte bauen bei gleichem Blutfluss (Q= 1,5 L/min) eine ähnliche Förderhöhe (H= 54 mmHg) auf. Mit Hilfe von numerischer Strömungsmechanik (CFD) wurde die Strömung in jeder Pumpe simuliert, und die Ergebnisse dienten zur iterativen Verbesserung des jeweiligen Pumpendesigns. Die anschließenden detaillierten CFD-Simulationen dieser verbesserten Entwürfe lieferten Erkenntnisse über die Scherspannungen, den normalisierten Hämolyse-Index (NIH), die Auswaschung und die Stagnationszonen. Diese Ergebnisse wurden folglich mit den Resultaten der zweistufigen Pumpe verglichen. Der Einfluss der Netzgröße, als auch des verwendeten Zeitschrittes auf die Simulationsergebnisse wurde überprüft.

Resultate und Diskussion Die einstufigen Pumpen erzeugen eine ähnliche Förderhöhe wie die zweistufige Pumpe (H_1= 56 mmHg, H_2= 55 mmHg), jedoch mit einem geringeren Wirkungsgrad (η_1= 30%, η_2= 27% vs. η_{2S}= 32%). Die auftretenden Scherspannungen erreichen höhere Werte (bis zu 1600 Pa) als bei der zweistufigen Pumpe. Die NIH Werte der einstufigen Pumpen sind höher (6,4 und 8,3 mg/100L) im Vergleich zur zweistufigen Pumpe (3,7 mg/100L). Die 90% Auswaschung der einstufigen Pumpen wurde im Vergleich zur zweistufigen Pumpe 2-3 mal schneller erreicht, was aufgrund des geringeren Volumens zu erwarten war. Die detaillierte Auswaschung der Lagergeometrie muss jedoch in Zukunft weiter untersucht werden. Stagnationszonen traten, wie bei der zweistufigen Pumpe, nur in wandnahen Bereichen auf.

Schlussfolgerung Trotz eines größeren Volumens, sind Vorteile der zweistufigen Pumpe in Bezug auf Hämolyse, NIH und Auswaschung zu sehen. Das geringere Hämolyserisiko und der NIH sind auf die geringeren Scherspannungen zurückzuführen, die vor allem durch die geringere Umfangsgeschwindigkeit des Laufrads verursacht wird. Die Auswaschung der Lagergeometrie in der zweistufigen Pumpe ist vorteilhaft, da zwischen den beiden Pumpenstufen ein Druckgefälle vorhanden ist, welches zur verbesserten Auswaschung beiträgt. Aus diesem Grund, muss der Einfluss der spezifischen Lagerkonstruktion der einstufigen Pumpen noch genauer untersucht werden.

Contents

1 Introduction **1**
1.1 Project background . . . 2
1.2 Scope of work . . . 4

2 Theory **5**
2.1 Hemocompatibility of RBPs . . . 5
2.1.1 Von Willebrand factor . . . 7
2.1.2 Platelets . . . 7
2.1.3 Red blood cells . . . 8
2.2 Pump theory . . . 10
2.2.1 Velocities . . . 13
2.2.2 Pump performance & efficiency curve . . . 14
2.2.3 Affinity laws, scaling & geometrical similarity . . . 14
2.2.4 Impeller types . . . 17
2.2.5 Cordier- diagram . . . 17
2.2.6 Pump design . . . 18
2.2.7 Bearing properties . . . 18
2.3 Computational fluid dynamics . . . 21
2.3.1 Mesh . . . 22
2.3.2 Simulation of rotating and static regions . . . 23
2.3.3 Discretization error of the simulation . . . 23

2.3.4 Simulating blood damage in RBPs 26

3 Materials and methods 28

3.1 Calculation of the design parameters 28

3.1.1 General design 29

3.2 CAD 32

3.3 CFD simulation 32

3.3.1 CFD geometry of the pump 32

3.3.2 Simulation setup 32

3.3.3 Pump efficiency 34

3.3.4 Shear stress and hemolysis 34

3.3.5 Washout and stagnation 36

3.4 Iterative approach 36

3.4.1 Concept 1 – identical specific speed and specific diameter . . 38

3.4.2 Concept 2 - equal impeller and volute geometry 51

3.5 Mesh independency 57

3.6 Time-step independency 60

4 Results 62

4.1 Pump design and performance 62

4.1.1 Concept 1 – identical specific speed and specific diameter . . 63

4.1.2 Concept 2 - equal impeller and volute geometry 64

4.2 Shear stress analysis 65

4.2.1 Concept 1 – identical specific speed and specific diameter . . 66

4.2.2 Concept 2 - equal impeller and volute geometry 69

4.3 Hemolysis and washout 74

4.3.1 Concept 1 – identical specific speed and specific diameter . . 74

4.3.2 Concept 2 - equal impeller and volute geometry 76

5 Discussion 82

5.1 Interpretation of the results 82
5.2 Limitations 84
5.3 Future work 85

6 Conclusion 86

Bibliography 88

A Berechnungsprogramm für Rotationsblutpumpen 96

Nomenclature

Abbreviations

BC	boundary condition
BEP	best efficiency point
CAD	computer aided design
CFD	computational fluid dynamics
GCI	grid convergence index
HF	heart failure
HJB	hydrodynamic journal bearing
HM III	HeartMate III
HVAD	HeartWare VAD
ILA	infinitely long approximation
ISA	infinitely short approximation
LIC	line integral convolution
MCS	mechanical circulatory support
MRF	Multiple Reference Frame
MUW	Medical University of Vienna
RANS	Reynold-Averaged Navier-Stokes
RBP	rotodynamic blood pump
VAD	ventricular assist device
vWF	von Willebrand factor

Physical Constants

g	Gravitational acceleration	$\mathrm{m/s^2}$

Latin Symbols

$\mathbf{S}$	mean strain rate tensor	$1/\mathrm{s}$
c	absolute velocity, radial clearance	$\mathrm{m/s}, \mathrm{\mu m}$

D	fraction of damaged erythrocytes	1
d	diameter	m
D_I	linear damage	1
d_q	specific diameter	1
e	eccentricity, blade thickness	$1, \mathrm{mm}$
e_a	approximate relative error	%
F_f	friction force	N
GCI	grid convergence index	%
H	pressure head	mmHg
h	height, mesh size, specific enthalpy	$\mathrm{mm}, 1, \mathrm{J/kg}$
Hb	total hemoglobin	g/L
L	length	m
$mgNIH$	normalized milligram index of hemolysis	mg/100L
N	number of cells	1
n	rotation rate, power constant	$\mathrm{rpm}, 1$
n_q	specific speed	1
O	center	1
P	power	W
p	pressure, apparent order	$\mathrm{Pa}, 1$
P_{loss}	power loss	W
Q	volume flow	L/min
q	correction factor	1
Q_{sp}	gap flow	L/min
R	radius	m
r	grid refinement factor	1
S	modulus of the mean strain rate tensor	1/s
s	sign factor	1
T	torque	$\mathrm{N/mm^2}$
t	time	s
V	volume	mL
W	load-carrying capacity	N
Y	specific work	J/kg
z	geodetic height	m
Z_h	hydraulic losses	m
z_{Bl}	number of blades	1
z_{st}	number of stages	1

ΔHb	plasma-free hemoglobin	g/L
$\dot{m}$	mass flow	kg/s
$\overline{W}$	dimensionless load	1

Greek Symbols

α	hemolysis parameter	1
β	blade angle, hemolysis parameter	°, 1
ϵ	difference	1
ϵ_{hub}	inclination angle	°
η	efficiency	1
λ	relaxation time	s
μ	dynamic viscosity	Pa s
μ_0	zero shear viscosity	Pa s
μ_∞	infinite shear viscosity	Pa s
ν	kinematic viscosity	m^2/s
ω	angular velocity	1/s
Φ	variables mesh independency	1
ψ	angle of the minimum gap height	°
ρ	density	kg/m^3
τ	shear stress	N/mm^2
ε	eccentricity ratio	1

Vectors and Tensors

$\vec{\bar{v}}$	mean velocity
$\vec{c}$	absolute velocity
$\vec{u}$	circumferential velocity
$\vec{w}$	relative velocity
$\vec{y}$	position
$\frac{d\vec{v}}{d\vec{y}}$	velocity gradient

Subscripts

min	Minimum

Chapter 1

Introduction

According to recent observations, 26 million people worldwide suffer from heart failure (HF), which is a medical condition, characterized by the impeded function of the heart to pump enough blood through the circulatory system [1]. Heart failure impacts individuals of all ages, including adults and children. In children, HF is primarily caused by dilated cardiomyopathy, congenital heart disease and myocarditis [2]. In the US, 18 of 100.000 children are hospitalized with HF [3]. Additionally, the mortality rate of pediatric patients hospitalized with HF is with 7.7% higher than for adult patients with 5.6% [4].

The state-of-the-art therapy for advanced HF is heart transplantation [5]. However, the demand for donor organs exceeds the supply, which can impede timely treatment [6]. Mechanical circulatory support (MCS) devices such as ventricular assist devices (VADs) are used to bridge these waiting periods and are nowadays also established as destination therapy [7]. Ventricular assist devices support the function of a single ventricle of the heart by mechanically inducing a pressure gradient and blood flow [8, 9]. First generation VADs mimic the physiological heart function by providing a pulsatile flow. However, today's state-of-the-art devices for adult patients are rotodynamic blood pumps (RBPs), which provide a continuous flow [8]. These devices are overall more reliable, smaller in size and need less power to operate (see Figure 1.1) [8, 10].

Specifically, in pediatrics, however, there is a lack of implantable VADs that have proven to be a reliable bridge-to-transplant solution. In present, only the HeartMate III and the Berlin Heart EXCOR are approved for the treatment of pediatric patients [2, 11]. However, the HeartMate III was primarily designed

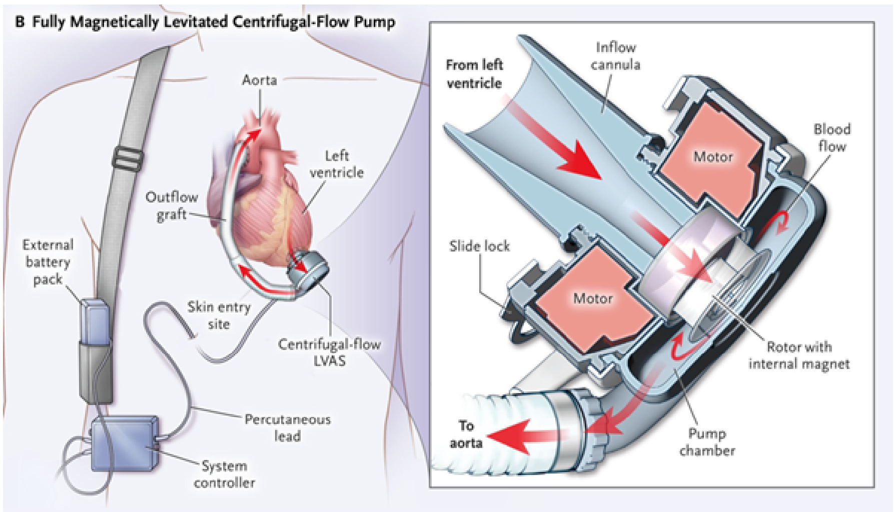

Figure 1.1: Illustration of an implanted HeartMate III with a detailed cross-sectional view of the pump [15].

for adult patients and can therefore only support older children (>8 years), since the size and the flow of the pump are overdesigned for small pediatric patients [12]. The Berlin Heart EXCOR utilizes pump sizes from 10-60 ml to support small pediatric patients as a bridge-to-transplant solution. In contrast to the HeartMate III, which is an implantable device with continuous flow, the Berlin Heart EXCOR is a paracorporeal system, which provides a pulsatile blood flow [12, 13]. In a paracorporeal system, the blood pump is located outside the body and is connected to the heart and blood vessels via cannulas and tubes. However, patients weighing less than 10 kg who have been treated with this system have a mortality rate of 38% [13]. In addition, this system is associated with the hospitalization of the patient, since the mobile unit of the Berlin Heart EXCOR can only be used with the larger pump sizes of 50 and 60 ml [14]. Therefore, further development of implantable VADs, specifically for small pediatric patients, is needed.

1.1 Project background

The Medical University of Vienna (MUW) is developing a new VAD solution for small pediatric patients. Currently, a novel multi-stage RBP utilizing two stages is being developed as an implantable VAD for this specific patient group. The design of this pump is visualized in Figure 1.2. This pump, set at rotation rate of 6400 rpm, is expected to generate a pressure head of 54 mmHg with an impeller diameter of 11 mm and an efficiency of 32%. The pump entails a blood volume of 3.7 mL, while continuously providing a blood flow of 1.5 L/min. The impeller is powered by an electric motor and fully levitated within the blood inside the housing. The impeller is suspended in radial direction through a hydrodynamic journal bearing and is axially centered through reluctance forces of the motor.

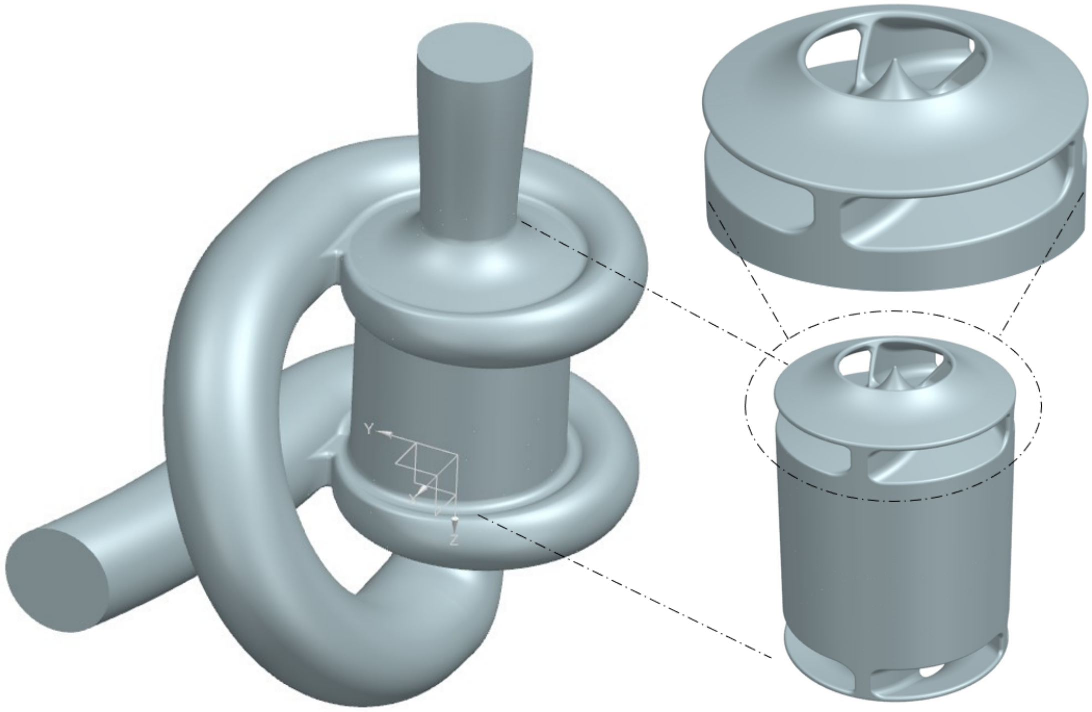

Figure 1.2: 3D- CAD design of the two-stage pump with the pump housing on the left side and the impeller on the right side.

Such multi-stage rotodynamic pumps are designed with more than one impeller, which are stacked in series on a single shaft (see Figure 1.3). Each impeller adds energy to the fluid, resulting in increased pressure as the fluid progresses through the stages without the need of an increase in rotation rate compared to single-stage pumps [16]. Therefore, the idea of a multi-stage RBP is expected to result in less blood damage, since the circumferential velocity of the impeller can be reduced while maintaining the needed pressure head.

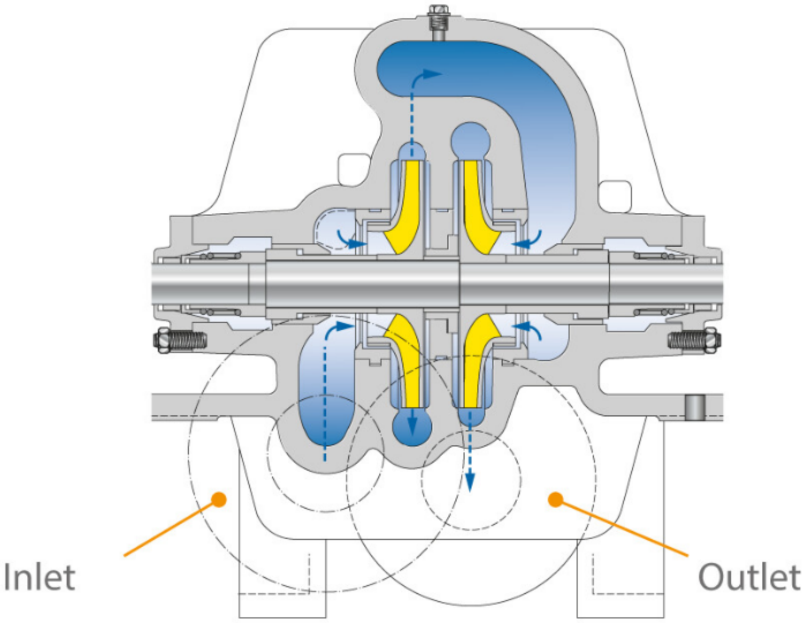

Figure 1.3: Schematic illustration of a two-stage centrifugal pump in a back-to-back configuration [17].

1.2 Scope of work

The objective of this master thesis is to calculate, design and simulate single-stage RBPs to compare to and thus estimate the potential benefits of a two-stage design. Two individual pump concepts are being developed, which utilize different approaches to ensure a comparability with the two-stage pump. The first concept is based on the application of the scaling laws and the geometrical similarity of rotodynamic pumps. For the second single-stage concept, the impeller and volute geometry remain identical as within the two-stage pump, only the rotation rate and the blade angle are adjusted for a comparable pump output.

This thesis begins with the necessary information to understand the complex engineering, biomechanics, and clinical aspects of RBPs, as well as an introduction into numerical modeling of fluid flow. Following this theoretical foundation, the document explains the methods used to achieve the research goal and presents the results. Lastly, a detailed discussion of all gathered data is provided, along with a glimpse into the future of pediatric VADs.

Chapter 2

Theory

The objective of RBPs is to provide a specific blood volume flow Q and a specific pressure head H while ensuring hemocompatibility. Currently, the design of the impeller and volute geometry are based on the theoretical principles of rotodynamic pumps. Furthermore, computational fluid dynamics (CFD) simulation provides information on the pump performance, velocity profiles and shear stresses. The evaluation of the simulation results is indispensable to observe the efficiency of the pump as well as the flow characteristics affecting the hemocompatibility and blood damage (e.g., shear stress, velocity) [18–20].

In the upcoming chapter, the significance of hemocompatibility in RBPs is discussed, followed by the overall structure and function of rotodynamic pumps, emphasizing the concept of geometrical similarity. Additionally, a detailed account of the fluid flow simulation using CFD is presented.

2.1 Hemocompatibility of RBPs

A major aim of RBPs is to convey blood, which consists of liquid blood plasma and solid cell components, while ensuring hemocompatibility [21]. The bloods solid components are erythrocytes, leukocytes, and thrombocytes. The latter are often referred to as platelets. Furthermore, a fraction of the blood plasma consists of solid components, such as proteins, coagulants, electrolytes and immunoglobulin [22]. All these solid cell components are prone to degradation or functional impairment due to mechanical stresses. The term hemocompatibility describes the altered immunologic, inflammatory and hematologic behavior of the blood when it comes into contact with a foreign material or device [23]. This interaction also has the capability to excite the blood coagulation cascade, which increases thrombus formation [21]. The blood coagulation cascade is a series of enzymatic reactions which lead to clotting of the blood, usually needed by the organism to repair injured blood vessels [24]. The leading mechanism behind the blood coagulation is called hemostasis [25] However, the formation of blood clots (thrombosis) in RBPs is not desired, due to the possibility of congesting veins and arteries or causing pump thrombosis [9, 26]. The event of pump thrombosis describes the presence of a thrombus inside the device, which can impede the function of the impeller or congest the inlet or outlet of the blood pump [26].

In general, thrombosis is affected by three separate factors, also known as the Virchow's triad: surface interaction, blood flow characteristic and altered blood coagulability (see Figure 2.1) [27, 28]. Specifically, in RBPs, the surfaces are made of foreign material, the blood flow is following non-physiological patterns and the blood coagulability is modified [20]. The non-physiological flow patterns of the blood inside such pumps refer to zones with stagnant, slow, turbulent, and recirculating flow [20, 29].

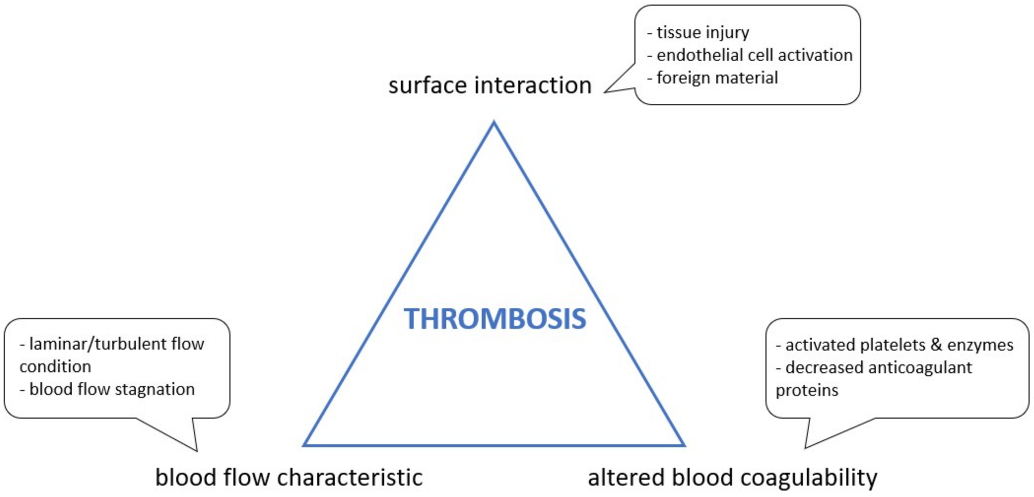

Figure 2.1: Illustration of the Virchow's trias with examples to each factor affecting thrombosis.

Blood damage refers to the trauma of the blood cells and proteins induced by mechanical stress. Hemolysis, platelet activation, modification of the coagulation cascade, thromboembolism as well as the reduction of the functionality of the white blood cells and the destruction of the von Willebrand factor (vWF), which are explained in the following sections, are regarded as blood damage. Not only the magnitude of the shear stress, but also the exposure time of the cells is important for the classification of the level of blood damage [9].

Since the different blood components exhibit different mechanical properties, the damaging effect to each component is observed separately [9]. In the following, the known damaging effects to three components of the blood are described. It should be noted that the following shear stress thresholds originate from simplifications, since the effect of the exposure time is not considered.

2.1.1 Von Willebrand factor

The vWF is an important protein for hemostasis, which can be found in the blood plasma as large multimers. Its task is the platelet and subendothelial collagen adhesion, and the regulation of the blood coagulation cascade. The shape of the vWF multimer is considered to unfold as a result of shear stress in the circulation, exposing the cleavage sites hence increasing its vulnerability to proteolysis. This reduces the amount of large vWF multimers in the blood and leads to bleeding disorders [30]. Aortic stenosis and MCS devices (e.g. VADs) are thought to increase the effect of proteolysis of the vWF, because the blood is exposed to higher shear stresses compared to the normal circulation [9].

The information about the threshold of shear stress leading to destruction of vWF multimer chains is limited. However, Fraser et al. analyzed the mechanical blood damage in rotary VADs and associated shear stresses above 9 Pa to an increased degradation of the vWF [9].

2.1.2 Platelets

Platelets are important cells for thrombus formation and hemostasis. They are activated if blood vessels are damaged and repair the damage by adhering to the injured location. In this process, the activated platelets are binding with collagen and vWF to form clots and heal the damaged injury [31]. These platelets, however, have the ability to be activated by either mechanical or chemical stimuli. The platelets are constantly deformed (stretched, compressed and sheared) while

being transported in the cardiovascular system and the use of RBPs are applying additional shear stresses which can lead to undesired activation. The activation of platelets leads to multiple processes which result in blood clotting [32].
Studies analyzed the shear stress – exposure time dependency on the activation of platelets. Hellums [33] shows that the platelet activation threshold is both shear stress and exposure time dependent. The behavior follows a consistent curve. Fraser et al. [9] summarized the results of similar studies in a diagram (see Figure 2.2). Since the velocities of the blood flow in VADs result in an exposure time around 0.1 seconds, Fraser et al. analyzed the flow field with regard to possible mechanical activation of platelets at shear stresses above 50 Pa [9].

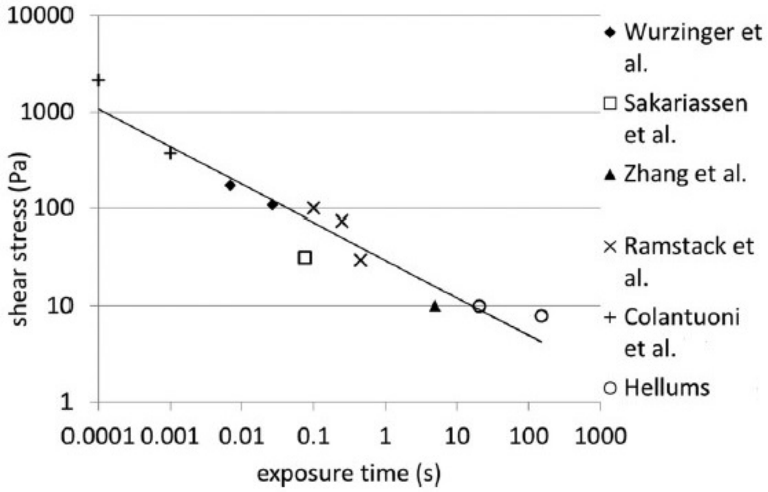

Figure 2.2: Shear stress - exposure time threshold behavior for platelet activation [9]

2.1.3 Red blood cells

Erythrocytes (red blood cells) can store gases and nutrients, and transport them through the cardiovascular system [34]. Damage to those cells is called hemolysis, which may result in the stored hemoglobin to leak into the blood plasma. This ultimately alters the function of erythrocytes and shortens their lifespan [35]. Hemolysis can occur due to the the exposure of mechanical shear stress, which deforms the cell and creates pores or ruptures the erythrocyte membrane [36]. Figure 2.3 shows a schematic view of the erythrocytes in different deformation arrangements.

The hemolysis risk in RBPs is the highest at the blades of the impeller, the volute cutwater, as well as in the gaps between the rotating impeller and the stationary pump housing, since the highest shear stresses occur in these regions. Parameters like the circumferential velocity, impeller diameter and length, as well as the exposure time are influencing the level of hemolysis in a RBP [37]. Another factor contributing to hemolysis is the interaction of the erythrocytes with foreign material [38].

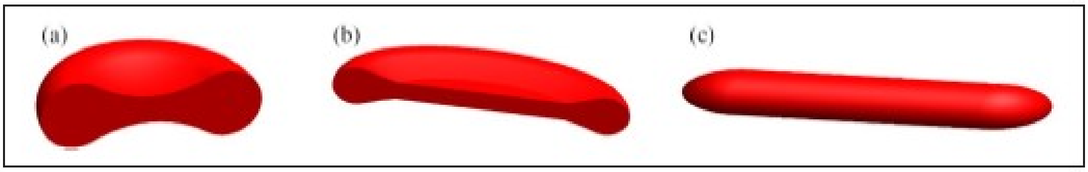

Figure 2.3: 3D illustration of an erythrocyte in the (a) undeformed state, (b) slightly deformed and elongated state and (c) stretched state before rupturing [35].

Various researchers observed the influence of shear stress and its duration of exposure leading to hemolysis [35]. Emerging from this research, a prediction for the hemolysis index

$$HI = \frac{\Delta Hb}{Hb} = D(\tau, t) = A * t^{\alpha} * \tau^{\beta} \tag{2.1}$$

was derived in a power law, which states the relation of plasma-free hemoglobin ΔHb and total hemoglobin Hb. In equation 2.1, the influence of the exposure time t (s) and the shear stress τ (Pa) on the hemolysis index is visible [39]. The research groups studying blood damage adjusted the empirically determined parameters A, α, and β, to ensure that the computed level of hemolysis aligns with the experimentally measured values. The experiments of Heuser and Opitz [40] correlated with the calculated hemolysis index from equation 2.1, with $A = 1.8 * 10^{-6}$, $\alpha = 0.765$ and $\beta = 1.991$. Consequently, the level of hemolysis is more sensitive to the magnitude of the shear stress, since its exponent β is higher than the exponent of the time variable α [41]. However, the significance of this power law in equation 2.1 has its limitations since it was derived from data gathered by Couette flow experiments. Nevertheless, it is used to assess first data on hemolysis for engineering purposes [42]. Specific standardized relations were introduced to assess the blood damage of medical devices in general [39]. Among these relationships is the normalized milligram index of hemolysis (mgNIH), quantifying the rise in plasma-free hemoglobin in milligrams per 100 liters of pumped blood [43]. The $mgNIH$

$$mgNIH = Hb * D(\tau, t) * 100 * 1000 \tag{2.2}$$

can be calculated numerically, by using the concentration of total hemoglobin Hb and the fraction of damaged erythrocytes $D(\tau, t)$ from equation 2.1 [39]. A normal Hb level in adults ranges from 120-180 g/L [44].
Another observation focuses on the typical exposure times in VADs. As stated before, the flow velocities in VADs lead to an exposure time of about 0.1 seconds. The critical shear stresses in this range of exposure duration that lead to hemolysis are above 150 Pa [45].

2.2 Pump theory

The fundamental design principles of rotodynamic pumps, as studied by Gülich [16] or Stepanoff [46], are used to create concepts for RBPs since the method of operation is the same [20]. The aim of rotodynamic pumps is to transport a fluid with a certain volume flow at a specific pressure level. Inside the fluid filled pump, an impeller is rotating and consequently conveying the fluid from the inlet (suction side) to the outlet (pressure side). In this process, the fluid gets accelerated, deflected and decelerated while the rotating impeller transfers energy to the fluid. Figure 2.4 shows the cross-sectional view of a pump with denotations for a more detailed description [16].

Therefore, the mechanical energy generated by a motor with a power

$$P_m = T_m * 2 * \pi * n_m \tag{2.3}$$

is transferred to the conveyed fluid and transformed into kinetic and potential energy by the impeller. The motor's torque T_m and rotation rate n_m are governed by the power. The transfer of power from the motor to the pump impeller is accompanied by mechanical losses, thus the mechanical efficiency

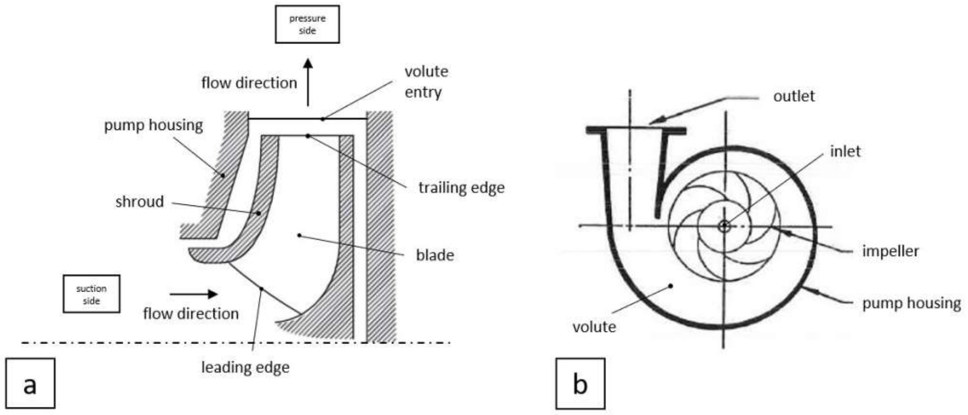

Figure 2.4: Illustrative views of a centrifugal pump with the labeled main components: (a) cross-sectional view (b) top view, modified from [16, 46].

$$\eta_m = \frac{P_h}{P_m} \tag{2.4}$$

has to be considered. The theoretical hydraulic power P_h of the pump further describes the theoretical specific work

$$Y_{th} = \frac{P_h}{\dot{m}} = \frac{P_h}{Q * \rho} \tag{2.5}$$

in combination with the fluid mass flow $\dot{m}$. This parameter has significant importance to rotodynamic pumps and describes the total energy transmitted to the fluid per unit mass. In rotodynamic pumps, the energy transmitted to the fluid

$$Y_{th} = \frac{\Delta \mathrm{p}_v}{\rho} + \frac{p_p - p_s}{\rho} + \frac{c_p^2 - c_s^2}{2} + g\left(z_p - z_s\right) = \ h_p - h_s \tag{2.6}$$

can be calculated, where $\frac{\Delta \mathrm{p}_v}{\rho}$ represent the hydraulic losses, $\frac{p_p - p_s}{\rho}$ the pressure energy, $\frac{c_p^2 - c_s^2}{2}$ the kinetic energy and $g\left(z_p - z_s\right)$ the potential energy between the pressure side (index “p”) and the suction side (index “s”). Here, p represents the pressure, c the absolute velocity, z the geodetic height, g the gravitational acceleration and ρ the density of the fluid. Equation 2.6 is derived from the Bernoulli equation with additional terms for the enthalpy h, since in rotodynamic pumps the energy level is usually increased along the streamline. However, the hydraulic losses are assumed to be zero for the theoretical specific work Y_{th} [16, 46].

Specifically in blood pumps, the height differences are usually of a small magnitude and therefore negligible. Furthermore, the velocities c_p and c_s are approximated to be equal, since the flow leaving the impeller of the pump is gradually decelerated in the following guide apparatus. These approximations show that the theoretical specific work Y_{th} in blood pumps is only depending on the pressure energy. Finally, the flow exiting the impeller gets guided to the pump outlet by the volute, which gradually decelerates the flow and transforms the kinetic energy to static pressure (see Figure 2.4b). The volume flowing out of the impeller is split at the volute cutwater, which separates the flow into a part flowing in the guide vane and a part flowing towards the pump outlet. The optimal design of the volute cutwater matches the angle of the approaching flow. A mismatch could lead to undesired losses [16].

The fluid is subject to pressure losses in this guiding process, which can occur due to friction or vortex dissipation. These losses are influencing the hydraulic efficiency

$$\eta_h = \frac{Y}{Y_{th}} = \frac{Y}{Y + Z_h * g} \tag{2.7}$$

of the pump, and therefore the magnitude of the head H. Z_h is the sum of all hydraulic losses between the pressure side and suction side [16, 20, 46].

In general, the pump performance is described by the head

$$H = \frac{Y}{g} \ , \tag{2.8}$$

which is calculated by the division of the specific work Y with the acceleration of gravity g. Observing blood pumps and their assumptions for energy transformation, the theoretical head

$$H_{th} = \frac{p_p - p_s}{\rho * g} \tag{2.9}$$

depends on the pressure difference between pressure side and suction side, fluid density ρ and acceleration of gravity g. To describe pressures in the cardiovascular system, the head is usually given in millimeters of mercury (mmHg) [16, 20].

2.2.1 Velocities

The fluid is being moved through the pump, as a reaction to the mechanical interaction with the rotating impeller. In rotodynamic pumps, the velocities of the moving fluid can be defined in a relative and an absolute system. Therefore, the circumferential velocities $\vec{u}$ of the pump impeller, the absolute velocities $\vec{c}$ as well as the relative velocities $\vec{w}$ of the flow are observed. The circumferential velocity depends on the rotation rate n and the dimension of the impeller, while the relative velocity is being observed in a rotating reference frame and the absolute velocity

$$\vec{c} = \vec{u} + \vec{w} \tag{2.10}$$

is the sum of the two vectors. They can be geometrically mapped in a velocity triangle (see Figure 2.5), which shows the relation between the present velocities [16].

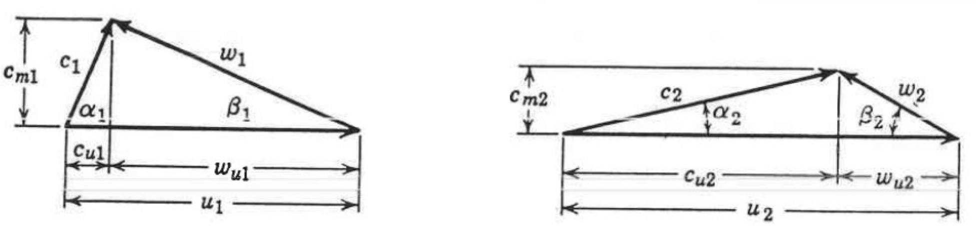

Figure 2.5: Typical velocity triangles of rotodynamic pumps (index "1" describes blade channel entry, "2" blade channel exit) [46].

The energy of the rotating impeller is governing the magnitude of the generated flow velocities. Therefore, the specific work of the impeller can be described by the velocities in the moving fluid

$$Y_{th} = u_2 c_{u2} \text{-} u_1 c_{u1}. \tag{2.11}$$

Equation 2.11 is called the “Euler’s turbine equation”, which assumes the conservation of momentum in the pumping process. The parameters $u_{1,2}$ are the circumferential velocities of the impeller at the entry “1” and exit “2”, whereas $c_{u,1,2}$ are the projected absolute velocities in the plane of the respective circumferential velocity (please see Figure 2.5). The geometrical relationship of the velocity triangle leads to the specific work

$$Y_{th} = \frac{1}{2} * \left(u_2^2 - u_1^2 + w_1^2 - w_2^2 + c_2^2 - c_1^2\right) \ , \tag{2.12}$$

being only dependent on the three velocity components. Firstly, the centrifugal part $u_2^2 - u_1^2$, secondly the reduction in relative velocity $w_1^2 - w_2^2$ and lastly the increase in absolute velocity $c_2^2 - c_1^2$. The exiting velocity c_2 is further decelerated while being guided to the pump outlet [16].

2.2.2 Pump performance & efficiency curve

The generated head H of a pump over the volume flow Q at constant rotation rate n is depicted in the pump performance curve (see Figure 2.6). Figure 2.6a shows the deviation of the real HQ curve from the Euler pump curve due to friction, recirculation, and leakage losses. The conceptual design of rotodynamic pumps can only be optimized for a specific operating point on the performance curve, which usually resembles the best efficiency point (BEP) [16, 20].
Another way to visualize the performance of a specific pump design at different operating points, which are defined by the pressure head H an the volume flow Q, is the pump efficiency curve. The efficiency η is calculated at various operating points and depicted over the range of the volume flow Q [16, 20]. Figure 2.7 shows an example of a pump performance curve (pressure head curve) and pump efficiency curve for a RBP [47].

2.2.3 Affinity laws, scaling & geometrical similarity

The pump performance curve also shows a scaled behavior of a pump at different rotation rates n, which is governed by the affinity laws. These laws state, that the volume flow Q is directly proportional to the rotation rate n and the head H is proportional to the square of the rotation rate n

$$\frac{Q_1}{Q_2} = \frac{n_1}{n_2} \quad , \quad \frac{H_1}{H_2} = \frac{n_1^2}{n_2^2}, \tag{2.13}$$

which is also shown in Figure 2.6b [46].

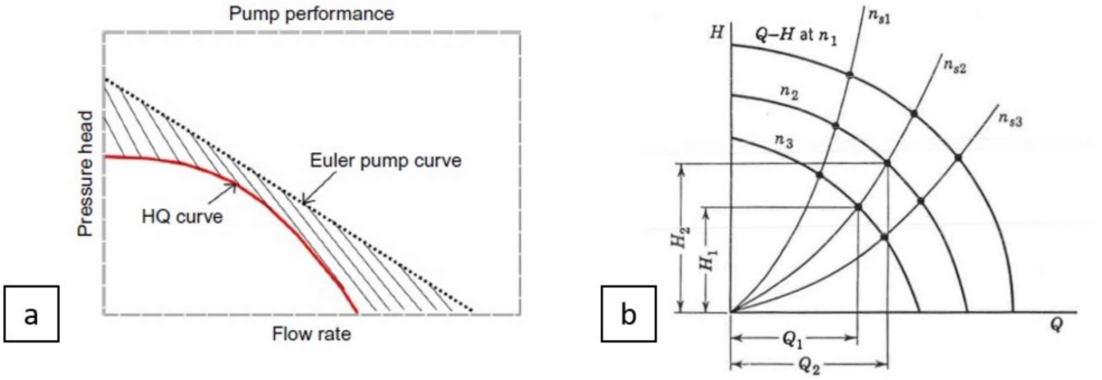

Figure 2.6: Pump performance curve (a) with the impact of hydraulic losses and (b) with different rotation rates n, modified from [20] S 317; [46] S 26.

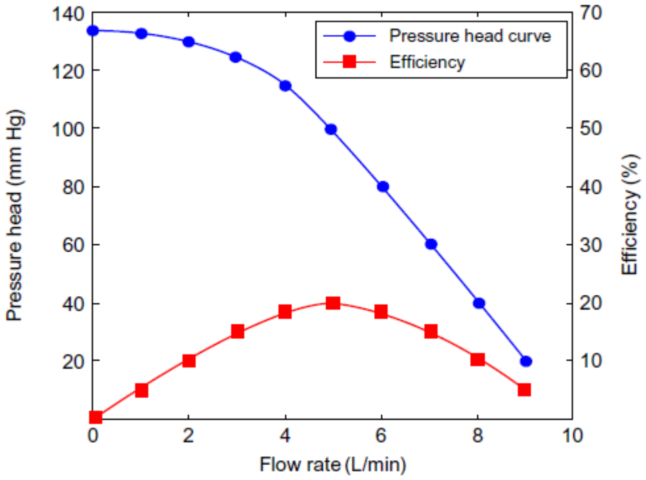

Figure 2.7: Exemplary pump performance and efficiency curve of a RBP [47].

Another application of the affinity laws is the scaling of pumps. In this case, the diameter, the number of stages and the efficiency of the model pump, as well as the scaled version, are included. However, the efficiencies of the observed pumps are generally approximated to be of the same magnitude [16]. Therefore, the affinity laws are extended by the outer impeller diameter d_2 (see Figure 2.8) and the number of pump stages z_{st} of the model pump (M) or scaled version (S), respectively, forming the following equations:

$$H_S = H_M * \left(\frac{n_S}{n_M}\right)^2 * \left(\frac{d_{2,S}}{d_{2,M}}\right)^2 * \frac{z_{st,S}}{z_{st,M}} \tag{2.14}$$

$$Q_S = Q_M * \frac{n_S}{n_M} * \left(\frac{d_{2,S}}{d_{2,M}}\right)^3. \tag{2.15}$$

The combination of Equation 2.14 and 2.15 resulted in the introduction of the specific speed n_q

$$n_q = n * \frac{\sqrt{Q}}{(H/z_{st})^{0.75}}, \tag{2.16}$$

which is a parameter used to choose the impeller type and pump design. Furthermore, the aforementioned equations lead to the specific diameter d_q

$$d_q = d_2 * \frac{(H/z_{st})^{0,25}}{\sqrt{Q}}, \tag{2.17}$$

that combined with the specific speed is used for scaling. The units used in equation 2.16 and 2.17 are n in rpm, d in m, Q in m^3/s and H in m. Pumps that share equal specific speed n_q and diameter d_q exhibit geometrical similarity [16].

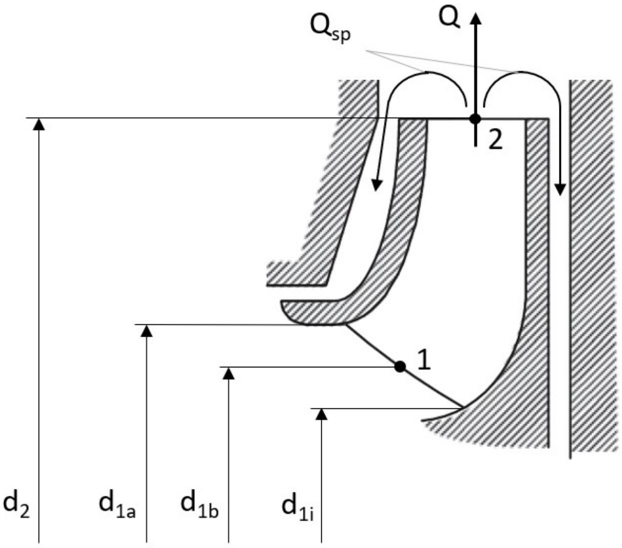

Figure 2.8: Cross-sectional view of a pump impeller with diameter measurements, volume flow and gap flow, modified from [16].

2.2.4 Impeller types

In general, pumps are classified by various aspects, such as the operation principle, impeller type or the guide apparatus. The impeller type ultimately defines the pump's fluid flow direction. Common rotodynamic pumps are either radial, semi-axial or axial, depending on the head and volume flow of the pump operation, as well as the pumps rotation rate. Consequently, the specific speed is used to classify the different impeller types, since it combines all the influencing parameters. Table 2.1 provides the information on the typical ranges of specific speed for each impeller type [16]. However, another influencing factor of the impeller shape is the overall pump design, which is mostly predetermined by the application area.

Table 2.1: Difference in pump types depending on the specific speed [16].

$\mathbf{n_q}$	**pump type**	**impeller shape**
7-100	radial	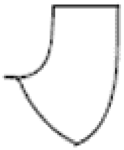
35-160	semi-axial	
160-400	axial	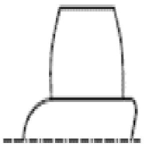

2.2.5 Cordier- diagram

The Cordier- diagram shows the relation of a pump's efficiency η, its specific speed n_q and specific diameter d_q. Otto Cordier experimented with different kinds of turbomachines, including pumps and turbines, and determined their respective operating point of highest efficiency. The specific speed and diameter of each turbomachine calculated in the operating point with highest efficiency were finally illustrated in a diagram (see Figure 2.9). According to Cordier, every point inside the ribbon-shaped area (in Figure 2.9 colored in blue for pumps) has a combination of specific speed and diameter, which represents a pump design with best efficiency.

Moreover, the efficiency η can be expected to be nearly the same for a group of turbomachines, which fulfill the conditions for geometrical similarity (same specific speed n_q and specific diameter d_q). Additionally, the impeller shapes are represented in the diagram, matching the previously mentioned range for their respective specific speeds in Table 2.1. Thus, the Cordier– diagram helps the pump designer to choose an optimal design [48, 49].

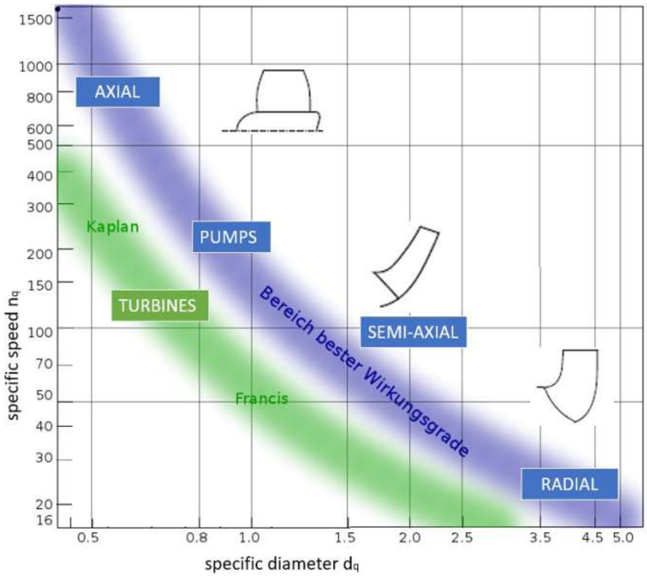

Figure 2.9: Cordier- diagram for pumps and turbines, modified from [16, 49].

2.2.6 Pump design

The prediction of performance during the design of a rotodynamic pump is based on empirical approximations and assumptions that lead to uncertainties [16, 20]. Further information on the calculation of rotodynamic pumps can be found in Appendix A.

2.2.7 Bearing properties

In general, there are different bearing types to hold the rotating impeller in the stationary pump housing. For rotodynamic pumps either mechanical, hydrodynamic, or magnetic bearings are used [16]. The latest RBPs use hydrodynamic or magnetic bearings, or a combination of both, to fully levitate the impeller inside the pump housing [50].

Since a hydrodynamic journal bearing (HJB) is used in the two-stage pump, it should also be adapted in the single-stage pump concepts. In a radial HJB, the rotating shaft (journal) is located inside a cylindrically shaped body (bearing) with a radial clearance c separating both surfaces (see Figure 2.10) [51]. This clearance gap is filled with a fluid [52]. When the shaft starts to rotate, the fluid causes a hydrodynamic lift force onto the rotating shaft which separates it from the stationary pump housing [50].

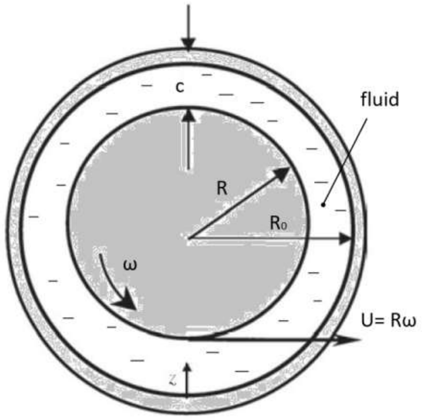

Figure 2.10: Illustration of a hydrodynamic journal bearing, modified [51].

The operation state of an HJB is dependent on the interaction of the bearing geometry, the angular velocity ω, and the dynamic viscosity of the fluid μ. The parameters defining the bearing geometry are the radius of the rotating shaft R, the radial clearance c, and the bearing length L. During rotation, the shaft moves relative to the pump housing. The location of the shaft center O_j relative to the bearing center O_b is defined by the eccentricity e, the angle ψ, and the resulting minimum radial clearance c_{min}, exemplary shown in Figure 2.11 [51].

A hydrodynamic journal bearing has the ability to endure a specific force W, which is commonly referred to as the load-carrying capacity. The calculation of this force is based on some assumptions. Firstly, the ratio of the bearing length L and the diameter d ($d = 2 * R$) defines if the infinitely long approximation (ILA) or the infinitely short approximation (ISA) can be used, to analytically calculate the load-carrying capacity. In general, ILA is providing results of acceptable accuracy if $L/d > 2$, else ISA is used. Secondly, the bearing design leads to assumptions about the boundary conditions (BC). The lubricating fluid film is either assumed to be distributed equally along the bearing length even at the edges and the regions of negative pressure in the bearing being considered (full Sommerfeld BC), or it is assumed that the fluid film decreases towards the edges of the bearing, the bearing being open to ambient pressure and neglecting the negative pressure (half Sommerfeld BC) [51, 53].

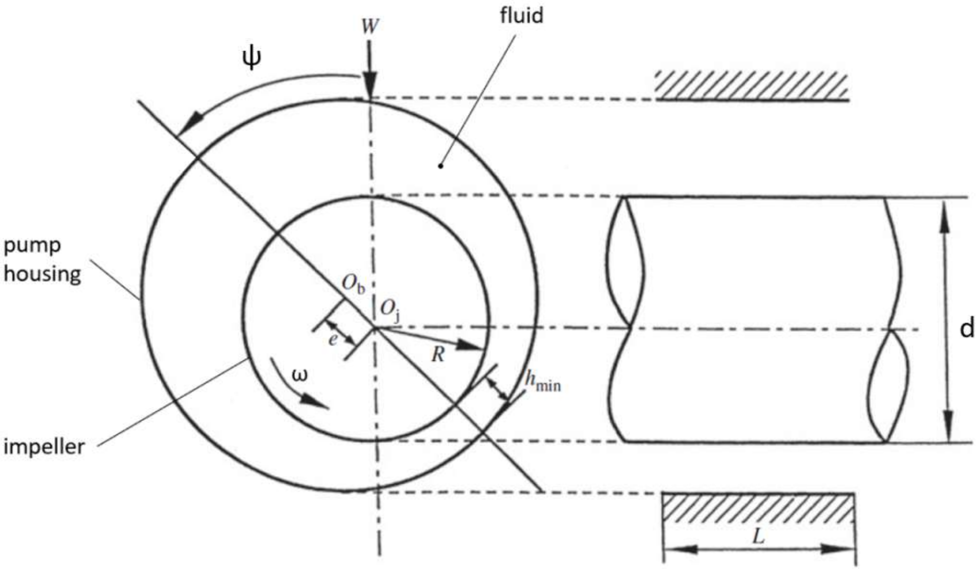

Figure 2.11: Example of a hydrodynamic journal bearing in operation with an eccentricity e, modified [51].

In addition to the two-stage pump, the bearings used in RBPs, are generally designed as short bearings with $L/d < 1$ [53, 54]. Therefore, the following calculation is derived by applying the ISA to the governing equations. Furthermore, the full Sommerfeld BC is assumed since the impeller of the pump is fully surrounded by blood as the lubricating medium [51]. As a result, the load-carrying capacity W is calculated as follows:

$$W = \overline{W} * \frac{\mu\omega R L^3}{c^2}, \tag{2.18}$$

by considering the dimensionless load $\overline{W}$, dynamic viscosity μ, angular velocity ω, radial clearance c, bearing radius R, and length L. The dimensionless load $\overline{W}$

$$\overline{W} = \frac{\pi}{2} * \frac{\varepsilon}{\left(1-\varepsilon^2\right)^{3/2}} \tag{2.19}$$

is a function of the eccentricity ratio ε

$$\varepsilon = \frac{e}{c}, \tag{2.20}$$

which is given by the eccentricity e and the radial clearance c. Additionally, the friction force F_f

$$F_f = \frac{\mu \omega R^2 L}{c} * \frac{2\pi}{\left(1 - \varepsilon^2\right)^{1/2}} \tag{2.21}$$

can be calculated to estimate the expected power loss P_{Loss}

$$P_{Loss} = F_f \omega R \tag{2.22}$$

of the hydrodynamic journal bearing [51].

2.3 Computational fluid dynamics

Specific fluid flow volumina can be simulated with CFD, which uses numerical methods to solve the governing partial differential equations that are not (or only in special cases) analytically solvable. These numerical computations can be used to gather reliable information on the flow field and its derivatives. The main governing equations for the flow are derived from the Navier-Stokes equations, which refer to the conservation of mass, momentum and energy. Due to their differential form, the equations need to be discretized by a set of algebraic equations, which result in an approximate solution. To make the numerical calculation possible, the region of interest, in which a solution for the fluid flow is to be computed, needs to be designed and subsequently discretized into a finite number of subvolumes. This representation of the volume is called mesh or numerical grid. Finally, it is possible to computationally solve the governing discretized equations iteratively for each cell of the mesh [20, 55].

Thus, CFD creates the possibility to study the fluid flow in a specified volume with the help of virtual experiments. The results emerging from the simulation can help to understand certain processes in the flow field in a high degree of detail than by using an experimental setup. Especially in pumps, the first impressions on the performance or issues with the design are gathered before going into prototyping and physical experiments, which ultimately saves time and money. However, experimental testing is not neglectable since CFD relies on discretization and approximations to the realistic flow, needs to be validated and does not cover the entire realistic situation including blood flow phenomena [20].

2.3.1 Mesh

In general, a mesh can be created in a two-dimensional fashion on a surface or in three dimensions for a volume. Since this master thesis only investigates the flow inside a pump, the volumetric mesh is further described. In CFD simulations, the quality of the generated mesh determines the accuracy, stability and the validity of the numerical solution. Important parameters influencing the quality of the mesh are the mesh density, distribution of cell size, volume ratios of neighboring cells and sufficient refinement layers near walls. Particularly in regions where high gradients are expected, the mesh needs a higher cell density for a satisfactory accuracy. However, in regions with even flow, the density can be lower, which lead to a decrease in computational time. The distribution of regions with different cell densities and the transition ratio from smaller cell sizes to bigger cells have a major impact on the results of a simulation. Near-wall layers, such as prism layers, are important to resolve the highest gradients in boundary layer flow and to calculate turbulence effects [55, 56].
A mesh of a specific volume, can either be structured, unstructured or hybrid. The structured variant is the simplest, which can only be used on simple geometries. Complex geometries can be meshed using the unstructured mesh, since this method is more flexible and fits into arbitrary geometries. However, due to the unstructured nature irregularities arise. The hybrid mesh combines both variants and uses the structured mesh in areas, where it poses an advantage. Cell types used for meshing are hexahedral for structured meshes and either tetrahedral or polyhedral for unstructured meshes. Illustrations of the cell types are displayed in Figure 2.12 [55, 56].

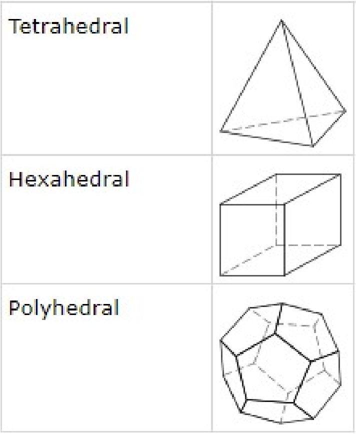

Figure 2.12: Cell types used in generating volume meshes [56].

2.3.2 Simulation of rotating and static regions

Pumps are designed with a stationary pump housing and a rotating impeller. The simulation of such rotating volumes relative to static volumes is either done by incorporating the Multiple Reference Frame (MRF) or Moving Mesh models. The MRF models use two or more confined volumes that are defined to be stationary or to move relative to each other, by adding the resulting forces while keeping the mesh fixed. In contrast to the MRF, the Moving Mesh models update its mesh after each time-step, which increases the accuracy of the simulation results and makes the simulation of transient phenomena due to the impeller rotation even startup and shutdown processes, possible [56, 57]. Nevertheless, this model is computationally more challenging and time consuming mainly because of the dynamic grid deformation. This process involves the adaptation of the mesh and the interpolation of the flow variables to the new positions in the updated mesh [58].

2.3.3 Discretization error of the simulation

Since numerical simulation utilizes a discretization in space and time to solve the differential equations, the solutions have a certain error and uncertainty. Therefore, specific methods were introduced to estimate the magnitude of these errors [20, 59]. Firstly, the uncertainty in the spatial dimension is investigated by comparing the numerical solution of certain variables Φ using different mesh sizes. A reliable method to estimate the spatial discretization error of the mesh size is the Grid Convergence Method. This approach utilizes three mesh sizes with different number of cells. These meshes are referred to as fine, medium, and coarse, based on the number of cells in descending order. Each mesh is compared to the coarser mesh, hence fine with medium and medium with coarse. For each mesh the representative mesh size h

$$h_{1,2,3} = (\frac{1}{N}\sum_{i=1}^{N}\Delta V_i)^{1/3} \tag{2.23}$$

is calculated, where the index corresponds to the fine (1), medium (2) or coarse (3) mesh. In equation 2.23 N is the total number of cells and ΔV_i is the volume of the observed cell i. Furthermore, the grid refinement factor

$$r_{21} = \frac{h_2}{h_1}, \tag{2.24}$$

$$r_{32} = \frac{h_3}{h_2} \tag{2.25}$$

for each comparison is calculated. The different meshes 1, 2 and 3 should be selected systematically so that the grid refinement factor $r > 1.3$ [59].
To make a qualitative comparison of the different mesh sizes, certain variables $\Phi_{1,2,3}$ are observed, which are vital for the interpretation of the simulation results. The differences ϵ of these variables

$$\epsilon_{21} = \Phi_2 - \Phi_1, \tag{2.26}$$

$$\epsilon_{31} = \Phi_3 - \Phi_2 \tag{2.27}$$

are further used to calculate the errors in the spatial dimension. Furthermore, the apparent order p

$$p = \frac{1}{\ln\left(r_{21}\right)} * \left|ln\left|\frac{\varepsilon_{32}}{\varepsilon_{21}}\right| + q\left(p\right)\right| \tag{2.28}$$

needs to be calculated. The term $q(p)$ is assumed to be 0 if the grid refinement factors r_{21} and r_{32} are equal [59]. However, in complex geometries it is not always possible to keep the grid refinement factor constant. Hence $q(p)$ corrects the apparent order p for nonuniform grid refinement ratios [60]. Since q

$$q\left(p\right) = \ln\left(\frac{r_{21}^{p} - s}{r_{32}^{p} - s}\right) \tag{2.29}$$

is a function of p, it must be solved iteratively. The factor s

$$s = 1 * sgn\left(\frac{\varepsilon_{32}}{\varepsilon_{21}}\right) \tag{2.30}$$

depends on the differences ϵ of the observed variables [59].
In order to calculate the grid convergence index (GCI), which corresponds to the numerical uncertainty of the spatial resolution, the approximate relative error e_a

$$e_{a,21} = \left|\frac{\Phi_1 - \Phi_2}{\Phi_1}\right| \tag{2.31}$$

is calculated. Lastly, the GCI

$$GCI_{21} = 1.25 * \frac{e_{a,21}}{r_{21}^{p} - 1} \tag{2.32}$$

can be computed, which estimates the discretization error of the medium-meshed solution compared to the coarse mesh and fine mesh solution, respectively. Here the value “1.25” is used as a safety factor, which was introduced based on experience applying this method [59, 61]. To assess if the medium mesh is refined enough, the fine-grid convergence index GCI_{21} is observed [59].
Secondly, the error due to time discretization is estimated by adjusting the time-step of the simulation. The relative error of the resulting variables Φ are calculated using equation 2.31 [20].

2.3.4 Simulating blood damage in RBPs

In general, the potential of blood damage is investigated by numerically calculating the shear stresses that evolve in the flow field and would act on the blood components with a certain exposure time. The respective shear stress thresholds for the van Willebrand factor, platelet activation and hemolysis were introduced in Chapter 2.1 [9, 20]. Especially, the effect of the shear stress τ and the exposure time t on hemolysis was more thoroughly investigated. To observe this effect in a defined volume, CFD offers two methods. Firstly, the Lagrangian method tracks particles along their path lines in the fluid volume. This method enables the calculation of the exerted shear stresses on certain particles along the way to the device outlet. Consequently, the history of damage to a single erythrocyte can be computationally calculated. However, the simulation error is sensitive to the distribution of the simulated path lines in the volume, especially for complex geometries. Moreover, stagnation zones and flow separation create regions where the flow velocity reaches zero, which poses problems in computing path lines in these regions. Secondly, the Eulerian method derives the blood damage by integrating a transported passive scalar over the entire flow volume. In this case, the entire flow field is included in the computation, but the information on the damage history of specific particles along its flow path is not accessible. The Eulerian method is usually preferred in computing the blood damage of VADs [39, 62].

Since increased blood damage is linked to turbulence in the flow, turbulent flow conditions need to be considered in the simulations. A concept to include the account of turbulence in the flow to the shear stress τ was introduced by incorporating the turbulent viscosity ν_t into the Reynold-Averaged Navier-Stokes (RANS) equation. The turbulent viscosity ν_t describes the effect of velocity fluctuations in the small scale, which are not included in the RANS equation, which is often used for flow simulation purposes [63]. Therefore, the exerted shear stress

$$\tau = \rho * (\nu + \nu_t) * \frac{d\vec{v}}{d\vec{y}} \tag{2.33}$$

is influenced by the density ρ, the kinematic viscosity ν, the turbulent eddy viscosity ν_t and the velocity gradient $\frac{d\vec{v}}{d\vec{y}}$. While the kinematic viscosity depends on the fluid properties, the turbulent viscosity depends on the size and form of the turbulence field [16].

The influence of low blood flow velocities on thrombi formation was studied by

Pivkin et al. [64]. Therefore, the thrombi growth rate at velocities ranging from 0.1 to 0.8 $\frac{m}{s}$ was analyzed. The results show the highest increase in thrombotic reaction at velocities of 0.1 $\frac{m}{s}$ [64].

Chapter 3

Materials and methods

In the subsequent section, the methods employed to design and analyze single-stage pump concepts are described, which are equivalent to the two-stage pump design currently developed at the MUW. The methodology used in this research combines a systematic and interdisciplinary approach to address the complexities associated with the design process of RBPs. This chapter provides detailed information about the theoretical calculation of the pump design parameters, its design using computer aided design (CAD), and the subsequent CFD simulations. The simulation results are used to identify refinement potentials for the designed pump. For this purpose, the mean of the resulting parameters over the last computed rotation is calculated. Additionally, the results are subject to a mesh and time-step independency study to determine the numerical uncertainty due to discretization. These processes are repeated in an iterative approach, until a refined single-stage RBP design has been found.

3.1 Calculation of the design parameters

To calculate the geometry of RBPs, the theoretical background of rotodynamic pumps is being used. However, as stated before, there are some adjustments compared to the industrial design guidelines which need to be considered to ensure hemocompatibility [20]. Furthermore, several boundary conditions must be met since the aim of this thesis is to design a single-stage pump that is comparable to the two-stage pump concept. Table 3.1 comprises the main parameters of the two-stage pump, which were used to calculate the similar pump concepts. The index “$2S$” denotes the parameters of the two-stage pump.

The design of the two-stage pump can be seen in Figure 1.2. In this thesis, two distinct pump designs are calculated, utilizing the initially developed calculation program described in Appendix A.

Table 3.1: Main parameters of the two-stage pump used to develop similar pumps.

Q_{2S}	1.5 L/min	$d_{inlet,2S}$	6 mm
H_{2S}	53.87 mmHg	$d_{outlet,2S}$	6 mm
n_{2S}	6400 rpm	$h_{1,2S}$	2 mm
$z_{st,2S}$	2	$h_{2,2S}$	1.5 mm
$z_{Bl,2S}$	4	$e_{1,2S}$	0.2 mm
$d_{1i,2S}$	3 mm	$e_{2,2S}$	0.7 mm
$d_{1a,2S}$	5 mm	$\beta_{1,2S}$	39°
$d_{2,2S}$	11 mm	$\beta_{2,2S}$	45°

3.1.1 General design

To keep both designed concepts similar to the two-stage pump, some general parameters were introduced. Firstly, all pumps are conveying the same fluid, with the same volume flow Q, and generate the same total pressure head H. Secondly, the impellers of the semi-axial pumps are designed with an inclination angle ϵ_{hub} of 15° (see Figure 3.3) and four blades, which are covered by a shroud. The shroud thickness, as well as the distance to the pump housing (see Figure 2.4a) are equal to the two-stage pump concept, with 0.3 mm and 0.5 mm, respectively. The distance to the pump housing is essential for the recirculation of the blood in RBP. A moderate recirculation is needed to enhance the washout of the pump, thus reducing blood damage [65].

Furthermore, the de Haller criterion is considered in the design process of the pump, to minimize flow separation and therefor improve the flow field. The de Haller criterion describes a threshold for the deceleration ratio

$$\frac{w_2}{w_1} > 0.55 \tag{3.1}$$

of the relative velocity at the impeller outlet and the impeller inlet. If this criterion is not met, flow separation can occur at the boundary layers [66].
Another design aspect includes the hydrodynamic journal bearing, which influences the functionality of the pump [51]. The bearings of the later single-stage pump designs shall exhibit a similar load-carrying capacity W as the two-stage pump, to make the overall function comparable. Therefore, the radial clearance c is adjusted, but the bearing length L is kept the same. Furthermore, the concepts share a common feature to ensure the recirculation of the blood passing through the gaps in the bearing region. Therefore, all impellers were designed with a concentric hole with a diameter of 0.6 mm, which can be seen in Figure 3.1. This diameter was selected since the simulation results showed that the flow velocities in the hole were above 0.1 $\frac{m}{s}$. Furthermore, the oncoming flow from the pump inlet did not flow into the hole, but was diverted into the blade channels by the recirculating flow (see Figure 3.2).

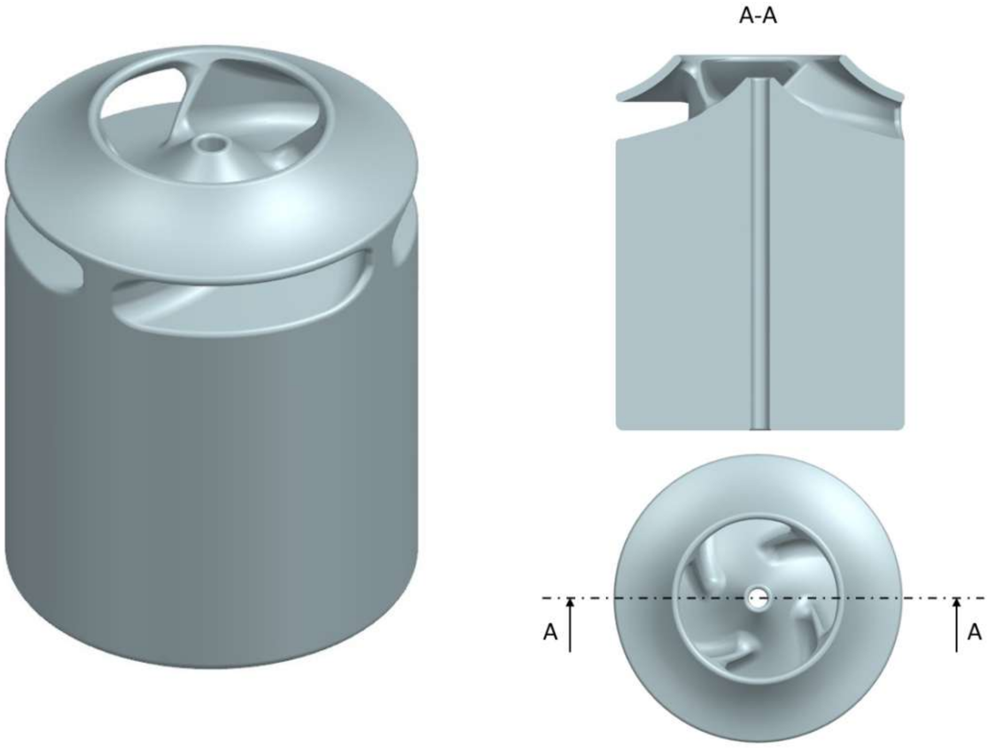

Figure 3.1: Impeller geometry with a cross-sectional view to show the hole through the impeller.

The volute design was computed by the principles of conservation of velocity [46], which was performed by the calculation program. The design was initiated at

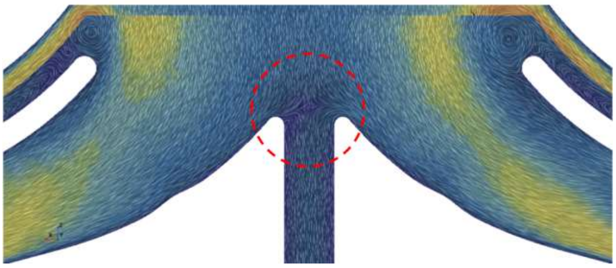

Figure 3.2: Illustration of the flow field with a detailed observation around the hole through the impeller.

the volute cutwater, which is located at a diameter d_4. General recommendations for an optimal position of the volute cutwater by Stepanoff [46] suggest d_4 to be 10% higher than the impeller diameter d_2. Subsequently, the impeller geometry was connected to the volute geometry utilizing edge blends. Lastly, the volute cross-section was linearly increased with increasing angle until a full rotation was performed. From this position the volute was designed as a conical shaped duct following a straight path to the volute outlet. The diameter of the volute outlet and the diameter of the inflow tube of the pump housing were equally dimensioned at 6 mm, which coincides with the two-stage pump design. This measure aims to create a similar inflow and outflow behavior.

The inflow tube diameter decreases towards the transition to the impeller. The diameter of the inflow tube at the transition site also defines the outer diameter of the leading edge (impeller inlet) d_{1a}(see Figure 3.3), which is 5 mm in all pump designs.

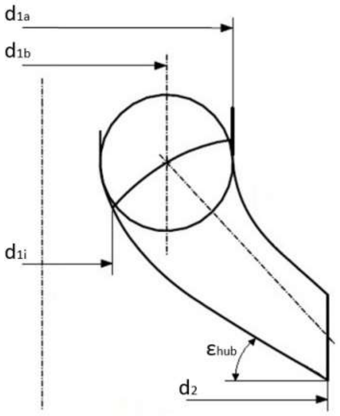

Figure 3.3: Sketch of an impeller blade of a semi-axial pump with main measurements, modified from [16].

3.2 CAD

Based on the calculated geometrical parameters of the RBP, the respective concept was designed using NX CAD software (version: 1899) by Siemens AG (Munich, Germany). To further use this data to simulate the flow of the fluid, the fluid volume inside the pump was designed. A parametric design was implemented in the 3D CAD model to facilitate quicker adjustment of the parameters. The information derived from the subsequent CFD simulation were used to change certain parameters, to improve the overall functionality of the single-stage pump.

3.3 CFD simulation

The numerical analysis of the fluid flow through the pump was performed by using the software Simcenter STAR-CCM+ (version: 16.02.008-R8) by Siemens AG (Munich, Germany).

3.3.1 CFD geometry of the pump

To define the volumetric boundaries of the simulation, the previously created CAD data was imported as a parasolid file. The rotation of the impeller was simulated using the MRF model. Therefore, an interface was created surrounding the impeller and the adjacent fluid volume, which defines the rotating region in combination with the impeller geometry. To incorporate the rotational motion of the fluid volume close to the wall, the interface walls were positioned in the middle of the circumferential bearing gap and the shroud gap, respectively. The bottom of the interface was defined at the beginning of the bearing gap. Figure 3.4 depicts the position of the interface. Furthermore, the impeller walls outside of the defined interface (radial, axial and hole walls) were defined as rotating regions with the same rotation rate as the respective pump concept.

3.3.2 Simulation setup

An unstructured, polyhedral mesh of the fluid inside the pump was created. Additionally, thin mesher and prism layer mesher were used to qualitatively represent

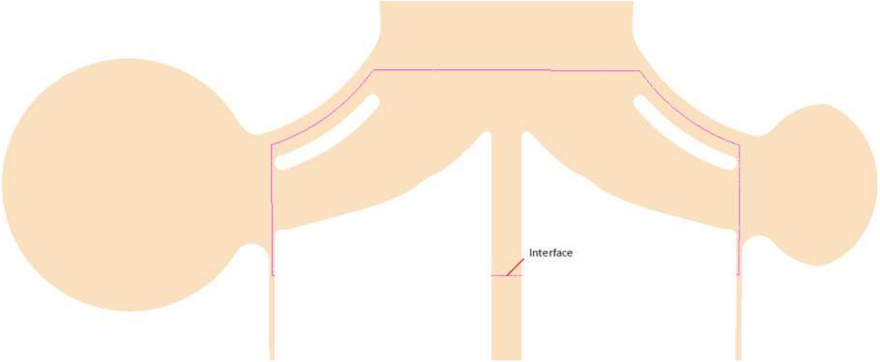

Figure 3.4: Illustration of the pumps cross-section with interface highlighted.

narrow gaps and wall near regions, respectively. The conception and sizes of the meshes were based on experience. The suitability of the meshes were confirmed by a mesh independency study, which was performed by the application of the Grid Convergence Method [59].

The computation of turbulence is done by using the $k - \omega$ SST model, which is a commonly employed approach in RBP simulations [9, 20, 62]. The time step of the solver was set relative to the rotation rate of the pump to achieve a rotation of 2° per step. The simulation was executed to model 10 rotations of the pump, followed by a verification of the convergence of the results. To assess convergence, the observation focused on the pressure head behavior, which revealed that the difference between the mean of the last rotation and the preceding one was below 1%. The simulation results of the final pump concept were subject to a time step independency study, employing different time step sizes to achieve rotations of 1° and 4°, respectively.

Blood exhibits shear thinning properties and is therefore regarded as a non-Newtonian fluid. To simulate the material properties correctly, the Non-Newtonian Generalized Carreau-Yasuda Fluid model was used [67]. In Simcenter STAR-CCM+ this model was implemented with a relaxation time λ of 3.313 seconds, zero shear viscosity μ_0 of 0.056 Pa*s, infinite shear visosity μ_∞ of 0.00345 Pa*s, power constant n of 0.3568 and a parameter a of 2 [68]. The blood density used in this study was $\rho = 1050\ kg/m^3$, which is consistent with findings in related research on blood flow in RBPs [9].

Additional boundary conditions for the inlet and outlet were introduced to the simulation. The inlet of the pump acts as a mass flow inlet with 0.02625 kg/s equivalent to a volume flow of 1.5 L/min, considering the assumed blood density. The outlet was set as a pressure outlet with a pressure of 0 Pa. Lastly, the turbulence profile of the inlet and outlet region was predefined by the turbulence intensity and length scale. Both are considered constant, the intensity with a value of 0.01, and a length scale of 6 mm, which correspond to the diameter of the inlet and outlet of the pump.

3.3.3 Pump efficiency

The pump efficiency is assessed by calculating the mechanical efficiency utilizing the equations 2.3 2.4 2.5 and 2.8:

$$\eta_m = \frac{0.013595 * H * g * \rho * Q}{T_m * 2 * \pi * n_m}. \tag{3.2}$$

3.3.4 Shear stress and hemolysis

The application of CFD in the development of RBPs also enables the assessment of the hemocompatibility. Investigating stagnation zones, the shear stress level, together with the exposure time to the fluid are obligatory when it comes to managing blood flow [20]. The shear stresses on each volumetric element of the mesh were calculated using equation 2.33. The velocity gradient $\frac{d\vec{v}}{d\vec{y}}$ is calculated by STAR-CCM+ as the strain rate tensor. However, since we want to express the shear stress in each cell with a single quantity, the modulus of the mean strain rate tensor is used. The mean strain rate tensor **S**

$$\mathbf{S} = \frac{1}{2} * (\nabla\vec{\bar{v}} + \nabla\vec{\bar{v}}^T) \tag{3.3}$$

is described by the mean velocity $\vec{\bar{v}}$. Furthermore, the modulus of the mean strain rate tensor S is defined by:

$$S = |\mathbf{S}| = \sqrt{2\mathbf{S} : \mathbf{S}} \tag{3.4}$$

and is replacing the velocity gradient $\frac{d\vec{v}}{d\vec{y}}$ in equation 2.33 [69].

Since the dynamic viscosity μ

$$\mu = \rho * \nu \tag{3.5}$$

is the product of the density ρ and the kinematic viscosity ν, the provided field function for the dynamic viscosity was used [16]. The $k - \omega$ SST model computes the turbulent viscosity μ_t for the simulated pump [70].
The numerical assessment of the level of hemolysis, as described in chapter 2.1.3, was performed by utilizing the Eulerian method, which includes the results of the entire flow field of the pump. A passive scalar transport equation starting at the pump inlet with the power law relation of shear stress level and exposure time as the source term was implemented. The passive scalar model simulates the transport and dispersion of a scalar quantity within a fluid flow. This process was done after convergence of the general simulation of the pump flow was achieved. Subsequently, the approach from Garon and Farinas [39] was applied in Simcenter STAR-CCM+. Firstly, the power law with the empirical parameters from Heuser and Opitz [40] was transformed to the linear damage D_I

$$D_I = D\left(\tau, t\right)^{1/\alpha} = \left(1.8 * 10^{-6}\right)^{1/0.765} * \tau^{1.991/0.765} * t, \tag{3.6}$$

which is subsequently discretized in time. Thus, the time derivative of D_I

$$\frac{d}{dt} D_I = \left(1.8 * 10^{-6}\right)^{1/0.765} * \tau^{1.991/0.765} \tag{3.7}$$

is computed. To obtain an average value for the linear damage

$$\overline{D_I} = \frac{1}{Q} \int\limits_V \frac{d}{dt} D_I dV = \frac{\rho}{\dot{m}} \int\limits_V \frac{d}{dt} D_I dV \tag{3.8}$$

the volume integral of $\frac{d}{dt} D_I$ is calculated and normalized by the volume flow Q. However, the volume flow Q was not explicitly given in the simulation setup. Consequently, it was substituted in equation 3.8 by the parameters ρ and $\dot{m}$, which define the volume flow. The fraction of damaged erythrocytes D

$$D = \left(\overline{D_I}\right)^{0.765} \tag{3.9}$$

can be calculated by inverse transform of the discretized solution in space and time $\overline{D_I}$ [39]. Finally, the $mgNIH$

$$mgNIH = 120 * D * 100 * 1000 \tag{3.10}$$

can be calculated, where Hb was assumed to be 120 g/L [44].
Additional observations were performed, to assess the damage to the different blood components, introduced in chapter 2.1. Therefore, the parts of the volume, which are exposed to shear stresses above the respective thresholds of the vWF, platelets and red blood cells, were analyzed.

3.3.5 Washout and stagnation

To observe the washout of the pump, a passive scalar transport model was used. The initial condition for the fluid volume was set to "1" and regarded as "old blood". By simulating further rotations, the mass flow inlet provided fluid with the passive scalar value "0", which dispersed throughout the pump volume. The representation of the washout capability of the RBP is determined by the distribution of the passive scalar value and the volumetric percentage of cells that still occupy the 'old blood' after multiple rotations. Critical geometries for the washout, such as the bearing and the hole through the impeller, were additionally monitored. Therefore, two planes were introduced for the bearing and the hole respectively (see Figure 3.5), to assess the amount of old blood present in these cross-sections.
Stagnation zones are located by plotting regions with low velocities $< 0.1 \ \frac{m}{s}$ [64].

3.4 Iterative approach

The resulting data gathered by the simulations were used to conclude certain changes to improve the geometry of the pump. However, maintaining the general pump design was imperative to ensure the similarity with the two-stage pump. Mainly the pressure head generation and the velocity distribution of the flow field inside the impeller and volute were observed. Therefore, line integral convolution (LIC) was used to visualize the magnitude and the direction of the velocities. The velocity distribution was used to assess flow separation and stagnation zones, thus

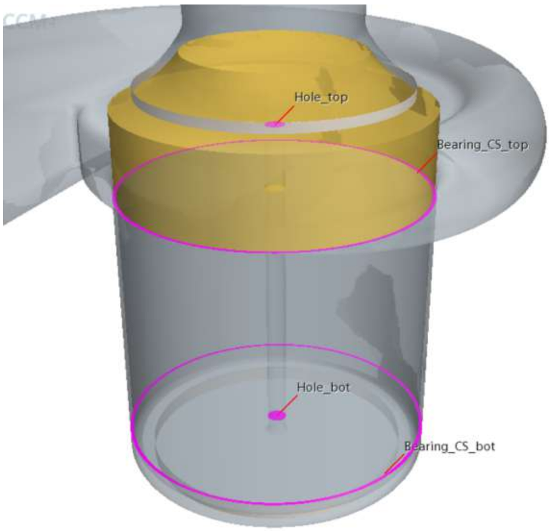

Figure 3.5: Geometry of the pump showing the location of the highlighted surfaces in the critical regions for the washout.

estimating the hemocompatibility and washout of the pump.

Furthermore, the static pressure distribution and the location of the accumulated pressure at the volute cutwater were observed to adapt and further improve the pump performance. Figure 3.6 depicts the aforementioned processes which are iteratively executed until a satisfactory pump concept is identified. After completing the iterative process, the hemocompatibility and washout are finally simulated for the improved pump geometry.

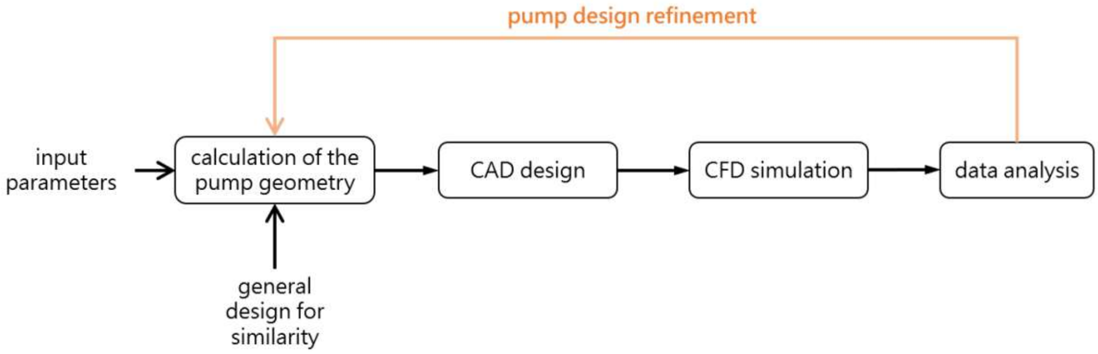

Figure 3.6: Sequence of the iterative process used in this thesis to develop a refined RBP.

3.4.1 Concept 1 – identical specific speed and specific diameter

The geometrical parameters of the first pump design are based on the concept of geometrical similarity. Hence, it is essential that the specific speed n_q and specific diameter d_q of the single-stage pump match those of the two-stage pump [16]. Therefore, the specific speed n_q and specific diameter d_q of the two-stage pump are calculated using equations 2.16 and 2.17, respectively. The main parameters of the two-stage pump can be found in Table 3.1. This results to $n_q = 68.25$ and $d_q = 1.711$. The first concept for the single-stage pump was developed to exhibit the same values for n_q and d_q. Therefore, equations 2.16 and 2.17 are transformed to calculate the rotation rate n

$$n_1 = n_q * \frac{\left({}^{H}\!/_{z_{st}}\right)^{0.75}}{\sqrt{Q}} = 68.25 * \frac{\left(\frac{53.87*0.01359 \ m}{1}\right)^{0.75}}{\sqrt{\frac{1.5}{60*1000} \ \frac{m^3}{s}}} \cong 10800 \frac{U}{min} \tag{3.11}$$

and the impeller diameter d_2

$$d_{2,1} = d_q * \frac{\sqrt{Q}}{\left({}^{H}\!/_{z_{st}}\right)^{0.25}} = 1.711 * \frac{\sqrt{\frac{1.5}{60*1000} \ \frac{m^3}{s}}}{\left(\frac{53.87*0.01359 \ m}{1}\right)^{0.25}} * 10^3 = 9.25 \ mm \tag{3.12}$$

of a single-stage pump, with the same volume flow Q. The values for n_1 and $d_{2,1}$ were imperative for the similarity of this pump concept, thus they could not be further adjusted for refinement purposes.

The improvement of this pump concept was performed by adjusting the blade heights $h_{1,2}$, blade thickness e_2 and the blade angles $\beta_{1,2}$. The calculation program provided a recommendation for the optimal diameter d_4 of the volute cutwater position, which was subsequently refined through iterative adjustments. As both pumps exhibit the same parameters n_q and d_q, they also share the same point in the Cordier- diagram. Therefore, the efficiency of the single-stage pump can be expected to be similar to the two-stage pump [48].

In the following subsections the most significant pump configurations are introduced, which were subsequently refined in an iterative process. The section describes the path of the iterative process until the final pump design was developed including the design ideas and the analysis of the respective resulting flow field. For simplicity, only the concepts which exhibit major changes are described in detail. Table 3.2 comprises the main parameters and results of each iteration introduced for concept 1.

Table 3.2: Summary of the design parameters and respective results for each iteration described of concept 1.

parameters/iterations	**1**	**9**	**11**	**13**
h_1 mm	3	1.8	1.8	1.8
h_2 mm	2	1.4	1.2	1.2
e_2 mm	0.8	0.7	0.8	0.8
β_1 °	35	34	34	34
β_2 °	45	38	38	38
d_4 mm	12	10.5	10.5	10
H mmHg	**53.4**	**62.88**	**55.37**	**55.81**
$\boldsymbol{\eta}$ **%**	**42**	**34**	**31**	**29.6**

Iteration 1

The idea behind the 1st pump configuration was to additionally keep the relative velocities $w_{1,2}$ at the impeller leading (impeller inlet) and trailing edge (impeller outlet) (see Figure 2.4a) as close to the ones in the two-stage pump, to further enhance similarity. To realize this, a set of geometrical adaptations where necessary to create a blade channel that generates similar relative velocities at a different diameter and rotational speed. In the two-stage pump, the relative velocities were theoretically calculated to $w_{1,2S}= 2.110\ \frac{m}{s}$ and $w_{2,2S}= 0.924\ \frac{m}{s}$ by the calculation program.

Design By adjusting the geometrical parameters in the calculation program, a fitting pump concept was created with theoretical relative velocities $w_{1,1}= 2.197\ \frac{m}{s}$ and $w_{2,1}= 0.961\ \frac{m}{s}$, which exhibit a deviation of around 4% to the intended values. Here, the index “1” after the comma marks the parameters of the first pump concept for the single-stage pump. Figure 3.7 depicts the calculation of the 1st design and its parameters, which was subsequently designed and simulated.
The volute design of this pump iteration was based on the results of the calculation

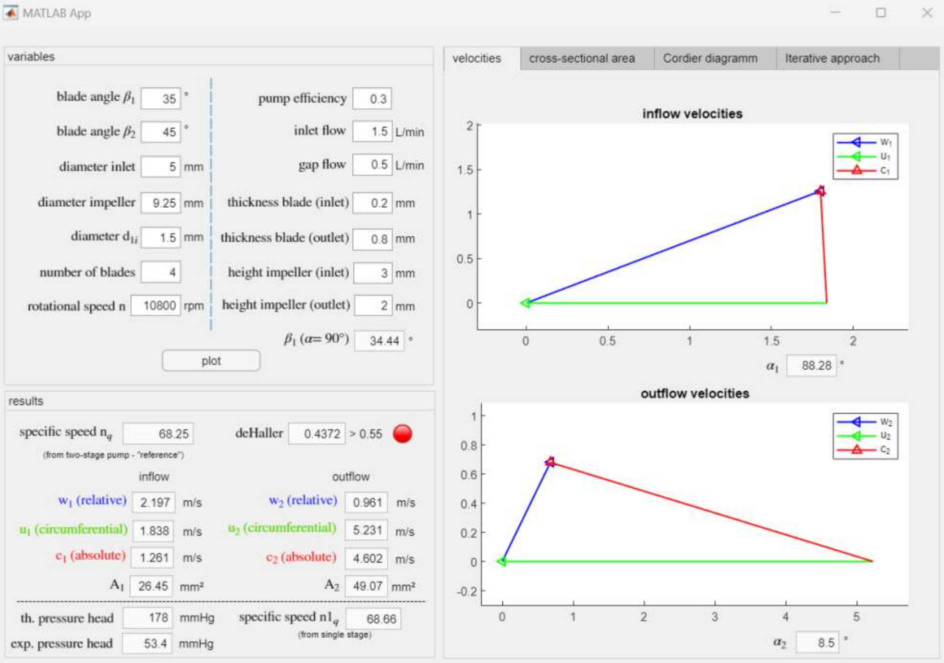

blade angle β_1 35 °
blade angle β_2 45 °
diameter inlet 5 mm
diameter impeller 9.25 mm
diameter d_{1i} 1.5 mm
number of blades 4
rotational speed n 10800 rpm
pump efficiency 0.3
inlet flow 1.5 L/min
gap flow 0.5 L/min
thickness blade (inlet) 0.2 mm
thickness blade (outlet) 0.8 mm
height impeller (inlet) 3 mm
height impeller (outlet) 2 mm
β_1 (α= 90°) 34.44 °

specific speed n_q 68.25
(from two-stage pump - "reference")
deHaller 0.4372 > 0.55 ●

inflow
w_1 (relative) 2.197 m/s
u_1 (circumferential) 1.838 m/s
c_1 (absolute) 1.261 m/s
A_1 26.45 mm²

outflow
w_2 (relative) 0.961 m/s
u_2 (circumferential) 5.231 m/s
c_2 (absolute) 4.602 m/s
A_2 49.07 mm²

th. pressure head 178 mmHg
exp. pressure head 53.4 mmHg
specific speed $n1_q$ 68.66
(from single stage)

α_1 88.28 °
α_2 8.5 °

Figure 3.7: First iterative calculation of the 1st pump design with the respective parameters.

program, which is shown in Figure 3.8. To support the design process, the diameter of the volute cross-section is presented at specific angles in 90° steps. These were calculated by the conservation of momentum and conservation of velocity, respectively, however the latter was used in the pump design. Furthermore, the "diameter at tongue" shown in Figure 3.8 represents the diameter d_4, which is the recommended position of the volute cutwater. However, in this design, the volute cutwater was designed at a diameter of 12 mm, since in the early pump design stages the calculation approach presented by Gülich [16] was performed. The results of this approach led to a bigger diameter for the volute cutwater than the approach by Stepanoff [46] used later on, which was described in chapter 3.1.1. The idea behind the first bearing design emerged by visually bisecting the two-stage pump to a single-stage pump, as implicated in Figure 3.9. Thus, the radial clearance c was kept constant at 100 μm and the length of the bearing L was halved. The design of the described pump can be seen in Figure 3.10. However, this pump design leads to load-carrying capacities W with a relative difference of -85% compared to the two-stage pump, which are compared in Table 3.3. For simplicity reasons only values at eccentricity ratios ε of 0.85 to 0.5 in 0.05 increments are depicted, since this range is typical for hydrodynamic journal bearings [51].

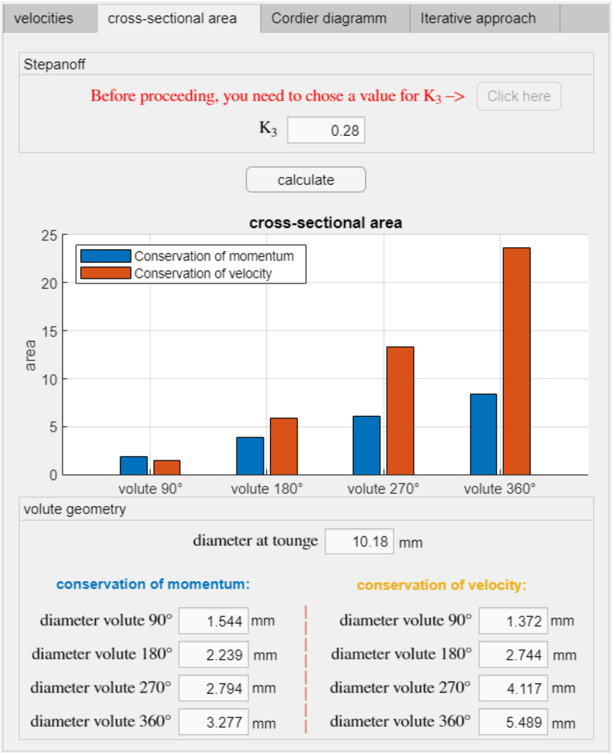

Before proceeding, you need to chose a value for K_3 –>

K_3 0.28

diameter at tounge 10.18 mm

conservation of momentum:			conservation of velocity:		
diameter volute 90°	1.544	mm	diameter volute 90°	1.372	mm
diameter volute 180°	2.239	mm	diameter volute 180°	2.744	mm
diameter volute 270°	2.794	mm	diameter volute 270°	4.117	mm
diameter volute 360°	3.277	mm	diameter volute 360°	5.489	mm

Figure 3.8: Calculation of the volute geometry for the 1st pump iteration of concept 1.

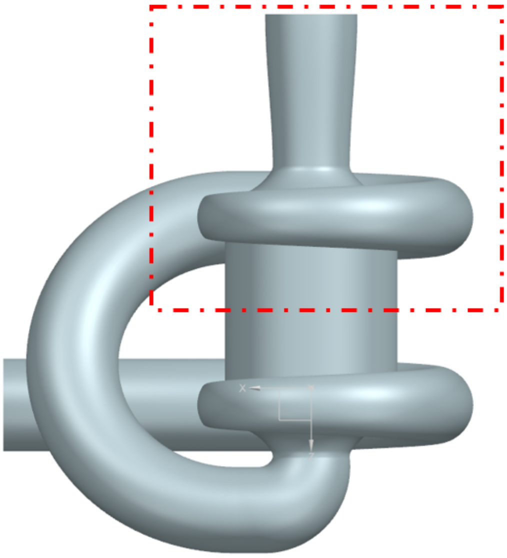

Figure 3.9: Illustration of the two-stage pump design with a red rectangle indicating the bisected volume.

Table 3.3: Bearing parameter comparison of the two-stage and single-stage pump (1st iteration of concept 1).

	Two-stage pump		**Single-stage pump** **$d_2 = 9.25$ mm**	
ε	$[W]$ N	$[P_{loss}]$ W	$[W]$ N	$[P_{loss}]$ W
0.85	4.22	0.31	0.63	0.24
0.8	3.14	0.27	0.47	0.22
0.75	2.48	0.25	0.37	0.20
0.7	2.04	0.23	0.30	0.18
0.65	1.72	0.21	0.26	0.17
0.6	1.47	0.20	0.22	0.16
0.55	1.26	0.19	0.19	0.15
0.5	1.09	0.19	0.16	0.15

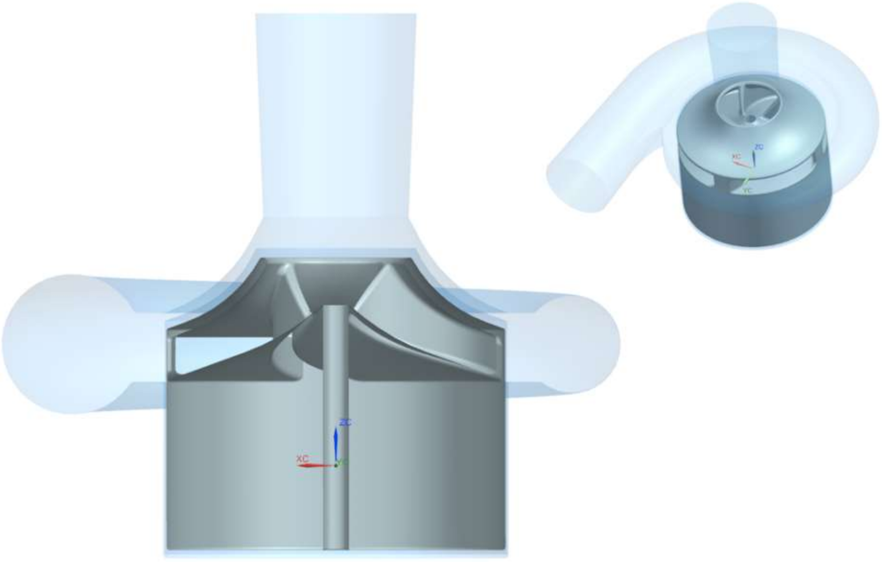

Figure 3.10: Illustration of the 1st design of pump concept 1.

Performance The simulation for this pump design resulted in a pressure head of 85.04 mmHg. The observed rise in pressure was unexpected, as the pump's initial calculation anticipated a pressure head of approximately 53.4 mmHg (see Figure 3.7). This could be linked to the low efficiency assumed in the analytical pump design (η= 30%), since the pump efficiency was calculated by the simulation results to be around 42%, utilizing equation 3.2. However, the flow field of the pump presents a flow characteristic that hinder its functionality as a RBP. The velocity inside the blade channel is rather non-uniform along the height and even a recirculating flow is observable, which restricts the utilization of the entire channel height for achieving uniform flow (see Figure 3.11a). Additionally, flow separation occurs at the blades, which is visible in Figure 3.11b, where dark blue spots in close proximity to the impeller blades can be seen.

The flow separation is most likely formed because the de Haller criterion, with a value of 0.4372, was not fulfilled. Lastly, the instantaneous static pressure distribution is shown in Figure 3.11c. The illustration exhibits dark red spots which indicate higher pressure exposure at these locations. Moreover, the pressure spot at the volute cutwater did not form directly at the conjunction between the beginning and the outlet of the volute, which could lead to further losses. The desired static pressure distribution features a uniform pattern around the impeller, with a concentrated pressure area located directly at the volute cutwater.

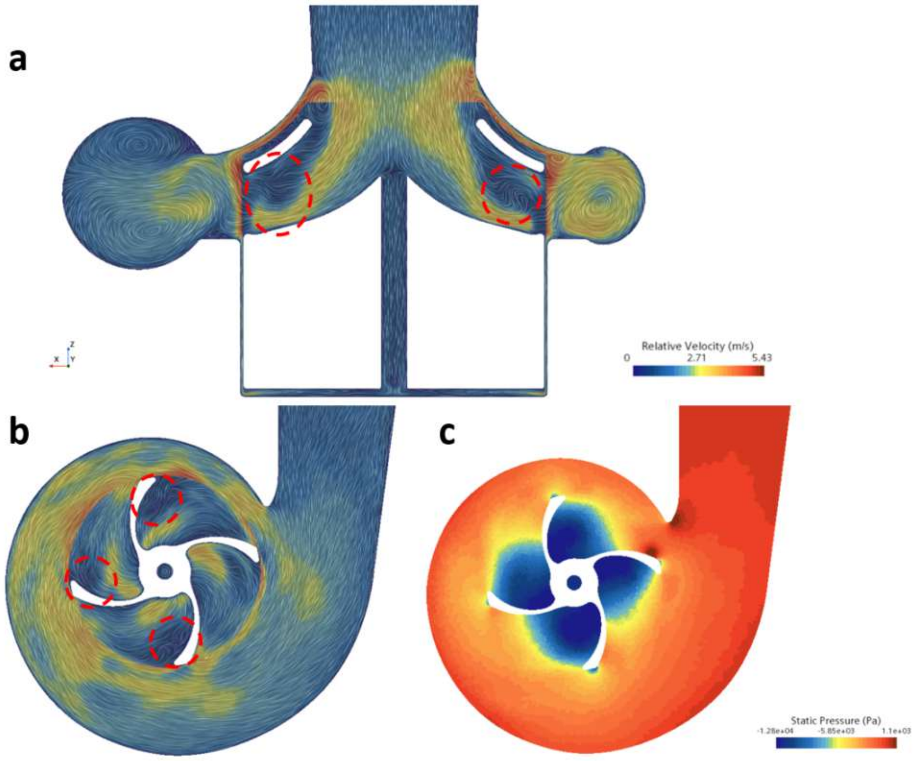

Figure 3.11: Simulation results of the 1st pump iteration of concept 1 with (a) the relative velocities in the XZ-plane, (b) the relative velocities in the XY-plane and (c) the static pressure in the XY-plane.

Conclusion By keeping the relative velocities $w_{1,1}$ and $w_{2,1}$ similar to the ones present in the two-stage pump, some parameters had to be changed. This significantly reduced the similarity of the geometric parameters between the two pumps impellers. Therefore, this feature was disregarded in further pump concepts. Furthermore, the edge blends of the pump housing were designed too small, which could disrupt a smooth flow. Figure 3.12 shows a detailed observation of the flow leaving the impeller into the volute. The red circles surround the locations of the described edge blends.

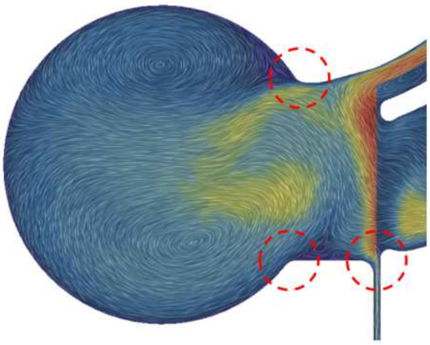

Figure 3.12: Scaled view of the relative velocity of the flow leaving the impeller into the volute.

Iteration 9

This concept revolved around the idea of having most blade design parameters similar as used in the two-stage pump.

Design In this design, the inner diameter of the impeller inlet d_{1i}, as well as the blade thicknesses e_1 and e_2 were kept constant. Since the overall height of the blade channel was not fully utilized by the blood flow in the previous concept, the heights of the impeller inlet h_1 and outlet h_2 were decreased. Furthermore, the blade angles β_1 and β_2 were adjusted to increase the ratio of the relative velocities $\frac{w_2}{w_1}$, which were used to assess the compliance of the de Haller criterion. The pump efficiency and the gap flow, which is formed over the impeller shroud, were adjusted based on the simulation results of the 1st pump design. Figure 3.13 shows the parameters used to design this pump configuration. The adjusted input parameters have a minor impact on the calculation for the volute design. Therefore, the previous values shown in Figure 3.8 are iteratively adjusted. Based on the previously analyzed simulation results, the diameter at the volute cutwater was decreased to 10.5 mm and the diameter of the volute cross-section at 360° was decreased to 5.2 mm.

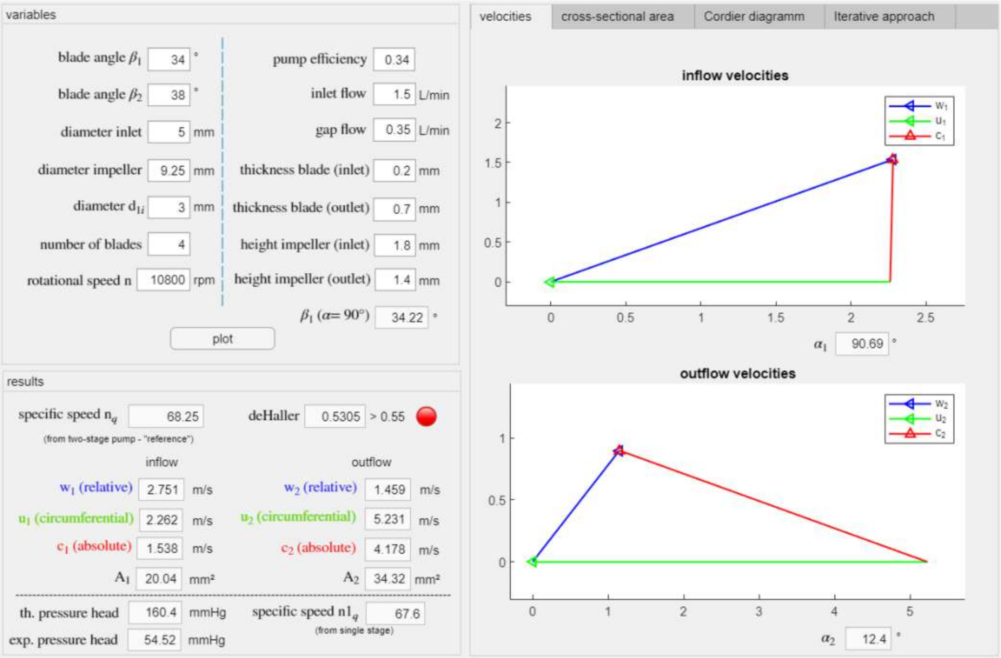

variables

blade angle β_1 34 °
blade angle β_2 38 °
diameter inlet 5 mm
diameter impeller 9.25 mm
diameter d_{1i} 3 mm
number of blades 4
rotational speed n 10800 rpm

pump efficiency 0.34
inlet flow 1.5 L/min
gap flow 0.35 L/min
thickness blade (inlet) 0.2 mm
thickness blade (outlet) 0.7 mm
height impeller (inlet) 1.8 mm
height impeller (outlet) 1.4 mm
β_1 (α= 90°) 34.22 °

results

specific speed n_q 68.25
(from two-stage pump - "reference")
deHaller 0.5305 > 0.55 ●

inflow
w_1 (relative) 2.751 m/s
u_1 (circumferential) 2.262 m/s
c_1 (absolute) 1.538 m/s
A_1 20.04 mm²

outflow
w_2 (relative) 1.459 m/s
u_2 (circumferential) 5.231 m/s
c_2 (absolute) 4.178 m/s
A_2 34.32 mm²

th. pressure head 160.4 mmHg
exp. pressure head 54.52 mmHg
specific speed $n1_q$ 67.6
(from single stage)

α_1 90.69 °
α_2 12.4 °

Figure 3.13: The 9th iterative calculation of the first pump concept with the respective parameters.

Further geometrical changes were executed to the bearing. The bearing length L was increased to the same length as in the two-stage pump. This adjustment enables a direct comparative analysis of the bearing performance. The radial clearance c= 110 μm resulted in load-carrying capacities W in the same range as the two-stage pump with a relative difference of -1.75%. A comparison of the bearing performance parameters is shown in Table 3.4.

Additionally, the edge blends of the pump housing were increased as seen in Figure 3.14. The performed changes improved the flow field in the transition from impeller to volute since the volute geometry is more aligned with the direction of the flowing volume.

Performance The simulation results for this pump yielded an averaged pressure head of 62.88 mmHg and a torque of $0.57 * 10^{-3}$ Nm. By applying these parameters to equation 3.2, a pump efficiency of 34% is calculated. However, flow separation still occurred inside the blade channel. This is again visible by the dark blue spots

Table 3.4: Bearing parameter comparison of the two-stage and single-stage pump (9th iteration of concept 1).

	Two-stage pump		**Single-stage pump $d_2 = 9.25$ mm**	
ε	$[W]$ N	$[P_{loss}]$ W	$[W]$ N	$[P_{loss}]$ W
0.85	4.22	0.31	4.14	0.44
0.8	3.14	0.27	3.08	0.39
0.75	2.48	0.25	2.44	0.35
0.7	2.04	0.23	2.00	0.33
0.65	1.72	0.21	1.69	0.31
0.6	1.47	0.20	1.44	0.29
0.55	1.26	0.19	1.24	0.28
0.5	1.09	0.19	1.07	0.27

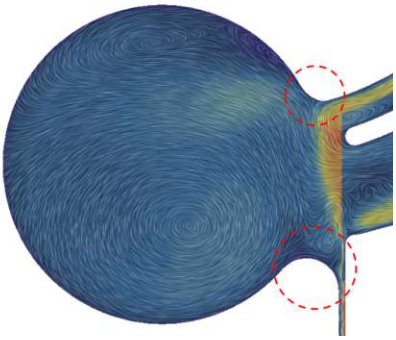

Figure 3.14: Detailed cross-sectional view of the flow field inside the pump of iteration number 9, with the adjusted edge blends marked.

in Figure 3.15b. Additionally, Figure 3.15a shows that the flow velocity along the height of the impeller outlet was uneven. Lastly, the static pressure distribution, as illustrated in Figure 3.15c, presents a non-uniform pattern surrounding the impeller.

Conclusion The dimensioning of the bearing is regarded as complete because the adjusted bearing dimensions yield a similar load-carrying capacity W as the two-stage pump. However, the impeller geometry needs to be refined, since the present velocity and pressure distribution are detrimental for the function of a blood pump.

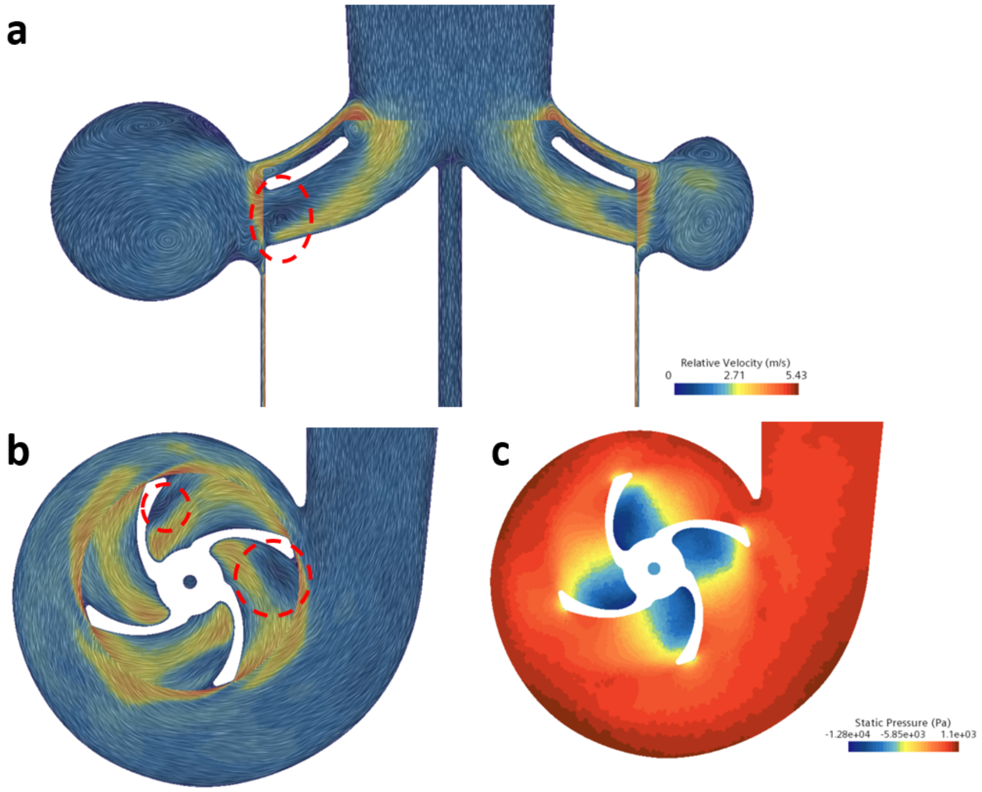

Figure 3.15: Simulation results of the 9th pump iteration of concept 1 with the (a) relative velocities in the XZ-plane, (b) relative velocities in the XY-plane and (c) the static pressure in the XY-plane.

Iteration 11

The 11th pump iteration focused on the refinement of the impeller geometry. This pump concept was developed to deal with the primary issues of the previous concepts, which included flow separation and uneven velocity distribution in the blade channels.

Design The dimensions were chosen to achieve a velocity behavior which satisfy the de Haller criterion and minimize the flow separation (see Figure 3.16). Concurrently, the height of the impeller outlet h_2 was decreased, to aim for a more even velocity distribution, especially toward the outlet of the volume flow. In this process, the blade thickness on the trailing edge was increased to fulfill these requirements. The geometry of the volute was not further adjusted in this iteration.

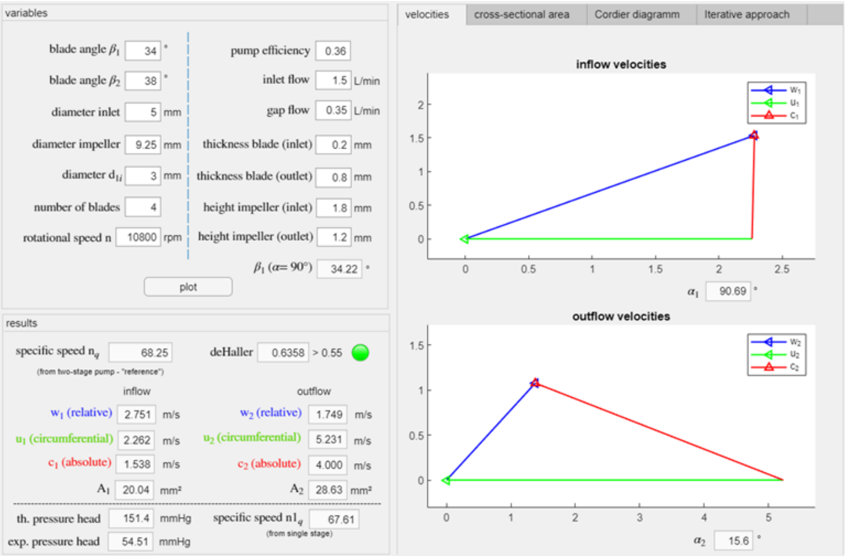

variables

blade angle β_1 34 °
blade angle β_2 38 °
diameter inlet 5 mm
diameter impeller 9.25 mm
diameter d_{1i} 3 mm
number of blades 4
rotational speed n 10800 rpm
pump efficiency 0.36
inlet flow 1.5 L/min
gap flow 0.35 L/min
thickness blade (inlet) 0.2 mm
thickness blade (outlet) 0.8 mm
height impeller (inlet) 1.8 mm
height impeller (outlet) 1.2 mm
β_1 (α= 90°) 34.22 °

results

specific speed n_q 68.25
(from two-stage pump - "reference")
deHaller 0.6358 > 0.55 ●

inflow
w_1 (relative) 2.751 m/s
u_1 (circumferential) 2.262 m/s
c_1 (absolute) 1.538 m/s
A_1 20.04 mm²

outflow
w_2 (relative) 1.749 m/s
u_2 (circumferential) 5.231 m/s
c_2 (absolute) 4.000 m/s
A_2 28.63 mm²

th. pressure head 151.4 mmHg
exp. pressure head 54.51 mmHg
specific speed $n1_q$ 67.61
(from single stage)

α_1 90.69 °
α_2 15.6 °

Figure 3.16: The 11th iterative calculation of the first pump concept with the respective parameters.

Performance The outcomes of the simulation for the 11th pump design indicated an average pressure head of 55.37 mmHg and a torque of $0.55 * 10^{-3}$ Nm, which lead to a pump efficiency of 31%. The flow field inside the impeller, which can be seen in Figure 3.17a and b, show a satisfactory distribution. A reduction in flow separation is present and the flow adheres more closely to the intended streamline towards the impeller outlet. The static pressure distribution visualised in Figure 3.17c indicates a well positioned volute cutwater because a high pressure area is formed at its face. However, the distribution in general still exhibits a non-uniform pattern, especially in the area of the volute.

Conclusion Since the velocity distribution in the blade channel of this pump iteration is satisfactory, the following iterations focused on the enhancement of the volute geometry.

Iteration 13

The 13th pump design featured a refined volute geometry which enhanced the overall velocity and pressure distribution. As stated before, the latest impeller design yielded satisfactory results, leading to the decision to maintain the geometrical parameters unchanged.

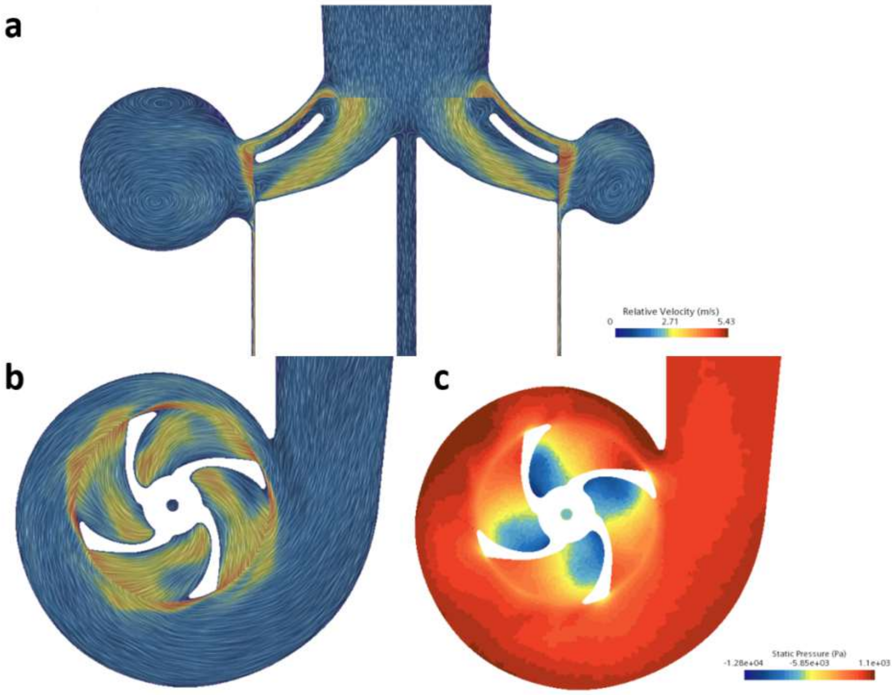

Figure 3.17: Simulation results of the 11th pump iteration of concept 1 with the (a) relative velocities in the XZ-plane, (b) relative velocities in the XY-plane and (c) the static pressure in the XY-plane.

Design Since the impeller design was not further adjusted, the analytical calculation of the pressure head, inflow and outflow velocities for this pump iteration are the same as shown in Figure 3.16. Modifications to the volute geometry included adjustment in both shape and size. The cross-sectional shape of the volute was refined, starting with a rounded rectangular shape near the volute cutwater, gradually transitioning over an elliptical to a circular shape towards the volute outlet. The diameter of the volute at 360° was further decreased to 5 mm. Furthermore, the diameter of the volute cutwater was decreased to 10 mm.

Performance The simulation results of this pump iteration yielded an averaged pressure head of 55.81 mmHg and torque of $0.56 * 10^{-3}$ Nm. These parameters define a pump efficiency of 29.6%. The pump efficiency was observed to decrease with further improvement of the design regarding a more even velocity and pressure distribution. This can be seen in Figure 3.18, which shows an improved velocity and pressure distribution compared to the previous simulation results. The relative velocities inside the impeller (see Figure 3.18a) show an improved uniform behavior across the height of the blade channel. Furthermore, the regions in close proximity to the blades, which can be seen in Figure 3.18b, are colored light blue in contrast to the dark blue regions of the preceding simulations. This suggests a decrease in flow separation, hence less flow stagnation zones. Finally, the static pressure distribution depicted in Figure 3.18c exhibits a uniform pattern surrounding the impeller. The pressure continuously increases with the distance to the pump's rotation axis.

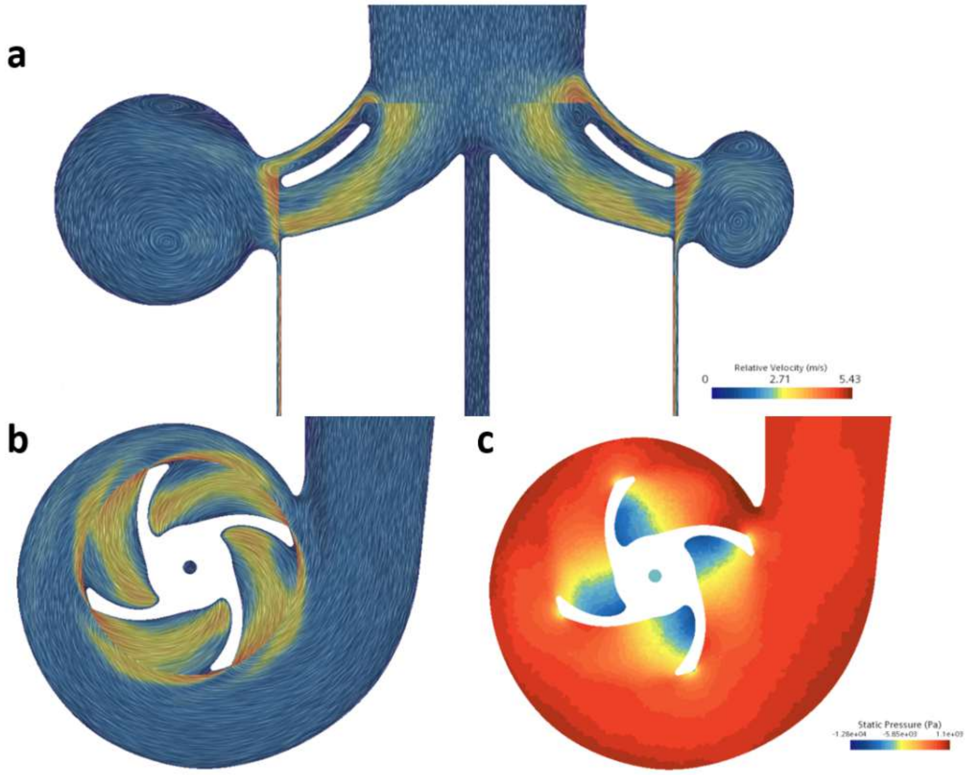

Figure 3.18: Simulation results of the 13th pump iteration of concept 1 with the (a) relative velocities in the XZ-plane, (b) relative velocities in the XY-plane and (c) the static pressure in the XY-plane.

When observing the mean static pressure (see Figure 3.19) a high-pressure point is visible exactly at the location of the volute cutwater, which indicates that its position is optimized for this pump design.

Conclusion This pump design was further considered as satisfactory, since the flow field was improved while fulfilling the previously described initial conditions for similarity. Therefore, the iteration process was completed.

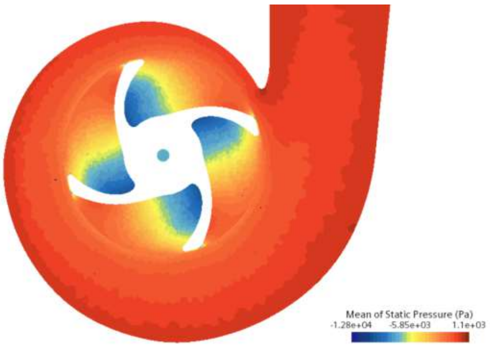

Figure 3.19: Mean static pressure distribution of the refined pump of concept 1 depicted in the XY-plane.

3.4.2 Concept 2 - equal impeller and volute geometry

This concept uses the same impeller und volute geometry as used in the two-stage pump. The idea was to build up the same pressure head with a single-stage pump with identical impeller design, by only increasing the rotation rate. Again, the affinity laws were used to scale the two-stage pump to a single-stage pump. The rotation rate n for this pump concept was initially determined utilizing equation 3.11 and the specific speed n_q of the two-stage pump. To achieve equal specific speed n_q, a rotation rate of 9080 rpm is needed. However, further revisions were made using the introduced calculation program, to adjust the blade angles $\beta_{1,2}$, to the corresponding rotation rate n. This action was necessary to achieve the same pressure head H while improving the flow field inside of the impeller and volute. The following subsections are providing a detailed description of the iterative process employed to refine this pump concept. This section focuses on the major changes that were instrumental in achieving the refined solution. The main parameters and results of the introduced concepts are summed up in Table 3.5.

Iteration 1

The 1st iteration of this pump concept focused on achieving an equal specific speed n_q as the two-stage pump in addition to the equal geometrical parameters. Hence, the previously calculated rotation rate of 9080 rpm was selected.

Design For the design of this pump concepts, the same geometrical parameters were used as in the two-stage pump, except the blade angles $\beta_{1,2}$. The calculation including the used parameters can be seen in Figure 3.20.

Table 3.5: Summary of the design parameters and respective results for each iteration described of concept 2.

parameters/iterations	**1**	**2**	**4**
n rpm	9080	8500	8500
β_1 °	35	37	37
β_2 °	32	33	33
c μm	100	100	105
H mmHg	**62.74**	**57.66**	**54.81**
η %	**27**	**28**	**27.2**

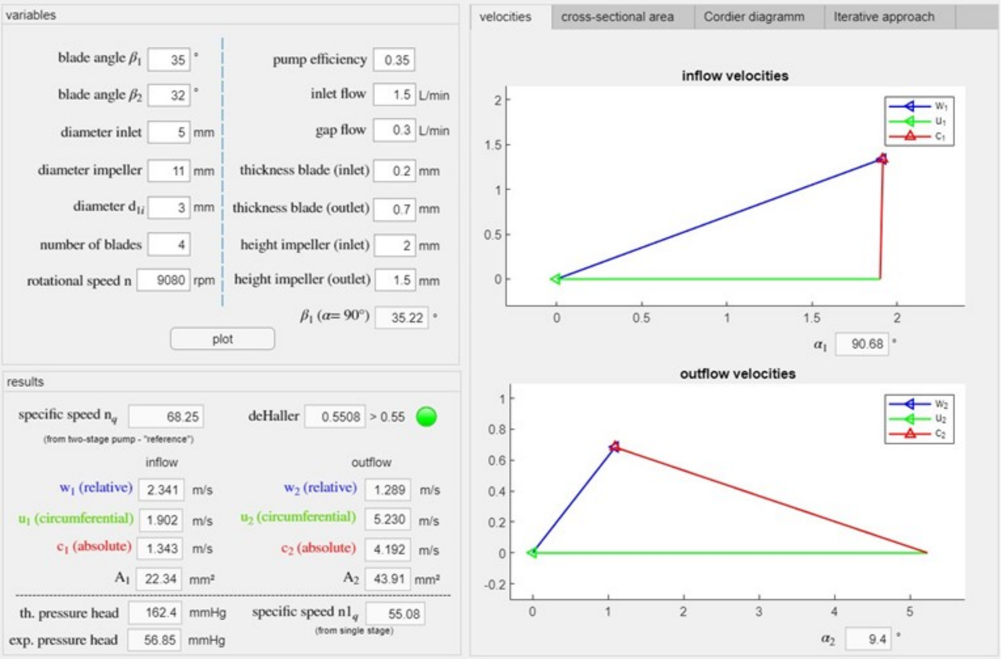

variables

blade angle β_1 35 °
blade angle β_2 32 °
diameter inlet 5 mm
diameter impeller 11 mm
diameter d_{1i} 3 mm
number of blades 4
rotational speed n 9080 rpm
pump efficiency 0.35
inlet flow 1.5 L/min
gap flow 0.3 L/min
thickness blade (inlet) 0.2 mm
thickness blade (outlet) 0.7 mm
height impeller (inlet) 2 mm
height impeller (outlet) 1.5 mm
β_1 (α= 90°) 35.22 °

results

specific speed n_q 68.25 (from two-stage pump - "reference")
deHaller 0.5508 > 0.55 ●

inflow
w_1 (relative) 2.341 m/s
u_1 (circumferential) 1.902 m/s
c_1 (absolute) 1.343 m/s
A_1 22.34 mm²

outflow
w_2 (relative) 1.289 m/s
u_2 (circumferential) 5.230 m/s
c_2 (absolute) 4.192 m/s
A_2 43.91 mm²

th. pressure head 162.4 mmHg
exp. pressure head 56.85 mmHg
specific speed $n1_q$ 55.08 (from single stage)

α_1 90.68 °
α_2 9.4 °

Figure 3.20: The 1st iterative calculation of the second pump concept with the respective parameters.

The hydrodynamic journal bearing was initially designed to exhibit the same length and radial clearance c as the two-stage pump. Hence, the clearance was designed with a width of 100 μm, which resulted in load-carrying capacities W summarized in Table 3.6. However, the relative difference in the load-carrying capacities between the two pump designs amounts to 18%.

Table 3.6: Bearing parameter comparison of the two-stage and the single-stage pump (1st iteration of concept 2).

	Two-stage pump		**Single-stage pump** **$d_2 =$ 11 mm** **$n =$ 9080 rpm**	
ε	$[W]$ N	$[P_{loss}]$ W	$[W]$ N	$[P_{loss}]$ W
0.85	4.22	0.31	4.97	0.57
0.8	3.14	0.27	3.70	0.50
0.75	2.48	0.25	2.93	0.45
0.7	2.04	0.23	2.40	0.42
0.65	1.72	0.21	2.02	0.40
0.6	1.47	0.20	1.73	0.38
0.55	1.26	0.19	1.49	0.36
0.5	1.09	0.19	1.29	0.35

Performance and conclusion The simulation results yielded an average pressure head H of 62.74 mmHg. Since the aim is to design a pump which generates approximately the same pressure head H as the two-stage pump, the analysis of the simulation results was not further continued. In this case, the relative error between the pressure heads amounts to 16.5%, whereas the maximum error accepted is 5%. Consequently, additional adjustments to the presented pump design were performed.

Iteration 2

To achieve a pressure head H in the range of the two-stage pump, the rotation rate n was decreased to 8500 rpm.

Design The blade angles $\beta_{1,2}$ were adjusted after selecting a new rotation rate n, until the de Haller criterion was satisfied. The parameters used in the 2nd pump iteration of concept 2 are visible in Figure 3.21.
For the bearing parameters, the radial clearance c was kept constant at 100 μm. The load-carrying capacities W decreased, due to the adjustment of the rotation rate n. The calculated values for the present pump design are shown in Table 3.7. However, the load-carrying capacities of the two-stage pump and this pump design

exhibit a relative difference of 11%.

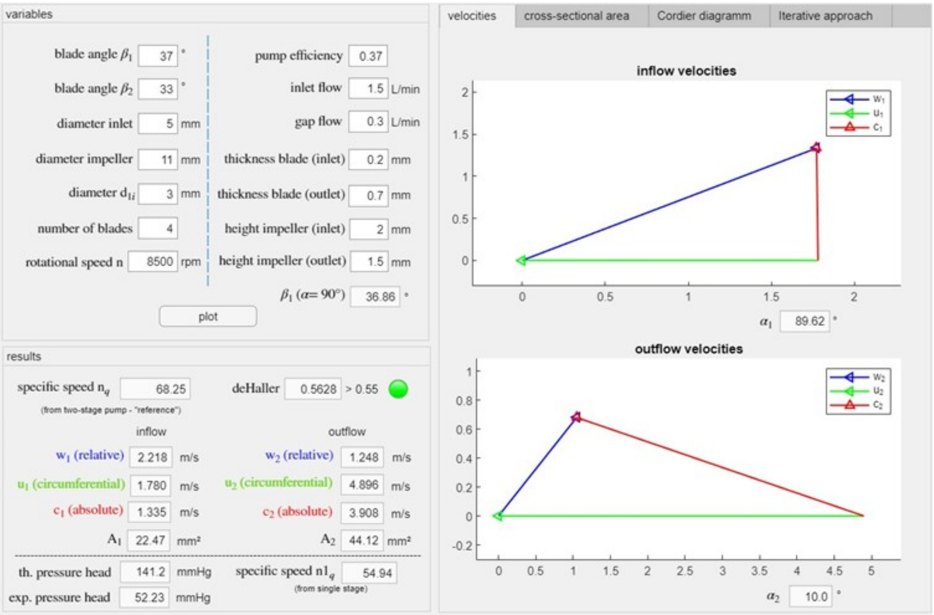

variables

blade angle β_1 37 °
blade angle β_2 33 °
diameter inlet 5 mm
diameter impeller 11 mm
diameter d_{1i} 3 mm
number of blades 4
rotational speed n 8500 rpm
pump efficiency 0.37
inlet flow 1.5 L/min
gap flow 0.3 L/min
thickness blade (inlet) 0.2 mm
thickness blade (outlet) 0.7 mm
height impeller (inlet) 2 mm
height impeller (outlet) 1.5 mm
β_1 (α= 90°) 36.86 °

results

specific speed n_q 68.25
(from two-stage pump - "reference")
deHaller 0.5628 > 0.55 ●

inflow
w_1 (relative) 2.218 m/s
u_1 (circumferential) 1.780 m/s
c_1 (absolute) 1.335 m/s
A_1 22.47 mm²

outflow
w_2 (relative) 1.248 m/s
u_2 (circumferential) 4.896 m/s
c_2 (absolute) 3.908 m/s
A_2 44.12 mm²

th. pressure head 141.2 mmHg
exp. pressure head 52.23 mmHg
specific speed $n1_q$ 54.94
(from single stage)

α_1 89.62 °
α_2 10.0 °

Figure 3.21: The 2nd iterative calculation of the second pump concept with the respective parameters.

Table 3.7: Bearing parameter comparison of the two-stage and the single-stage pump (2nd iteration of concept 2).

	Two-stage pump		**Single-stage pump** $\mathbf{d_2 = 11mm}$ $\mathbf{n = 8500rpm}$	
ε	$[W]$ N	$[P_{loss}]$ W	$[W]$ N	$[P_{loss}]$ W
0.85	4.22	0.31	4.69	0.51
0.8	3.14	0.27	3.49	0.45
0.75	2.48	0.25	2.76	0.41
0.7	2.04	0.23	2.27	0.38
0.65	1.72	0.21	1.91	0.35
0.6	1.47	0.20	1.63	0.34
0.55	1.26	0.19	1.41	0.32
0.5	1.09	0.19	1.22	0.31

Performance The simulation outcome indicated an average pressure head of 57.66 mmHg and a torque of $0.780 * 10^{-3}$ Nm. Subsequently, the efficiency of this pump design was determined to be at 28%. The developed relative velocities in the flow are shown in Figure 3.22a and b. As seen in the first iterative approaches of pump concept 1, the velocity distribution along the blade channel height is non-uniform and flow separation is occurring. Furthermore, some vortices can be seen in the cross-section of the volute, especially towards the outlet seen in Figure 3.22a. Such vortices are associated with increased friction and a decrease in efficiency [46]. The instantaneous static pressure distribution seen in Figure 3.22c exhibits a uniform pattern.

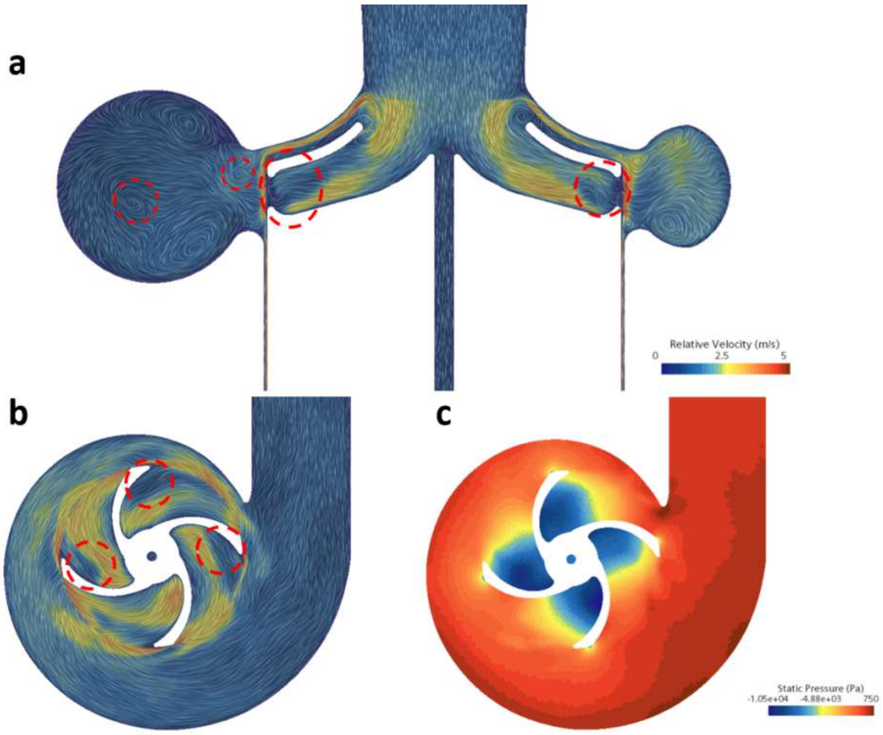

Figure 3.22: Simulation results of the 2nd pump iteration of concept 2 with the (a) relative velocities in the XZ-plane, (b) relative velocities in the XY-plane and (c) the static pressure in the XY-plane.

Conclusion The clearance c of the bearing gap has to be adjusted, to obtain a similar load carrying capacity W as the two-stage pump. This adjustment leads to a change in the flow field. Depending on the magnitude of the change, the blade angles $\beta_{1,2}$ must be adjusted for further improvement.

Iteration 4

In the 4th iteration of the pump design the radial clearance c was adjusted to achieve similar load-carrying capacities as in the two-stage pump.

Design In this pump design, the radial clearance c was increased to 105 μm. This minor change to the clearance gap did not affect the previously calculated improved blade angles $\beta_{1,2}$, while decreasing the relative difference in the load carrying capacities W to 1%. Therefore, the geometrical parameters for the impeller and the volute were not adjusted (see Figure 3.21). The resulting bearing performance parameters are shown in Table 3.8 in relation to the ones calculated for the two-stage pump.

Table 3.8: Bearing parameter comparison of the two-stage and the single-stage pump (4th iteration of concept 2).

	Two-stage pump		**Single-stage pump** $\mathbf{d_2 = 11mm}$ $\mathbf{n = 8500rpm}$	
ε	$[W]$ N	$[P_{loss}]$ W	$[W]$ N	$[P_{loss}]$ W
0.85	4.22	0.31	4.26	0.48
0.8	3.14	0.27	3.17	0.43
0.75	2.48	0.25	2.51	0.39
0.7	2.04	0.23	2.06	0.36
0.65	1.72	0.21	1.73	0.34
0.6	1.47	0.20	1.48	0.32
0.55	1.26	0.19	1.27	0.31
0.5	1.09	0.19	1.10	0.29

Performance The simulation results of this iteration yielded an average pressure head of 54.81 mmHg and a torque of $0.754 * 10^{-3}$ Nm, which resulted in a pump efficiency of 27.2%. Furthermore, the adjustment of the bearing parameters has caused an improvement to the pumps flow characteristic. Figure 3.23a shows a more uniform velocity distribution along the blade channel height. In comparison to the previous iterations less vortices can be seen in the volutes cross-section. Additionally, less flow separation is visible in close proximity to the impeller blades which can be seen in Figure 3.23b. Lastly, Figure 3.23c shows that the static pressure distribution remained uniform. The mean static pressure distribution depicted in Figure 3.24 shows a uniform distribution while the accumulated pressure point is located at the volute cutwater.

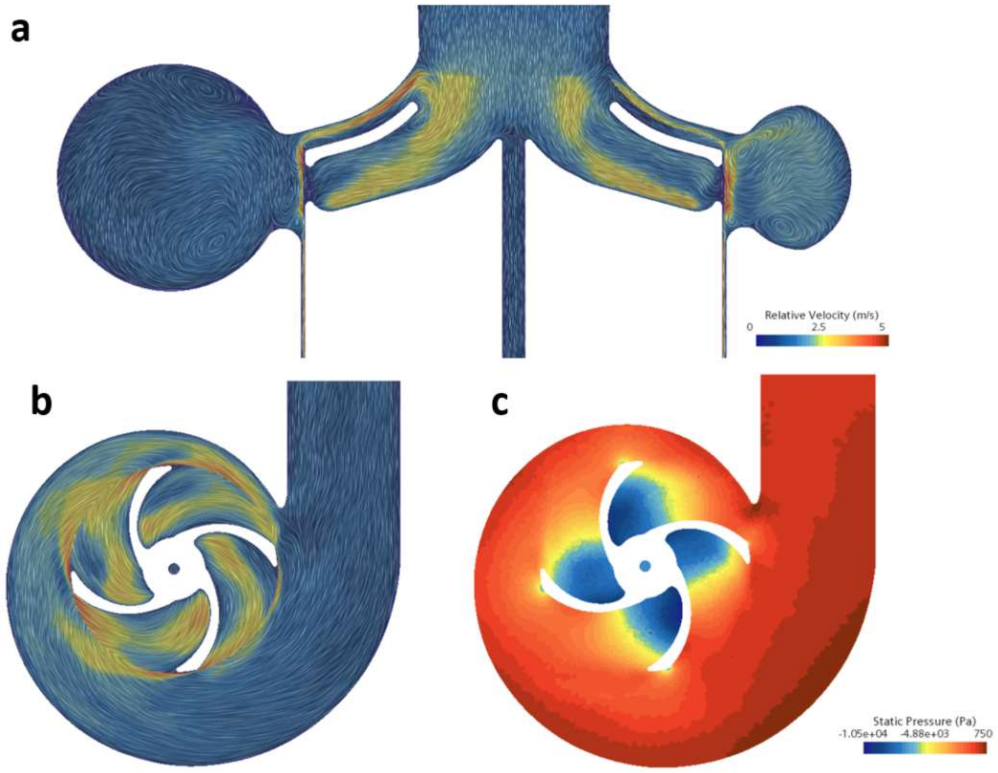

Figure 3.23: Simulation results of the 4th pump iteration of concept 2 with the (a) relative velocities in the XZ-plane, (b) relative velocities in the XY-plane and (c) the static pressure in the XY-plane.

Conclusion The calculation of the pump design showed that further adjustments of the blade angles $\beta_{1,2}$ did not improve the quality of the flow field. Therefore, the 4th pump iteration is regarded as the suitable pump design for concept 2.

3.5 Mesh independency

The simulation results were verified in the spatial domain through a comparative analysis of critical variables using additional simulations conducted with varying

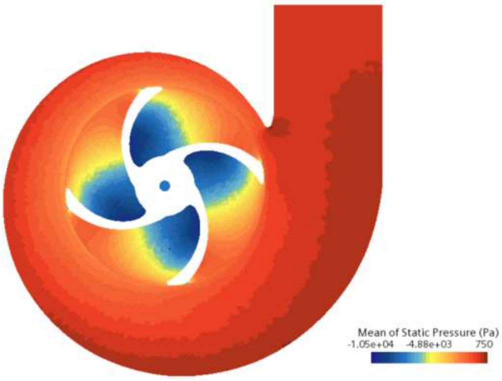

Figure 3.24: Mean static pressure distribution of the refined pump of concept 2 depicted in the XY-plane.

mesh sizes, including both a coarser and a finer mesh. Therefore, the grid convergence method was applied. The mesh independency was performed on the final pump design of concept 1, since both pump concepts exhibit a similar volume and utilize the same mesh input parameters. As for the observed variables the mean pressure head H and the mean torque T_m over one rotation after achieving convergence were compared. Table 3.9 contains the parameters used in this analysis, which were obtained by the simulations and the application of equations 2.23 - 2.25.

Table 3.9: Parameters used for the analysis of mesh independency.

pump volume $[V]$ m^3	$1.1394*10^{-6}$		
mesh size	coarse (3)	medium (2)	fine (1)
cell number $[N]$	673745	1716356	4635312
representative mesh size $[h]$	0.0119	0.0087	0.0063
grid refinement factor $[r]$	1.37	-	1.39
pressure head $[H]$ mmHg	55.34	55.81	56.27
torque $[T_m]$ Nm	$0.55610 * 10^{-3}$	$0.55583 * 10^{-3}$	$0.55797 * 10^{-3}$

Firstly, the pressure head H computed for each mesh size was compared. Therefore, equations 2.26 - 2.32 were applied to calculate the differences, approximate errors, and the GCI, which are summed up in Table 3.10.

Secondly, the simulated torque T_m for each mesh size was included in the comparative analysis. Again, equations 2.26 - 2.32 were utilized to calculate the parameters used to assess the mesh independency. Table 3.11 concludes a summary of the determined parameters.

Table 3.10: Calculation of the mesh independency analysis regarding the pressure head H computed using different mesh sizes.

mesh comparison	32	21
difference [ϵ]	-0.47	-0.46
approximate error [e_a] %	0.84	0.82
grid convergence index [GCI] %	12.7	11.6

Table 3.11: Calculation of the mesh independency analysis regarding the torque T_m computed using different mesh sizes.

mesh comparison	32	21
difference [ϵ]	$2.7{*}10^{-7}$	$-2.14{*}10^{-6}$
approximate error [e_a] %	0.049	0.38
grid convergence index [GCI] %	0.011	0.078

The approximate errors between both the solutions for the static pressure as well as the torque are below 1%. Additionally, the GCI values for the torque result in a low numerical uncertainty. However, the fine-grid convergence index of the pressure head shows a numerical uncertainty of 11.6% of the observed medium mesh solution. A possible influence for the high GCI values can be due to the continuously increasing pressure head with increasing mesh refinement. This indicates that the exact solution for the pressure head has not been found by the numerical simulations. Therefore, further mesh refinement was performed and subsequently analyzed.

To generate a finer mesh systematically, the base size of the cells was decreased by 33% while the number of the wall-near layers were increased by 33%. This operation resulted in a mesh comprising 6.2 million cells. However, the Grid Convergence Method is not applicable any longer because the grid refinement ratio calculated by equation 2.24 is below the 1.3 threshold. Nevertheless, the newly generated mesh is used to assess the mesh independency by calculating the approximate error between the solutions. Further grid refinement would increase the computational effort of the simulation, which exceeds the limited provided resources.

The simulation results for the refined mesh yielded a mean pressure head of 55 mmHg and a mean torque of $0.56 * 10^{-3}$. To compare the results of the three different sized meshes, the results were visualized as histograms in Figure 3.25. By analyzing the pressure head in Figure 3.25a, it is observable that the magnitude decreases in the finer mesh, which can be an indication for the numerical solution to oscillate around the exact solution. Additionally, the approximate error between the solutions for the pressure head of the meshes with highest and medium cell number is 2.31%, which is acceptable. The results for the mean torque in Figure 3.25b were also oscillating around a certain value, with an approximate error of 0.61% between the fine and medium mesh. Therefore, the mesh with a cell number of 4.6 million cells was chosen to provide sufficiently accurate simulation results.

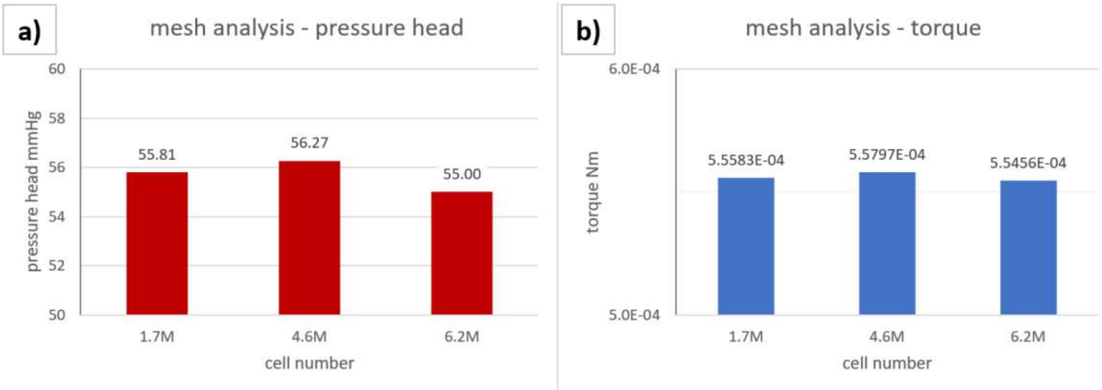

Figure 3.25: Analysis of the numerically calculated pressure head (a) and torque (b) for a coarse, medium and fine mesh.

3.6 Time-step independency

To assess the error caused by time discretization, the critical variables are computed by performing simulations with different time-step sizes. This time independency study was performed after assessing a suitable mesh size with the mesh independency study. These variables are compared to observe if further time-step refinement is needed to minimize the numerical uncertainty caused by time discretization. Since the simulation is based on the impeller rotation, the time-step sizes were selected to be equivalent to a 4°, 2°, and 1° rotation angle. As previously performed in the mesh independency, the variables used to assess time-step independency are the mean pressure head H and the mean torque T_m.

The results gathered by adjusting the time-step size are shown in Figure 3.26. Figure 3.26a depicts the computed pressure heads and Figure 3.26b the torque with decreasing time-step sizes. It is observable that the values are converging with increasing time-step refinement. However, since the approximate error between the 2° and the 1° time-step solution is 0.22% for the pressure head and 0.17% for the torque, a time-step corresponding to a 2° rotation is sufficiently accurate. A refinement of the time-step size would increase the computational effort with a low decrease expected in the numerical uncertainty. It also needs to be noted, that the computational power for this project was limited.

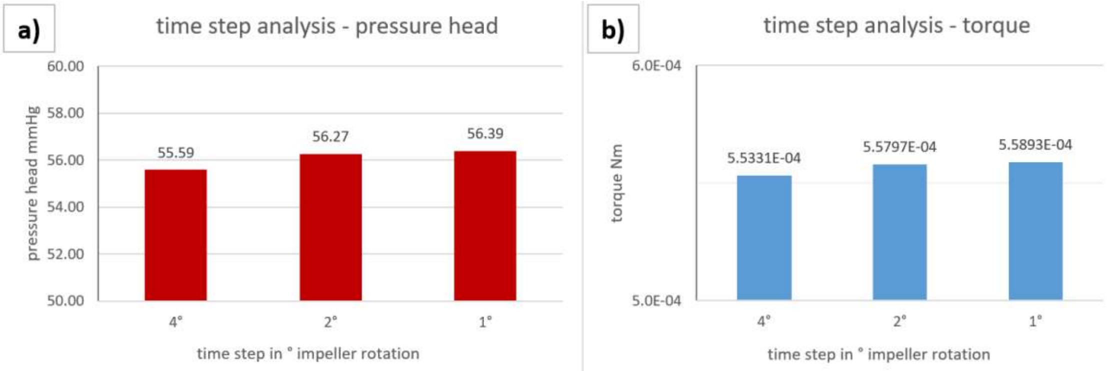

Figure 3.26: Analysis of the numerically calculated pressure head (a) and torque (b) for different time-steps, corresponding to 4°, 2° and 1° rotation of the impeller.

Chapter 4

Results

This master thesis evaluates the effectiveness of a two-stage configuration for a RBP relative to a single-stage concept. Therefore, focused analyses regarding the blood damage were performed. This chapter presents the final pump designs, the resulting values obtained by the CFD simulation and a relative comparison to the simulation results of the two-stage pump concept. The results of the two-stage pump concept have been provided by Sarah Linnemeier of the MUW.

4.1 Pump design and performance

In this section the final pump designs and results are summarized. The most important design parameters, which define the occurring shear stresses are comprised in Table 4.1.

Table 4.1: Comparison of important parameters of each pump design.

parameter	**two-stage**	**concept 1**	**concept 2**
volume V	3.7 ml	1.14 ml	1.4 ml
impeller diameter d_2	11 mm	9.25 mm	11 mm
rotation rate n	6400 rpm	10800 rpm	8500 rpm
circumferential velocity u_2	3.7 $\frac{m}{s}$	5.2 $\frac{m}{s}$	4.9 $\frac{m}{s}$
radial clearance c	100 μm	110 μm	105 μm

Figure 4.1 depicts the design of both single-stage pumps and the two-stage pump.

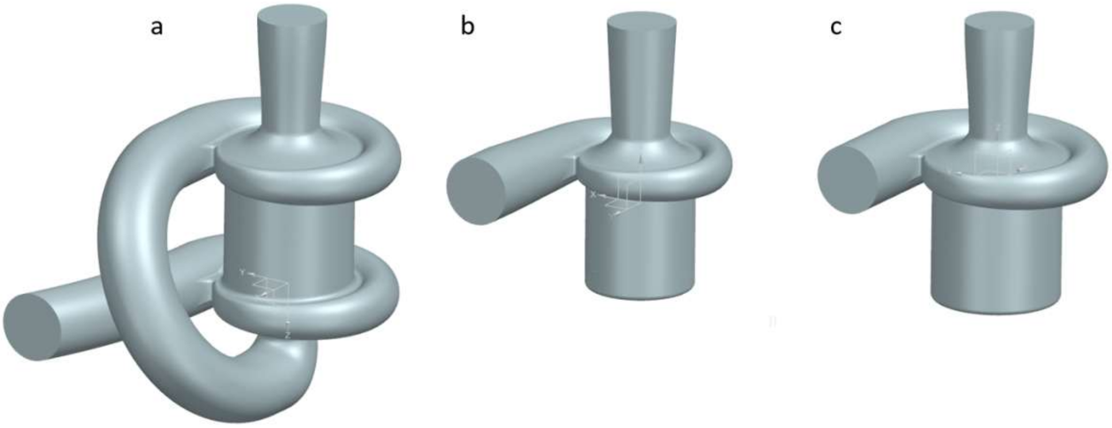

Figure 4.1: Design of the two-stage pump (a), the single-stage pump of concept 1 (b) and concept 2 (c).

4.1.1 Concept 1 – identical specific speed and specific diameter

The design of the final pump and its results are comprised in Table 4.2, where the index "1" is representative for the pump design of the first concept. This pump design entails a total volume of 1.14 ml, whereas the bearing and impeller hole geometry make up a volume of 0.0417 ml. The latter value represents 3.7% of the total volume.

Table 4.2: Main parameters of the single-stage pump based on concept 1.

Q_1	1.5 L/min	$d_{inlet,1}$	6 mm
H_1	56.27 mmHg	$d_{outlet,1}$	6 mm
n_1	10800 rpm	$h_{1,1}$	1.8 mm
z_{st}	1	$h_{2,1}$	1.2 mm
$z_{Bl,1}$	4	$e_{1,1}$	0.2 mm
$d_{1i,1}$	3 mm	$e_{2,1}$	0.8 mm
$d_{1a,1}$	5 mm	$\beta_{1,1}$	34°
$d_{2,1}$	9.25 mm	$\beta_{2,1}$	38°

The target value for the pressure head H, which was specified by the two-stage pump, was exceeded by this pump design. However, the relative error between the pressure heads of both pumps is around 4.5%. The different pressure head results in little differences in the specific speed and specific diameter, which amount to 66.03 and 1.73 respectively. This difference is additionally visualized in the Cordier-diagram, which can be seen in Figure 4.2.

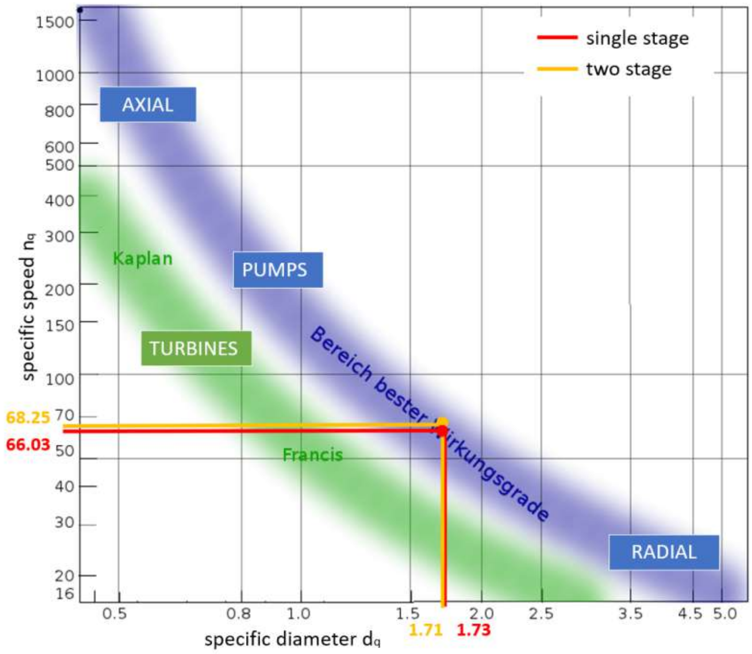

Figure 4.2: Cordier-diagram with the specific speed and diameter marked for the two-stage and single-stage pump of concept 1, respectively.

4.1.2 Concept 2 - equal impeller and volute geometry

The main parameters and results of the improved pump design are summerized in Table 4.3. Here, the index "2" marks the parameters corresponding to the design of concept 2. The total volume of this pump concepts design entails 1.4 ml. The bearing and impeller hole geometry entail a volume of 0.0563 ml, which constitutes 4% of the total volume.

In this concept, the relative difference in the pressure heads is 1.7%. Since this pump design demanded a reduction in the rotation rate to achieve a similar pressure head than the two-stage pump, the respective specific speeds are not equal. Furthermore, this pump concept did not focus to keep the specific diameter constant either. The values for the specific speed and diameter resulted in 53.04 and 2.04, respectively. Therefore, this pump concept is located in a different point in the Cordier-diagram, which can be seen in Figure 4.3.

Table 4.3: Main parameters of the single-stage pump based on concept 2.

Q_2	1.5 L/min	$d_{inlet,2}$	6 mm
H_2	54.76 mmHg	$d_{outlet,2}$	6 mm
n_2	8500 rpm	$h_{1,2}$	2 mm
z_{st}	1	$h_{2,2}$	1.5 mm
$z_{Bl,2}$	4	$e_{1,2}$	0.2 mm
$d_{1i,2}$	3 mm	$e_{2,2}$	0.7 mm
$d_{1a,2}$	5 mm	$\beta_{1,2}$	37°
$d_{2,2}$	11 mm	$\beta_{2,2}$	33°

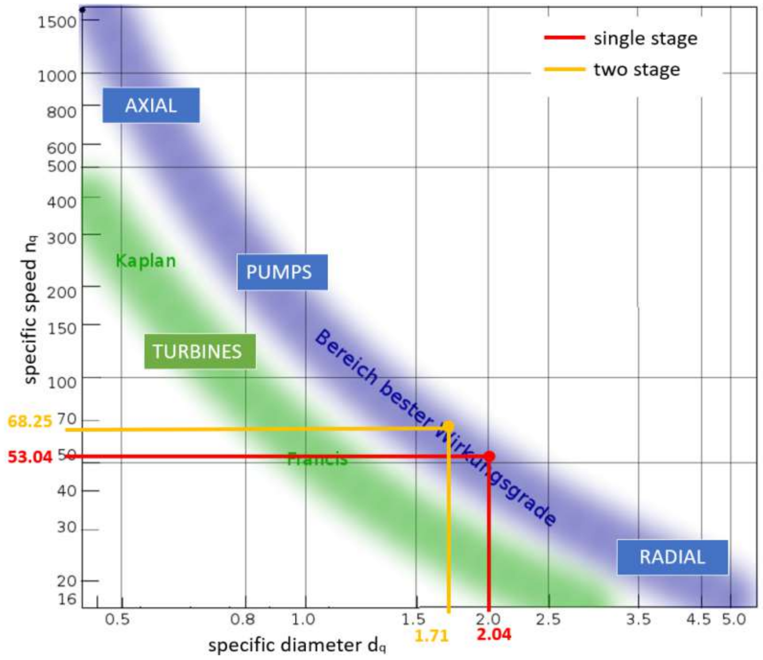

Figure 4.3: Cordier-diagram with the specific speed and diameter marked for the two-stage and single-stage pump of concept 2, respectively.

4.2 Shear stress analysis

The scalar shear stresses were computed at each time-step for each cell of the designed volume. They were analysed and processed into histograms for each concept. For this analysis the mean of the shear stresses computed in the time-steps over one impeller rotation were used.

4.2.1 Concept 1 – identical specific speed and specific diameter

The results for the mean shear stress distribution over the total volume of pump concept 1 are visualized in Figure 4.4. The total shear stresses shown in Figure 4.4c were split into the viscous and turbulent component, which can be seen in Figure 4.4a and b, respectively. Each histogram is composed of 16 bars, with a width of 100 Pa for the total and viscous shear stresses and 0.01 Pa for the turbulent shear stresses. The observed difference in magnitude between the total and the viscous shear stresses are attributed to the computed turbulent shear stresses, which show a comparatively low magnitude.

Compared to the two-stage pump, the shear stresses of the single stage pump exhibit a higher magnitude and reach up to 1600 Pa. However, the range from 1500-1600 Pa can be regarded as an overdramatization, since only the volume of a single cell is subjected to this shear stress. The results of both pump designs are combined in Figure 4.5. Since the difference between the total and viscous shear stresses are marginal, the comparison depicts only the viscous (see Figure 4.5a) and turbulent shear stresses (see Figure 4.5b). It is apparent, that in the single-stage pump more volume is subjected to shear stresses above 200 Pa compared to the two-stage pump. The portion of the pump volume experiencing shear stresses greater than the two-stage pump's maximum shear stress (1000 Pa) constitutes 0.0001% of the pump's total volume. Furthermore, the turbulent shear stresses are reaching higher magnitudes up to 0.16 Pa, while also exposing more volume to higher shear stresses in comparison to the two-stage pump.

The respective fluid volume, which is exposed to shear stresses above the thresholds of 9, 50 and 150 Pa, are depicted in Figure 4.6a. The data shows that 30% of the pump's volume (0.343 ml), are subjected to shear stresses exceeding 9 Pa. Furthermore, 5% (0.055 ml) are exposed to shear stresses over 50 Pa and 3% (0.031 ml) to over 150 Pa. Lastly, Figure 4.6b compares the computed data for the pump design of concept 1 to the data from the two-stage pump computations. While in the two-stage pump more volume is subjected to shear stresses above 9 Pa (17%, 0.64 ml) and 50 Pa (2%, 0.067 ml), more than 20 times less volume is subjected to shear stresses above 150 Pa (0.04%, 0.0014 ml).

In Figure 4.7 the shear stress distribution is visualized in the vertical cross-section of the single-stage pump (concept 1) and the two-stage pump. The color bar was

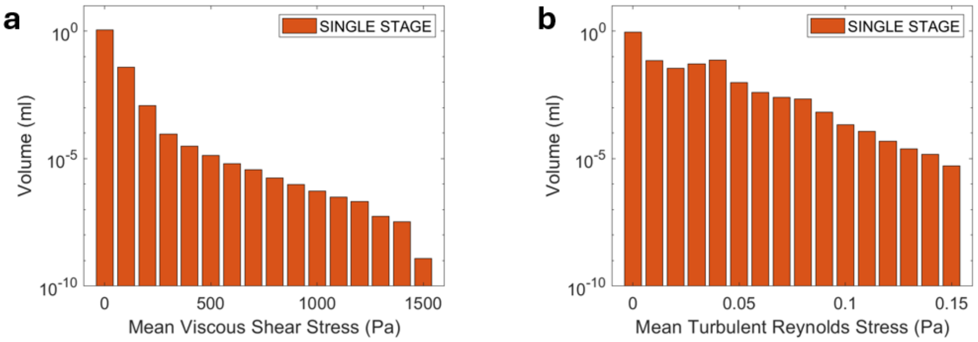

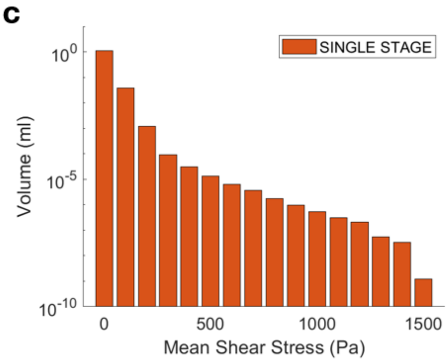

Figure 4.4: Mean shear stresses computed for pump concept 1, subdivided in (a) viscous, (b) turbulent and (c) total shear stress.

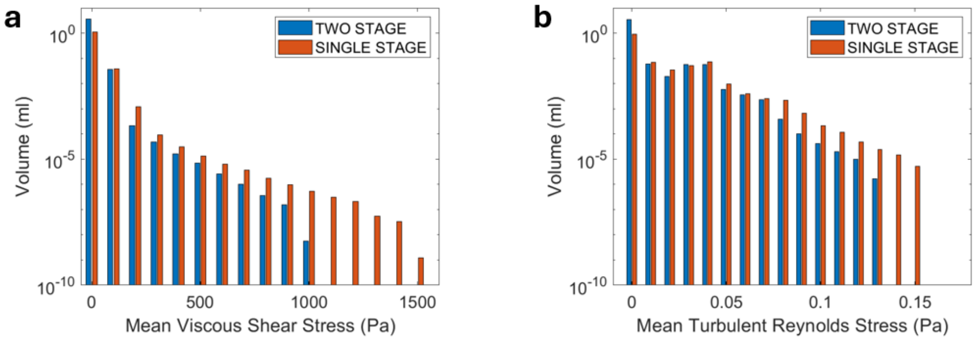

Figure 4.5: Comparison of the mean shear stresses computed for pump concept 1 and the two-stage pump, subdivided in (a) viscous and (b) turbulent shear stress.

defined to visualize stresses up to 150 Pa, since it defines the threshold where hemolysis starts to occur. It is apparent that in the single-stage pump the shear stress magnitudes inside the bearing gap, at wall-near regions inside the blade channel and at the pump housing surrounding the impeller shroud are higher in comparison to the two-stage pump.

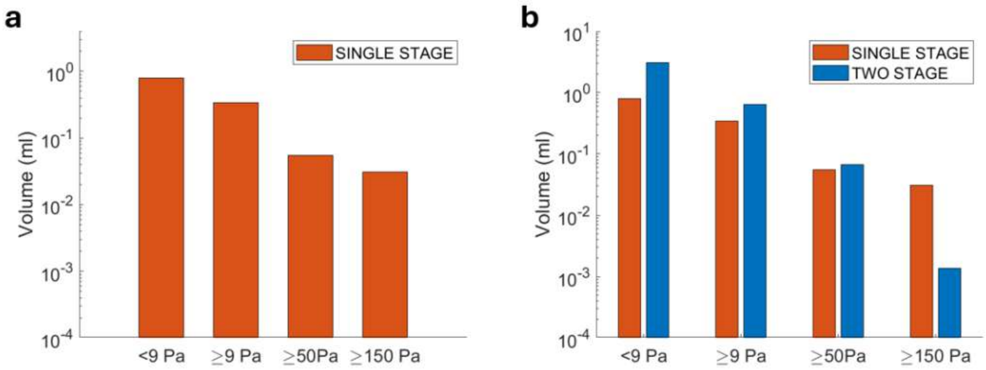

Figure 4.6: The volume of pump concept 1 (a), which is exposed to the respective shear stress thresholds of the introduced blood components. Further, a comparison to the shear stresses exposed to the pump volume of the two-stage pump (b) is presented.

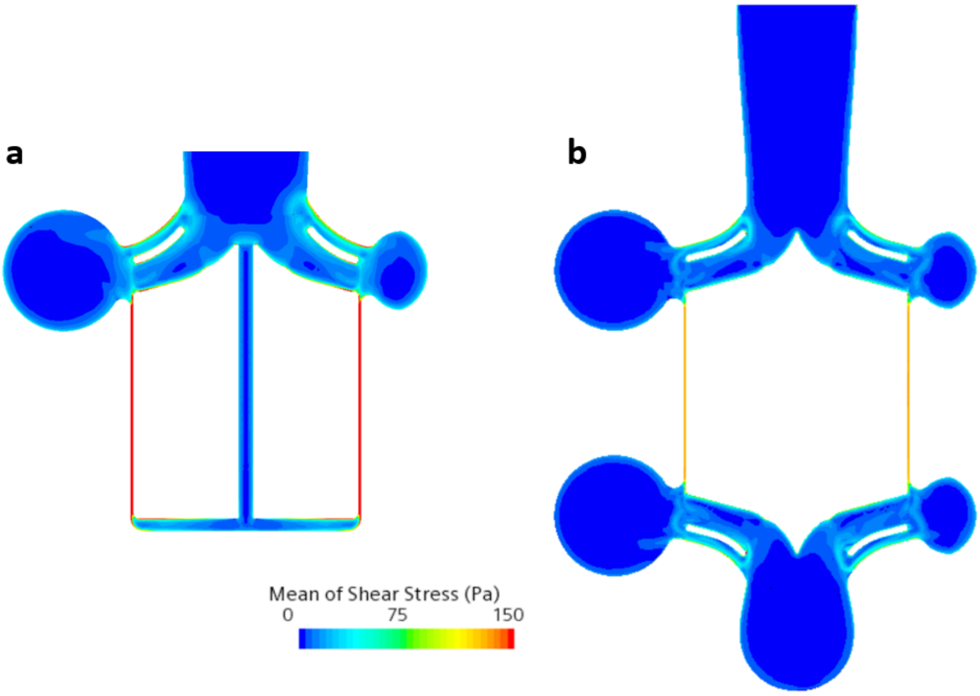

Figure 4.7: Mean shear stress distribution in the vertical cross-section of pump concept 1 (a) and the two-stage pump (b).

The occurring wall shear stresses are quantified in histograms, illustrated in Figure 4.8. Furthermore, the wall shear stresses from the single-stage pump of concept 1 (see Figure 4.8a) are compared to the ones in the two-stage pump (see Figure 4.8b). In the comparison a higher wall shear stress magnitude is seen in the single-stage pump, which reaches up to 1600 Pa.

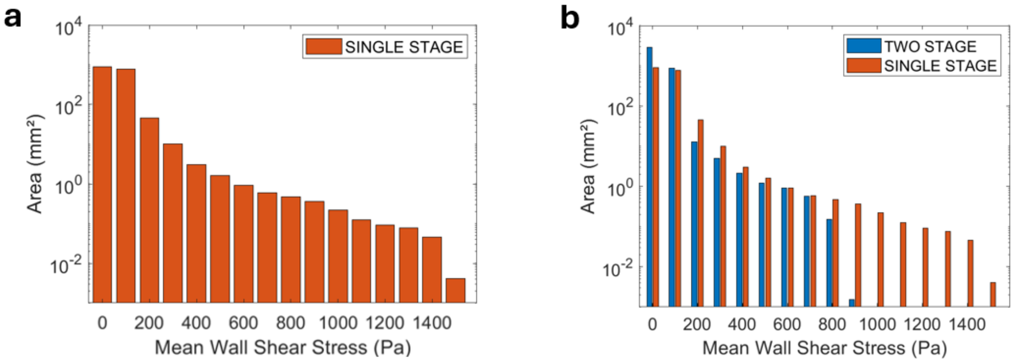

Figure 4.8: Wall shear stress distribution of pump concept 1 (a) and comparison with the wall shear stresses occurring in the two-stage pump (b).

The geometrical distribution of the wall shear stresses inside the pump design of concept 1 is visualized in Figure 4.9. In the pump design of concept 1, regions like the bearing gap, parts of the impeller blade channel, the pump housing above the impeller shroud, as well as the leading and trailing edge are subjected to wall shear stresses above 150 Pa. For further comparison, Figure 4.10 visualizes the wall shear stresses occurring in the two-stage pump. In the two-stage pump, the impeller leading and trailing edge and small parts of the pump housing show wall shear stresses above 150 Pa. The bearing region shows wall shear stresses around 100 Pa.

4.2.2 Concept 2 - equal impeller and volute geometry

The resulting mean shear stress distribution over the total volume of pump concept 2 is visualized in Figure 4.11. As seen in the illustration of the previous pump concept, the shear stress distributions are subdivided into the viscous (see Figure 4.11a) and turbulent parts (see Figure 4.11b), as well as the total shear stress distribution (see Figure 4.11c).

While the bar width remained constant, the shear stress distribution of pump concept 2 is composed out of 14 bars for the total and viscous part, and 17 bars for the turbulent. The reduction of the number of bars in the total and viscous shear stress distribution resulted from the smaller maximum shear stress (1400 Pa) in this pump concept. However, only small volumina in the magnitude of $2 * 10^{-7}$, which constitute 0.00001% of the total pump volume, are subjected to shear stresses above 1000 Pa.

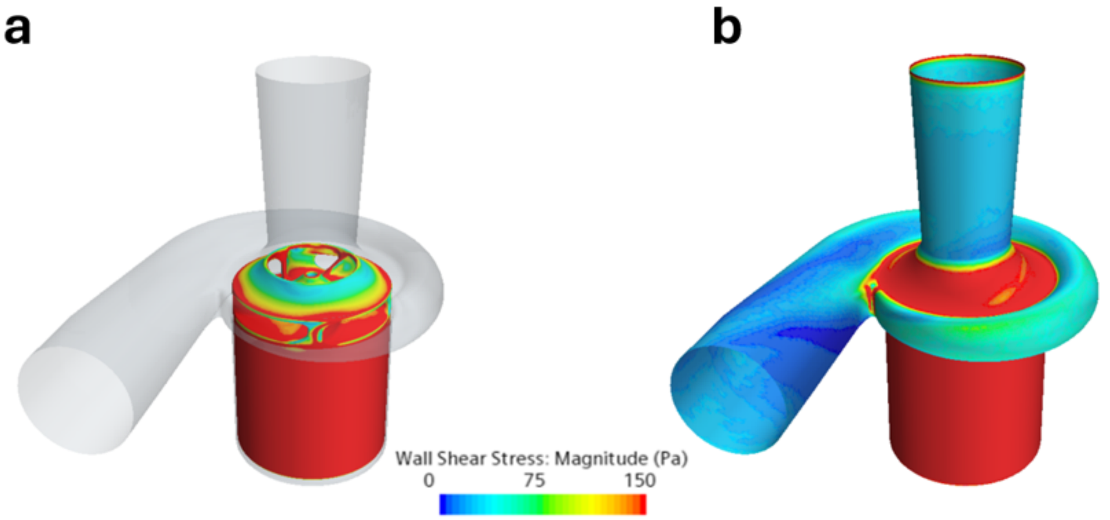

Figure 4.9: Geometrical distribution of the wall shear stresses occurring in the pump design of concept 1 on the area of the impeller (a) and the area of the pump housing (b).

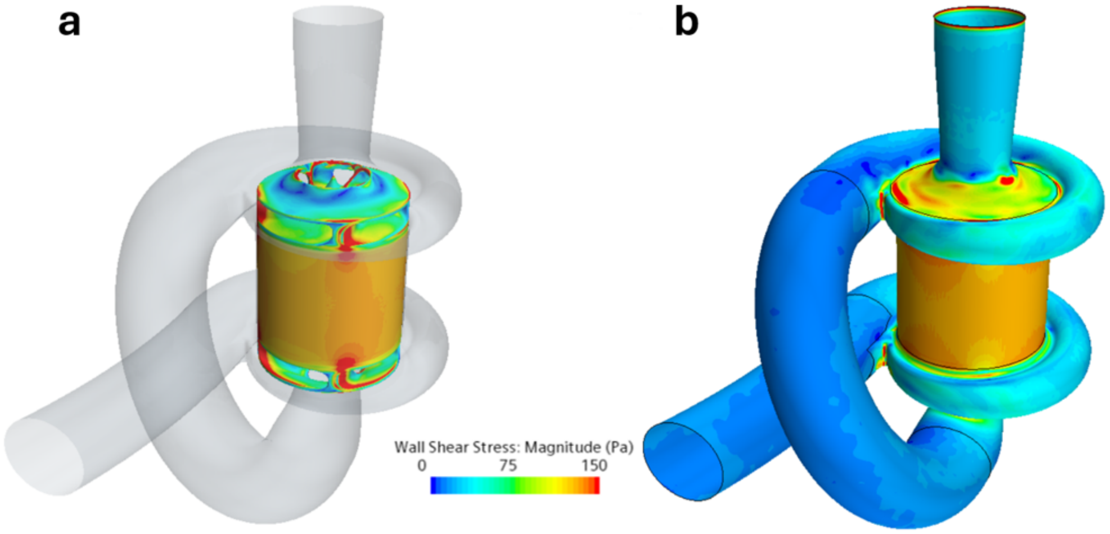

Figure 4.10: Geometrical distribution of the wall shear stresses occurring in the two-stage pump on the area of the impeller (a) and the area of the pump housing (b).

Figure 4.12 depicts the comparison of the shear stress distributions of the two-stage pump and pump concept 2. As previously described, only the viscous (see Figure 4.12a) and turbulent shear stress distributions (see Figure 4.12b) are depicted. In comparison to the two-stage pump, more volume is subjected to shear stresses

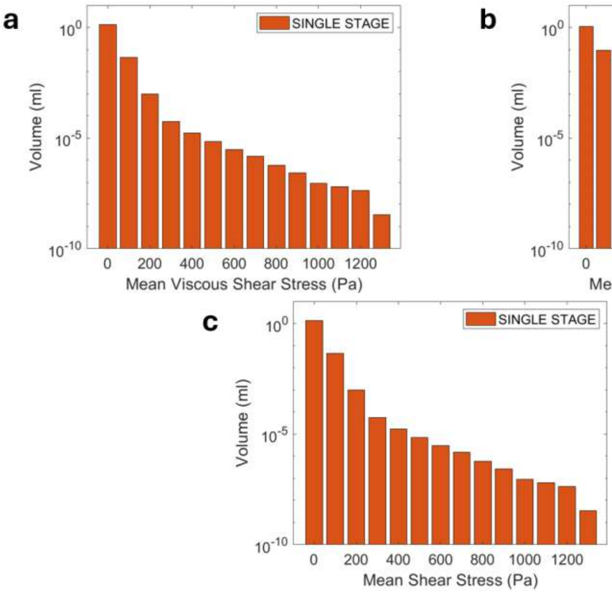

Figure 4.11: Mean shear stresses computed for pump concept 2, subdivided in (a) viscous, (b) turbulent and (c) total shear stress.

above 100 Pa. Similar volumes are exposed to shear stresses between 300 and 700 Pa. Additionally, the turbulent shear stresses reached up to 0.17 Pa, while in the two-stage pump a maximum of 0.14 Pa was computed. In this single-stage pump concept more volume is subjected to turbulent shear stresses above 0.01 Pa.

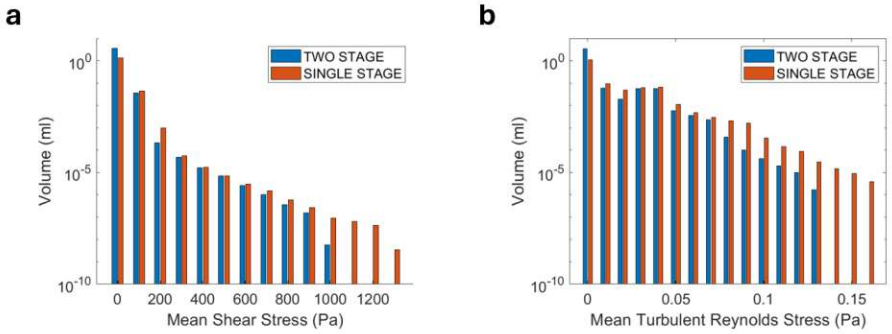

Figure 4.12: Comparison of the mean shear stresses computed for pump concept 2 and the two-stage pump, subdivided in (a) viscous and (b) turbulent shear stress.

Figure 4.13a illustrates the respective fluid volume exposed to shear stresses exceeding the thresholds of 9, 50, and 150 Pa. The analysis reveals that 30% of the pump's volume (0.427 ml), are exposed to shear stresses exceeding 9 Pa. Shear stresses exceeding 50 Pa impact 5% of the pump's volume (0.072 ml), whereas

2.5% of the volume (0.036 ml) is subjected to shear stresses greater than 150 Pa. Figure 4.13b shows a comparison of the results analyzed for pump concept 2 with the results from the two-stage pump. As seen in the comparison with pump concept 1, less volume of this pump concept is subjected to shear stresses above 9 Pa. However similar volume is subjected to shear stresses above 50 Pa (0.072 ml vs. 0.067 ml). The volume, which is subjected to shear stresses above 150 Pa, is approximately 25 times larger than in the two-stage pump (0.036 ml vs 0.0014 ml).

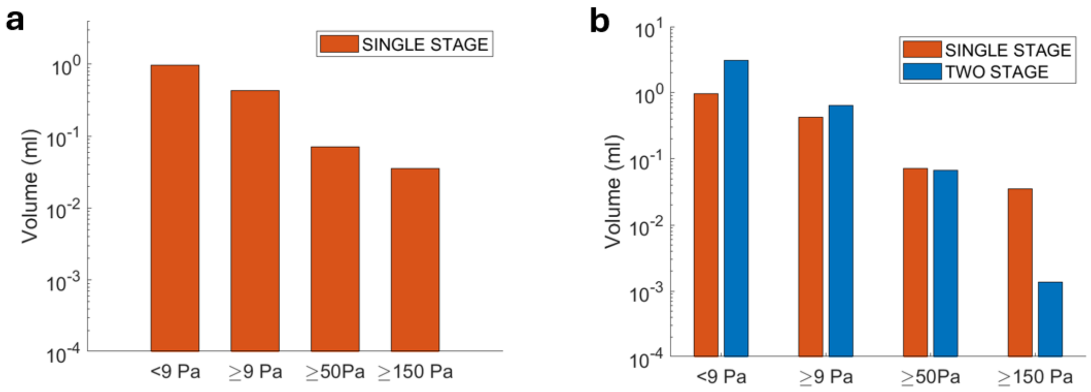

Figure 4.13: The volume of pump concept 2 (a), which is exposed to the respective shear stress thresholds of the introduced blood components. Further, a comparison to the shear stresses exposed to the pump volume of the two-stage pump (b) is presented.

Figure 4.14 visualizes the shear stress distribution in the vertical cross-section of the single-stage pump (concept 2) and the two-stage pump. A similar shear stress distribution is visible, as shown in the pump design of concept 1 (see Figure 4.7). Higher shear stresses are occuring in the bearing gap, the blade channel and the pump housing located over the impeller shroud compared to the two-stage pump. The wall shear stress distribution in pump concept 2 is illustrated in Figure 4.16a. Furthermore, this distribution is compared to the wall shear stress distribution in the two-stage pump, which is depicted in Figure 4.16b). As in the comparison with pump concept 1, a higher wall shear stress magnitude is seen in pump concept 2, which reaches up to 1100 Pa.
The geometrical distribution of the wall shear stresses inside the single-stage pump of concept 2 is visualized in Figure 4.15. Regions such as the bearing gap, impeller blade channel, parts of the pump housing, the leading and trailing edge are subjected to wall shear stresses above 150 Pa.

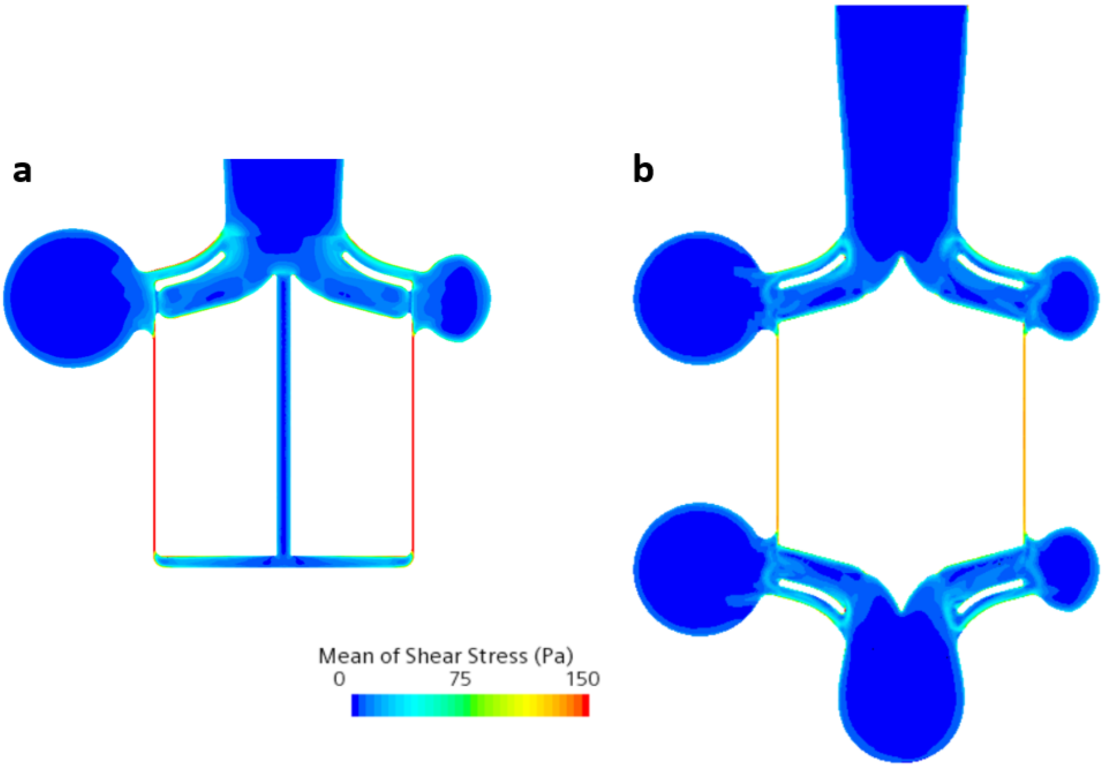

Figure 4.14: Mean shear stress distribution in the vertical cross-section of pump concept 2 (a) and the two-stage pump (b).

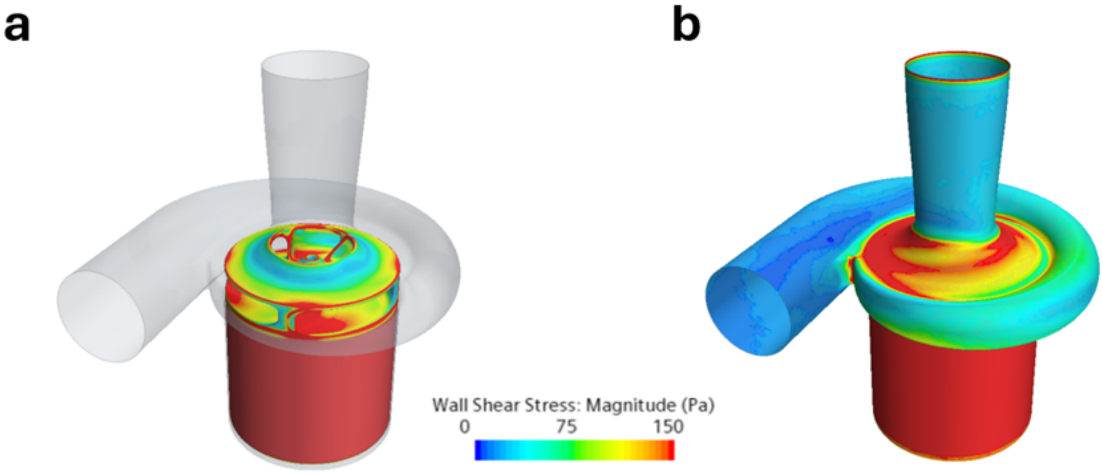

Figure 4.15: Geometrical distribution of the wall shear stresses occurring in the pump design of concept 2 on the area of the impeller (a) and the area of the pump housing (b).

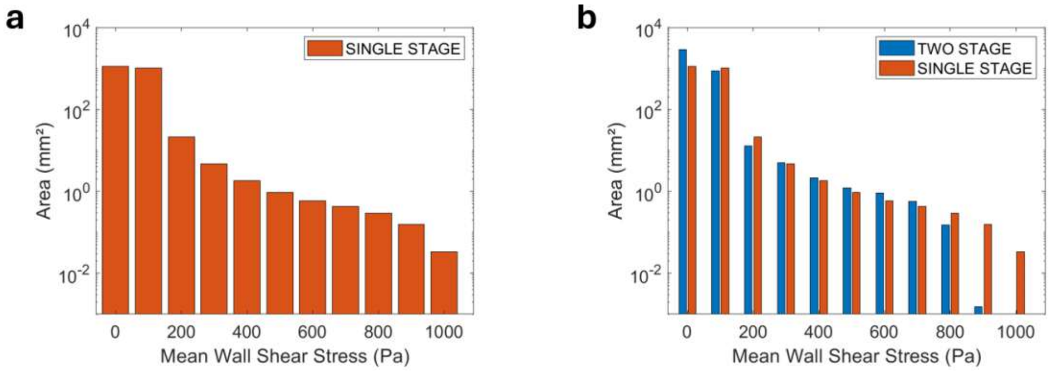

Figure 4.16: Wall shear stress distribution of pump concept 2 (a) and comparison with the wall shear stresses occurring in the two-stage pump (b).

4.3 Hemolysis and washout

This chapter presents the simulation results for the hemolysis. Therefore, the $mgNIH$ was calculated utilizing equations 3.6-3.10 over the computed time. Additionally, the $mgNIH$ values computed by the two-stage pump are presented to allow a comparison. The two-stage pump's washout was simulated over 30 rotations. In contrast, both single-stage pump concepts were simulated to perform 60 rotations, since the washout of the bearing and impeller hole geometry was not sufficiently simulated after 30 rotations.

The washout per time is presented by tracking the presence of 'old blood' throughout the pump volume. Furthermore, the washout of the bearing and impeller hole geometry is illustrated in separate charts.

4.3.1 Concept 1 – identical specific speed and specific diameter

Figure 4.17 depicts the evolution of the $mgNIH$ value of the first pump concept over the time. After the simulated 60 rotations, a value of 6.4 mg/100L is calculated. However, the values are continuously increasing and the curve is still rising with approximately 0.9 mg/100L per 0.1 s. This implicates that the solution did not converge and higher values for the $mgNIH$ are to be expected. The $mgNIH$ of the two-stage pump exhibits lower values throughout the computation, and reaches a final value of 3.7 mg/100L. The slope of the curve indicates that the $mgNIH$ is still rising, however, in comparison to the single-stage pump in a lower magnitude

(0.24 mg/100L per 0.1 s).

The volumetric percentage of old blood present in the total pump volume, of pump concept 1 and the two-stage pump, in relation to time is depicted in Figure 4.18. A 90% washout of the pump concept 1 is achieved at around 0.054 seconds, which coincides with 10 impeller rotations. The two-stage pump achieves a 90% washout after 0.145 seconds, which coincides with approximately 16 impeller rotations due to the lower rotation rate. Figure 4.19 and Figure 4.20 are observing the washout in the bearing gap and impeller hole, respectively. The washout in the bearing gap starts after 3 (0.016 s) and 23 rotations (0.13 s), respectively for the planes at the top and bottom as illustrated in 3.5. In the geometry of the hole, the washout starts after 29 rotations (0.16 s) at the bottom plane and after 32 rotations (0.23 s) at the top plane.

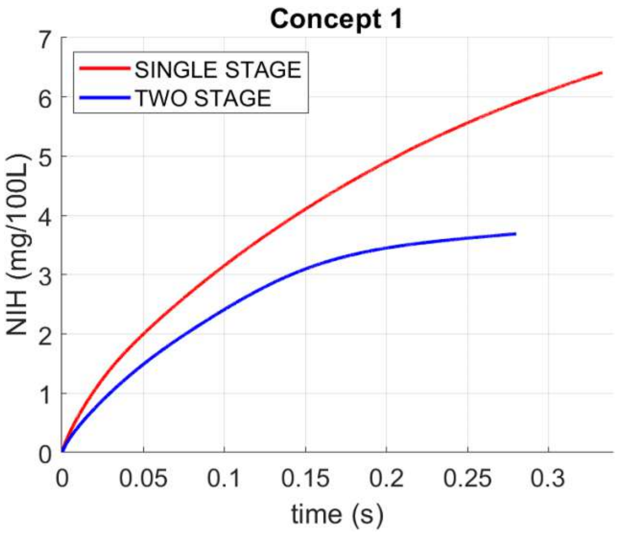

Figure 4.17: Comparison of the $mgNIH$ of pump concept 1 and the two-stage pump.

The washout of the entire bearing gap and impeller hole did not cross the 90% threshold after the limited number of rotations simulated. Therefore, the trend of the respective curve is computed, by calculating the percentage of washout per 0.1 seconds. The analysis focuses on the last 0.1 seconds of the simulated pump rotation. Table 4.4 comprises a summary of the percent washout per 0.1 seconds for each surface area, which can be interpreted as the trend of the respective curve. Since the bearing surface nearest to the blade channel had a washout of 97%, only a small increase of 1.88% is expected if additional 0.1 seconds are simulated. In the planes on the bottom of the bearing, as well as the bottom and top of the hole,

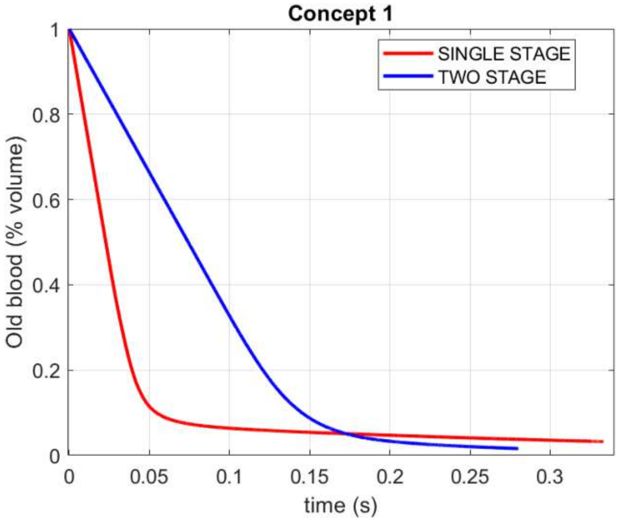

Figure 4.18: Percentage washout of the total pump volume of pump concept 1 in comparison to the washout of the two-stage pump.

the washout is expected to increase around 24-25% per 0.1 seconds. Figure 4.21 visualizes the washout after the final time-step in the vertical cross-section of the pump. It can be seen, that mostly the bearing region below the impeller and the hole exhibit an insufficient washout.

The velocity distribution was examined for mean velocities below the stagnation threshold of 0.1 $\frac{m}{s}$. In this pump concept, only wall near regions showed velocities below 0.1 $\frac{m}{s}$. Special observations were performed to the geometries of the bearing gap and the impeller hole. The velocity vector in the bearing gap indicated velocities above 2 $\frac{m}{s}$. However, the velocity component normal to the introduced planes (see Figure 3.5) have a magnitude of 0.04 $\frac{m}{s}$. In the impeller hole, the velocities normal to the cross-sectional plane are around 0.47 $\frac{m}{s}$. The volume, which exhibits mean relative velocities below 0.1 $\frac{m}{s}$, constitutes 0.115% of the total pump volume (0.001315 ml).

4.3.2 Concept 2 - equal impeller and volute geometry

The temporal progress of the $mgNIH$ of pump concept 2 compared to the $mgNIH$ of the two-stage pump is visualized in Figure 4.22. After the final rotation of the single-stage pump, a value of 8.3 mg/100L is computed, which is higher than the $mgNIH$ value of 3.7 mg/100L of the two-stage pump. Both curves for the $mgNIH$ are still rising with progressing time, which furthermore indicates missing

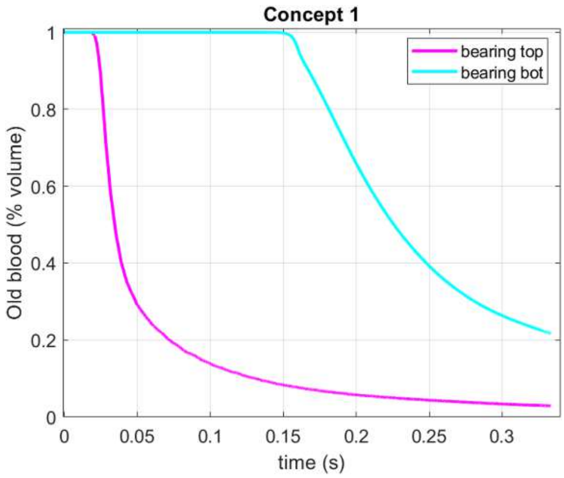

Figure 4.19: Percentage washout of the observed cross-sections located at the top and the bottom of the bearing gap in pump concept 1.

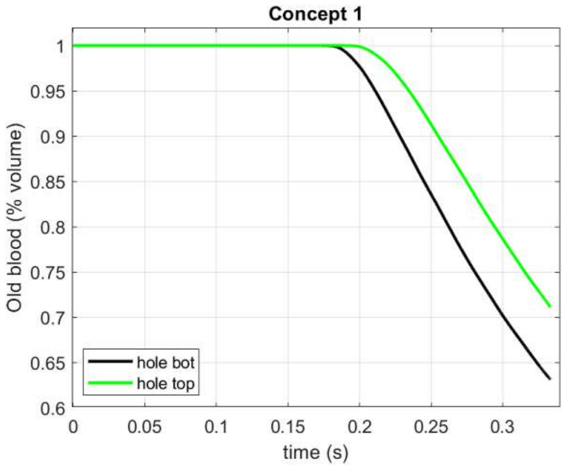

Figure 4.20: Percentage washout of the observed cross-sections located at the top and the bottom of the hole in pump concept 1.

Table 4.4: Analysis of the percentage washout per 0.1 seconds in the critical bearing and impeller hole geometries of pump concept 1.

surface	% washout per 0.1s
bearing top	1.88 %
bearing bot	24.62 %
hole bot	25.36 %
hole top	24.15 %

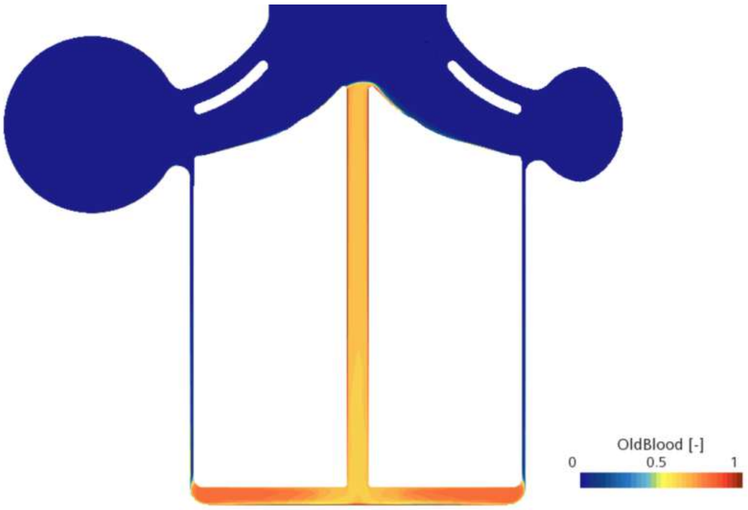

Figure 4.21: Illustration of the washout of pump concept 1, visualized in the vertical cross-sectional plane.

convergence. The $mgNIH$ of this pump concept increases by 0.95 mg/100L per 0.1 s in contrast to the increase of 0.24 mg/100L in the two-stage pump.
The washout capability of the pump was analyzed by observing the total pump volume and the critical geometries of the bearing and impeller hole, as performed in the prior pump concept. The simulated washout of the single-stage pump's total pump volume compared to the washout of the two-stage pump is shown in Figure 4.23. After 0.078 seconds, which is equivalent to approximately 11 rotations, the single-stage pump performs a washout of 90%. In comparison, the 90% washout of the two-stage pump takes 0.145 seconds, which coincides with approximately 16 impeller rotations. The washout of the bearing gap and the impeller hole are visualized in Figure 4.24 and Figure 4.25, respectively. In this pump concept, the newly introduced blood at the inlet takes 2 impeller rotations (0.015 s) to reach the bearing gap top plane, while it takes 22 impeller rotations (0.16 s) to reach the bottom plane. The washout at the bottom and top plane of the hole starts after 27 (0.19 s) and 29 impeller rotations (0.21 s).

The analysis of the washout results regarding the second pump concept exhibits a washout of the observed critical regions below 90%. To compensate the lack of information regarding the time point when 90% of the blood in these regions is washed out, the trend of these curves was computed. Table 4.5 summarizes the percent washout per 0.1 seconds by analyzing the results in each surface area. Given that the bearing surface closest to the blade channel achieved a 99% washout,

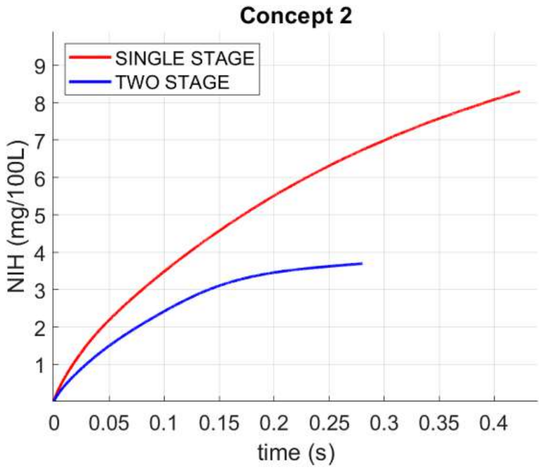

Figure 4.22: Comparison of the $mgNIH$ of pump concept 2 and the two-stage pump.

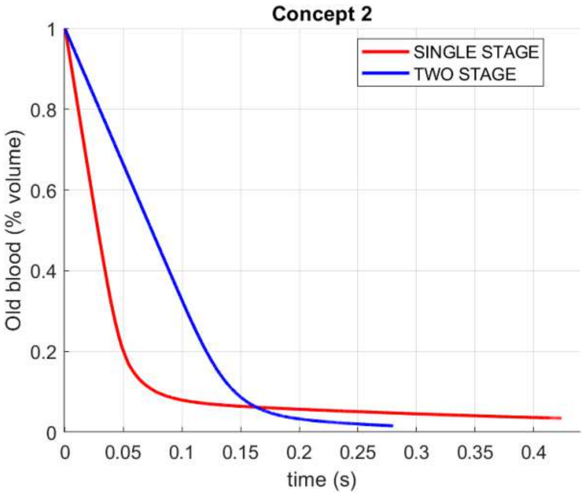

Figure 4.23: Percentage washout of the total pump volume of pump concept 2 in comparison to the washout of the two-stage pump.

an additional simulation of 0.1 seconds is anticipated to yield an increase of 0.75%. Conversely, for the planes at the bearing's bottom and both the bottom and top of the hole, the washout is projected to increase by approximately 15-20% in the next 0.1 seconds. In Figure 4.26 the washout in the vertical cross-section of the pump after the final time-step is shown. The depicted washout looks similar as in the pump design of concept 1 (see Figure 4.21), that is characterized by the insufficient washout of the bearing region below the impeller and the hole.

In this pump concept, the velocity distribution was examined for stagnation zones with velocities below 0.1 $\frac{m}{s}$. The distribution highlighted the bearing gap alongside

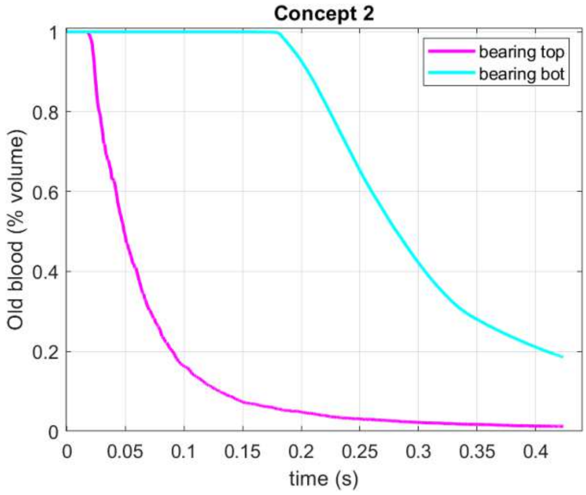

Figure 4.24: Percentage washout of the observed cross-sections located at the top and the bottom of the bearing gap in pump concept 2.

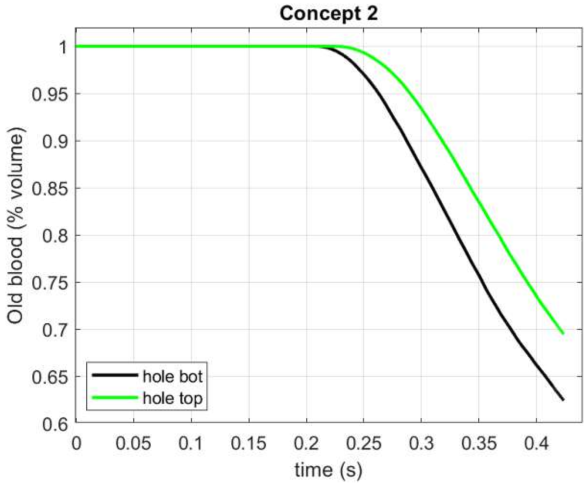

Figure 4.25: Percentage washout of the observed cross-sections located at the top and the bottom of the hole in pump concept 2.

the wall near regions to exhibit velocities below 0.1 $\frac{m}{s}$. The velocities in the bearing gap had values below 0.04 $\frac{m}{s}$ in the direction normal to the cross-sectional plane. However, the absolute velocity vector has a magnitude of around 2.5 $\frac{m}{s}$. In the impeller hole, the velocities normal to the cross-sectional plane were same as in pump concept 1 with 0.47 $\frac{m}{s}$. The portion of the pump volume displaying mean relative velocities under 0.1 $\frac{m}{s}$ accounts for 0.097% of the total pump volume (0.00136 ml).

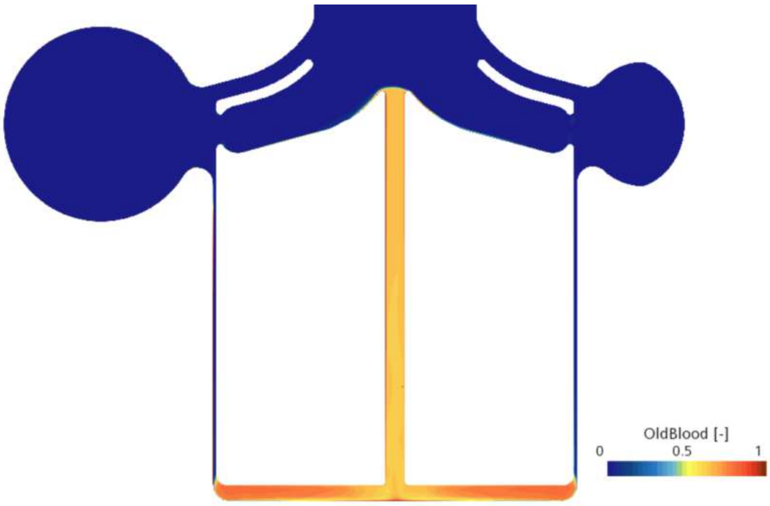

Figure 4.26: Illustration of the washout of pump concept 2, visualized in the vertical cross-sectional plane.

Table 4.5: Analysis of the percentage washout per 0.1 seconds in the critical bearing and impeller hole geometry of pump concept 2.

surface	**% washout per 0.1s**
bearing top	0.75 %
bearing bot	15.41 %
hole bot	19.43 %
hole top	19.28 %

Chapter 5

Discussion

In this thesis, two different pump designs were developed, which exhibit similarities with the currently developed two-stage RBP by the MUW. These pumps were compared to the two-stage pump with regard to the generated pressure head, pump efficiency, and blood damaging potential. Thereby, it can be determined whether an enhanced hemocompatibility justifies the increased volume and complexity associated with the two-stage pump concept. The following discussion of the results is divided into the interpretation of the results, the limitation of this study and suggestions for future work.

5.1 Interpretation of the results

Both developed single-stage pump concepts generate a similar pressure head (H_1= 56.27 mmHg, H_2= 54.81 mmHg) as the two-stage pump (H_{2S}= 53.87 mmHg), with a relative difference below 5%. The rotation rate was increased by 69% and 33%, for concepts 1 and 2 respectively, to facilitate the pressure head with only a single stage. Based on the Cordier-diagram, the specific speed and diameter of the developed pumps indicate that the pump designs are located in the area of highest efficiency (see Figures 4.2, 4.3). However, a reduction in pump efficiency is observable in both developed pump concepts compared to the two-stage pump. This is caused by higher friction losses due to the increased rotation rates. Furthermore, the iterative refinement of the pump design is accompanied by a reduction in efficiency, which is linked to the establishment of the special operating conditions of a RBP (no stagnation zones, uniform flow distribution, etc.).

Shear stresses of higher magnitude were observed in both pump concepts compared to the two-stage pump. Maximum mean shear stresses of 1600 and 1400 Pa were computed for the pumps of concept 1 and 2, respectively, whereas the two-stage pump has maximum values of 1000 Pa. Irrespective of the blood's residence time, these values indicate an increase in blood damage in comparison to the two-stage pump (see Figure 4.17 and 4.22). However, the volumes subjected to shear stresses above 1000 Pa constitute 0.0001% and 0.00001% of the total pump volume of pump concept 1 and 2, respectively. Furthermore, it is shown that in both pump concepts, less volume ($\Delta V_{1,9Pa}$= -0.3 ml, $\Delta V_{2,9Pa}$= -0.21 ml) is subjected to shear stresses above 9 Pa compared to the two-stage pump. A similar volume is subjected to 50 Pa, while more volume ($\Delta V_{1,150Pa}$= 0.03 ml, $\Delta V_{2,150Pa}$= 0.035 ml) is subjected to shear stresses above 150 Pa. It has to be noted that the volume of the two-stage pump is approximately 3 times larger than the developed single-stage pumps.

Progressing to the blood damage analysis, conducted with the power law by Heuser and Opitz [40], it is apparent that both single-stage pump concepts yield a higher $mgNIH$ value, with 6.4 and 8.3 mg/100L for pump concept 1 and 2, respectively. Thus, the blood damage potential of the two-stage pump, with an $mgNIH$ of 3.7 mg/100L, is the lowest of all the investigated pumps. The curves characterizing the $mgNIH$ are still rising to an undefined plateau. However, the slopes of the $mgNIH$ curves of the single-stage pumps are nearly 4 times higher than that of the two-stage pump. The rise is expected to be linked to the insufficient washout of the bearing and impeller hole geometry. The $mgNIH$ values obtained from experiments with the HeartMate III (HM III) and the HeartWare VAD (HVAD) are around 5 mg/100L and 10 mg/100L, respectively, at their optimal operating points [71]. Granegger et al. [72] researched the capability of the HVAD to be used in pediatric patients. The computed $mgNIH$ values were 37 mg/100L, while operating at conditions adjusted to the physiology of a small pediatric patient. It is apparent that the present computed values of the two pump concepts are located between the $mgNIH$ values of both the HM III and the HVAD. However, the computed $mgNIH$ curves did not converge to a final comparable value.

The time and rotations to perform a 90% washout of the total pump volume are lower in both pump concepts compared to the two-stage pump. The pump design of concept 1 has the fastest 90% washout with 0.054 seconds (10 rotations), which is correlated to the lowest volume of 1.14 ml. Followed by the pump design of concept 2 with a 90% washout time of 0.078 seconds (11 rotations) and lastly the two-stage pump with 0.145 seconds (16 rotations). In comparison, the 90% washout of the HVAD takes 0.6 seconds (22 rotations), applied in pediatric operating conditions [72]. However, the washout of the bearing gap and the impeller hole was insufficient after the computed time in both pump concepts.

Stagnation zones were primarily found in wall-near regions in all of the investigated pumps. The velocity vector in the bearing gap of each single-stage pump concept has a magnitude of 0.04 $\frac{m}{s}$ in the direction normal to the cross-sectional plane. Whereas the absolute velocities in the bearing gap exhibit a magnitude of around 2.5 $\frac{m}{s}$. The bearing geometry of the two-stage pump facilitates a flow with velocities of 0.1 $\frac{m}{s}$ in the direction normal to the cross-sectional plane. The lower velocities at the wall-near regions were predictable since the velocity towards static walls drops to 0 $\frac{m}{s}$. However, the lower velocities in the bearing gap in the direction normal to the cross-sectional plane were not anticipated to be below 0.1 $\frac{m}{s}$. These velocities explain the unsatisfactory results for the washout of the bearing region. Therefore, the bearing gaps of both designed pumps exhibit increased risk of thrombus formation and growth. Amongst other complications, thrombi can lead to pump thrombosis and impede the function of a VAD [73]. The bearing geometry needs to be improved to facilitate velocities above 0.1 $\frac{m}{s}$. The velocity vectors normal to the cross-sectional plane of the hole in both single-stage pump designs have a magnitude of 0.47 $\frac{m}{s}$ and therefor pose no risk for stagnation. The insufficient washout of the hole is correlated to the low velocities in the bearing gap, because the new blood reached the hole geometry just after 26 impeller rotations.

5.2 Limitations

In the following section, the limitations of this thesis are presented, which are crucial for understanding and interpreting the results.

- The improvements of the pump designs were performed by iterative adjustments and not by mathematical optimization.
- The improvements of the pump designs were performed in a single operating point and did not consider different operating conditions.
- The results were obtained by numerical simulations of the flow and no experimental data was available for validation. However, the used methodology is

established within the research group at the MUW.

- The comparison of certain variables, such as the $mgNIH$, are not convincing, since the data did not converge after the computed time.
- The simulation setup was simplified, for example, by assuming a constant mass flow, compared to the real environment inside a human body.
- The bearing geometry was calculated by applying the theory of hydrodynamic journal bearings. Influencing factors such as the increased width of the clearance gap and the impeller propulsion by an electric motor were not considered. Since the motor was not included in this analysis, factors such as the impeller stability, forces and heat transfer were not considered.
- The accuracy of the manufacturing process of small VADs, using durable and biocompatible materials, was not considered.

5.3 Future work

Additional CFD simulations are needed to assess the converged $mgNIH$ value of the pump concepts as well as to evaluate the progression of the washout in the critical geometries. These values can further be interpreted and compared to the two-stage pump and similar VADs.

Adjustments to the bearing geometry should be performed to achieve velocities above the stagnation threshold. This would not only diminish the stagnation zones in the bearing but also improve the washout. However, the bearing of the newly designed pump loses its comparability to the one in the two-stage pump due to differences in the load-carrying capacities. Additionally, the motor design is required and its interaction with the pump needs to be analyzed.

The feasibility of manufacturing the presented pump designs needs to be investigated. Furthermore, experiments have to be conducted utilizing the designed pumps to validate the simulation results and extrapolate information to perform further improvements.

Chapter 6

Conclusion

The design of two distinct single-stage pumps were established, which share similarity with the two-stage pump concept, currently developed by the MUW. Both designs were further refined by iterative adjustments based on CFD simulations. The refined pump designs were further compared to the two-stage pump, to assess potential benefits of a multi-stage concept for a RBP.

When compared to a two-stage concept, it is evident that similar pressure heads can be achieved at the same volume flow, but with a slight decrease in efficiency. However, it has to be stated that the reduction of a single stage led to a reduced volume of the pump by up to 69%.

The investigation showed that the single-stage pumps had fewer blood volume exposed to shear stresses above 9 Pa, which represents the activation threshold of the vWF. However, similar blood volume is exposed to shear stresses above 50 Pa, while more blood volume was exposed to shear stresses higher than 150 Pa, which indicates increased hemolysis risk. Generally, the shear stresses simulated in the single-stage pumps reached higher magnitudes (up to 1600 Pa) than in the two-stage pump.

In terms of blood damage, the $mgNIH$ value of pump concept 1 and 2 were approximately 2 times higher than for the two-stage pump. Furthermore, convergence did not occur in both computed curves for the $mgNIH$, which hinders a final statement and comparison. The missing convergence is correlated with the insufficient washout of the bearing geometry. Stagnation zones were assessed only in wall-near regions of the single-stage pumps, which coincides with the outcomes of the two-stage pump. Therefore, the design of the bearing geometry needs to be improved in regards of velocities and washout. The design of the two-stage pump benefits the washout of the bearing gap. Experimental testing has to be conducted with all the investigated pumps to validate the simulation results.

The two-stage pump design exhibits lower shear stresses and a more consistent washout throughout the volume. However, this is accompanied by an increased pump volume, which can be limited in the design process due to spatial limitations for the implant.

The advancement of VADs tailored for pediatric patients is of utmost importance, as it offers a life-saving bridge to transplantation or recovery, and enhances the quality of life. This research not only paves the way for innovative medical solutions but also holds the promise of transforming pediatric cardiac care, offering hope and new possibilities for children facing heart failure.

Bibliography

[1] Savarese, G., and Lund, L. (2017). Global Public Health Burden of Heart Failure. *Cardiac failure review 3(1)*, 7–11.

[2] Ündar, A., Wang, S., Özyüksel, A., and Rossano, J. W., Chapter 9 - Pediatric devices In *Mechanical Circulatory and Respiratory Support*, Gregory, S. D., Stevens, M. C. S., and Fraser, J. F., Eds.; Academic Press: 2018, pp 271–297.

[3] Rossano, J. W., Kim, J. J., Decker, J. A., Price, J. F., Zafar, F., Graves, D. E., Morales, D. L., Heinle, J. S., Bozkurt, B., Towbin, J. A., Denfield, S. W., Dreyer, W. J., and Jefferies, J. L. (2012). Prevalence, Morbidity, and Mortality of Heart Failure–Related Hospitalizations in Children in the United States: A Population-Based Study. *Journal of Cardiac Failure 18*, 459–470.

[4] Wittlieb-Weber, C. A., Lin, K. Y., Zaoutis, T. E., O'Connor, M. J., Gerald, K., Paridon, S. M., Shaddy, R. E., and Rossano, J. W. (2015). Pediatric Versus Adult Cardiomyopathy and Heart Failure-Related Hospitalizations: A Value-Based Analysis. *Journal of Cardiac Failure 21*, 76–82.

[5] Malik, A., Brito, D., Vaqar, S., and Chhabra, L., *Congestive Heart Failure.* Treasure Island (FL): StatPearls Publishing: 2023.

[6] Dipchand, A. I., and Laks, J. A. (2020). Pediatric heart transplantation: long-term outcomes. *Indian journal of thoracic and cardiovascular surgery 36*, 175–189.

[7] Garbade, J., Barten, M., Bittner, H., and Mohr, F. (2013). Heart transplantation and left ventricular assist device therapy: two comparable options in end-stage heart failure? *Clinical Cardiology 36*, 378–382.

[8] Nesta, M., Cammertoni, F., Bruno, P., and Massetti, M. (2021). Implantable ventricular assistance systems (VAD) as a bridge to transplant or as 'destina-

tion therapy'. *European heart journal supplements : journal of the European Society of Cardiology 23*, E99–E102.

[9] Fraser, K. H., Zhang, T., Taskin, M. E., Griffith, B. P., and Wu, Z. J. (2012). A Quantitative Comparison of Mechanical Blood Damage Parameters in Rotary Ventricular Assist Devices: Shear Stress, Exposure Time and Hemolysis Index. *Journal of Biomechanical Engineering 134*, 081002.

[10] Song, X., Throckmorton, A., Untaroiu, A., Patel, S., Allaire, P., Wood, H., and Olsen, D. (2003). Axial flow blood pumps. *ASAIO journal (American Society for Artificial Internal Organs : 1992) 49*, 355–64.

[11] Marey, G., McHugh, K., Sakhitab-Kerestes, A., Jang, S., MS, M., John, R., Richtsfeld, M., Said, S., Ameduri, R., and Griselli, M. (2019). HeartMate III as a Bridge to Transplantation in an Adolescent With Failed Fontan Circulation. *JACC: Case Reports 1*, DOI: 10.1016/j.jaccas.2019.09.013.

[12] O'Connor, M., Lorts, A., Davies, R., Fynn-Thompson, F., Joong, A., Maeda, K., Mascio, C., McConnell, P., Mongé, M., Nandi, D., Peng, D., Rosenthal, D., Si, M., Sutcliffe, D., VanderPluym, C., Viegas, M., Zafar, F., Zinn, M., and Morales, D. (2020). Early experience with the HeartMate 3 continuous-flow ventricular assist device in pediatric patients and patients with congenital heart disease: A multicenter registry analysis. *J Heart Lung Transplant. 39(6)*, DOI: 10.1016/j.healun.2020.02.007.

[13] Conway, J., St. Louis, J., Morales, D. L., Law, S., Tjossem, C., and Humpl, T. (2015). Delineating Survival Outcomes in Children <10 kg Bridged to Transplant or Recovery With the Berlin Heart EXCOR Ventricular Assist Device. *JACC: Heart Failure 3*, 70–77.

[14] Woolley, J. R., Dady, S., Spinnato, J., Sanchez-de-Toledo, J., Miller, E., Morelli, B., Winowich, S., and Wearden, P. D. (2013). First Berlin heart EXCOR pediatric VAD interhospital transports of nonambulatory patients with the Ikus stationary driver. *ASAIO journal (American Society for Artificial Internal Organs : 1992 59*, 537–541.

[15] Mehra, M. R., Naka, Y., Uriel, N., Goldstein, D. J., Cleveland, J. C., Colombo, P. C., Walsh, M. N., Milano, C. A., Patel, C. B., Jorde, U. P., Pagani, F. D., Aaronson, K. D., Dean, D. A., McCants, K., Itoh, A., Ewald, G. A., Horstmanshof, D., Long, J. W., and Salerno, C. (2017). A Fully Magnetically Levitated

Circulatory Pump for Advanced Heart Failure. *New England Journal of Medicine 376*, 440–450.

[16] Gülich, J. F., *Kreiselpumpen, Handbuch für Entwicklung, Anlagenplanung und Betrieb*, 4. Auflage; Springer: 2013.

[17] KSB SE & Co KGaA. KSB Centrifugal Pump Lexicon - Back-to-back impeller pump https://www.ksb.com/en-global/centrifugal-pump-lexicon/article/back-to-back-impeller-pump-1118598 (accessed Nov. 24, 2023).

[18] Kapadia, J., Pierce, K., Poupore, A., and Throckmorton, A. (2010). Hydraulic testing of intravascular axial flow blood pump designs with a protective cage of filaments for mechanical cavopulmonary assist. *ASAIO journal (American Society for Artificial Internal Organs : 1992) 56,1*, DOI: 10.1097/MAT.0b013e3181c5b046.

[19] Throckmorton, AL and Kapadia, JY and Chopski, SG, et al. (2011). Numerical, hydraulic, and hemolytic evaluation of an intravascular axial flow blood pump to mechanically support Fontan patients. *Annals of biomedical engineering 39,1*, DOI: 10.1007/s10439-010-0159-3.

[20] Smith, P. A., Wang, Y., Groß-Hardt, S., and Graefe, R., Chapter 10: Hydraulic design In *Mechanical Circulatory and Respiratory Support*, Gregory, S. D., Stevens, M. C., and Fraser, J. F., Eds.; Academic Press: 2018, pp 301–334.

[21] Mulinti, P., Brooks, J., Lervick, B., Pullan, J., and Brooks, A., 10 - Strategies to improve the hemocompatibility of biodegradable biomaterials In *Hemocompatibility of Biomaterials for Clinical Applications*, Siedlecki, C. A., Ed.; Woodhead Publishing: 2018, pp 253–278.

[22] Mathew, J., Sankar, P., and Varacallo, M., *Physiology, Blood Plasma.* Treasure Island (FL): StatPearls Publishing: 2023.

[23] Xu, L., Bauer, J., and Siedlecki, C. (2014). Proteins, platelets, and blood coagulation at biomaterial interfaces. *Colloids and surfaces. 124*, 49–68.

[24] Chaudhry, R., Usama, S., and Babiker, H., *Physiology, Coagulation Pathways.* Treasure Island (FL): StatPearls Publishing: 2022.

[25] LaPelusa, A., and Dave, H., *Physiology, Hemostasis.* Treasure Island (FL): StatPearls Publishing: 2023.

[26] Najjar, S., Slaughter, M., Pagani, F., Starling, R., McGee, E., Eckman, P., Tatooles, A., Moazami, N., Kormos, R., Hathaway, D., Najarian, K., Bhat, G., Aaronson, K., and Boyce, S. (2013). An Analysis of Pump Thrombus Events in Patients in the HeartWare ADVANCE Bridge to Transplant and Continued Access Protocol Trial. *The Journal of Heart and Lung Transplantation 33*, DOI: 10.1016/j.healun.2013.12.001.

[27] Kushner, A., West, W., Khan Suheb, M., and Pillarisetty, L., *Virchow Triad.* Treasure Island (FL): StatPearls Publishing.: 2022.

[28] Ogawa, S., Richardson, J., Sakai, T., Ide, M., and Tanaka, K. (2012). High mortality associated with intracardiac and intrapulmonary thromboses after cardiopulmonary bypass. *J Anesth. 26(1)*, DOI: 10.1007/s00540-011-1253-x.

[29] Fraser, K. H., Zhang, T., Taskin, M. E., Griffith, B. P., and Wu, Z. J. (2010). Computational fluid dynamics analysis of thrombosis potential in left ventricular assist device drainage cannulae. *ASAIO journal (American Society for Artificial Internal Organs : 1992) 56(3)*, DOI: 10.1097/MAT.0b013e3181d861f1.

[30] Cortes, G., Moore, M., and El-Nakeep, S., *Physiology, Von Willebrand Factor.* Treasure Island (FL): StatPearls Publishing: 2023.

[31] Williams, O., and Sergent, S., *Histology, Platelets.* Treasure Island (FL): StatPearls Publishing: 2022.

[32] Shadden, S., and Hendabadi, S. (2013). Potential fluid mechanic pathways of platelet activation. *Biomechanics and modeling in mechanobiology 12(3)*, DOI: 10.1007/s10237-012-0417-4.

[33] Hellums, J. (1994). 1993 Whitaker lecture: Biorheology in thrombosis research. *Annals of biomedical engineering 22(5)*, DOI: 10.1007/BF02367081.

[34] Barbalato, L., and Pillarisetty, L., *Histology, Red Blood Cell.* Treasure Island (FL): StatPearls Publishing: 2022.

[35] Köhne, I. (2020). Haemolysis induced by mechanical circulatory support devices: unsolved problems. *Perfusion 35*, 026765912093130.

[36] Leverett, L., Hellums, J., Alfrey, C., and Lynch, E. (1972). Red blood cell damage by shear stress. *Biophys J. 12(3)*, 257–273.

[37] Graefe, R., Henseler, A., and Steinseifer, U. (2016). Multivariate Assessment of the Effect of Pump Design and Pump Gap Design Parameters on Blood Trauma. *Artificial Organs 40*, 568–576.

[38] Beissinger, R. L., and Laugel, J.-F. (1987). Low-stress hemolysis in laminar blood flow: Bulk and surface effects in capillaries. *AIChE Journal 33*, 99–108.

[39] Garon, A., and Farinas, M.-I. (2004). Fast Three-dimensional Numerical Hemolysis Approximation. *Artificial organs 28*, 1016–25.

[40] Heuser, G., and Opitz, R. (1980). A Couette Viscometer for Short Time Shearing of Blood. *Biorheology 17*, 17–24.

[41] Giersiepen, M., Wurzinger, L. J., Opitz, R., and Reul, H. (1990). Estimation of shear-related blood damage in heart valve prostheses: in vitro comparison of 25 aortic valves. *Artificial Organs 13*, 300–06.

[42] Klaus, S., Paul, R., Reul, H., Mottaghy, K., and Glasmacher, B. (2001). Investigation of flow and material induced hemolysis with a Couette type high shear system. *Materialwissenschaft Und Werkstofftechnik - MATERIALWISS WERKSTOFFTECH 32*, 922–925.

[43] ASTM Standard F1841-19 (2019). Standard Practice for Assessment of Hemolysis in Continuous Flow Blood Pumps. *ASTM International*, DOI: 10.1520/F1841-19..

[44] Billett, H.H., Clinical Methods: The History, Physical, and Laboratory Examinations. In *Hemoglobin and Hematocrit*, Walker, H.K., Hall, W.D. and Hurst, J.W., Ed.; Boston: Butterworths: 1990; Chapter 151.

[45] Alemu, Y., and Bluestein, D. (2007). Flow-induced Platelet Activation and Damage Accumulation in a Mechanical Heart Valve: Numerical Studies. *Artificial organs 31*, 677–88.

[46] Stepanoff, A. J., *centrifugal and axial flow pumps : theory, design, and application*, 2nd edition; KRIEGER PUBLISHING COMPANY: 1957.

[47] Matsuda, H., *Rotary Blood Pumps: New Developments and Current Applications*; Springer: 2000.

[48] Cordier, O., *Ähnlichkeitsbedingungen für Strömungsmaschinen*; BWK Band 5, Nr. 10: 1953.

[49] Fister, W., *Fluidenergiemaschinen*, Band 1: Physikalische Voraussetzungen, Kenngrößen, Elementarstufen der Strömungs- und Verdrängermaschinen.; Springer: 1984.

[50] Foster, G., Chapter 5 - Third-generation ventricular assist devices In *Mechanical Circulatory and Respiratory Support*, Gregory, S. D., Stevens, M. C., and Fraser, J. F., Eds.; Academic Press: 2018, pp 151–186.

[51] Czichos, H., and Habig, K.-H., *Tribologie-Handbuch, Tribometrie, Tribomaterialien, Tribotechnik*, 5th edition; Springer Vieweg Wiesbaden: 2020.

[52] Bender, B., and Dietmar, G., *Dubbel Taschenbuch für den Maschinenbau 2: Anwendungen*, 26th edition; Springer Vieweg Berlin, Heidelberg: 2020.

[53] Boehning, F., Timms, D., Hsu, P.-L., Schmitz-Rode, T., and Steinseifer, U. (2013). Experimental and Analytical Performance Evaluation of Short Circular Hydrodynamic Journal Bearings Used in Rotary Blood Pumps. *Artificial organs 37*, DOI: 10.1111/aor.12076.

[54] Kataoka, H., Kimura, Y., Fujita, H., and Takatani, S. (2006). Influence of Radial Clearance and Rotor Motion to Hemolysis in a Journal Bearing of a Centrifugal Blood Pump. *Artificial organs 30*, 841–54.

[55] Ferziger, J. H., and Peric, M., *Computational Methods for Fluid Dynamics*; Springer Berlin, Heidelberg: 2012.

[56] Simcenter STAR-CCM+ Documentation. Mesh Construction https://docs.sw.siemens.com/documentation/external/PL20201109101148301/en-US/userManual/userguide/html/index.html#page/STARCCMP%2FGUID-DF7340FC-15A4-448F-95B8-D3279D4FB74D.html%23 (accessed Sept. 21, 2023).

[57] Fraser, K. H., Taskin, M. E., Griffith, B. P., and Wu, Z. J. (2011). The use of computational fluid dynamics in the development of ventricular assist devices. *Medical engineering & physics 33(3)*, DOI: 10.1016/j.medengphy.2010.10.014.

[58] Bianchi, G., Rane, S., Kovacevic, A., and Cipollone, R. (2017). Deforming grid generation for numerical simulations of fluid dynamics in sliding vane rotary machines. *Advances in Engineering Software 112*, DOI: 10.1016/j.advengsoft.2017.05.010.

[59] Celik, I., Ghia, U., Roache, P., Freitas, C., Coloman, H., and Raad, P. (2008). Procedure of Estimation and Reporting of Uncertainty Due to Discretization in CFD Applications. *J. Fluids Eng. 130*, DOI: 10.1115/1.2960953.

[60] Schwer, L. E. (2008). IS YOUR MESH REFINED ENOUGH ? Estimating Discretization Error using GCI.

[61] Roache, P. J. (1994). Perspective: A Method for Uniform Reporting of Grid Refinement Studies. *J. Fluids Eng. 116(3)*, 9.

[62] Taskin, M., Fraser, K., Zhang, T., Wu, C., Griffith, B., and Wu, Z. (2012). Evaluation of Eulerian and Lagrangian Models for Hemolysis Estimation. *ASAIO journal (American Society for Artificial Internal Organs : 1992) 58*, 363–72.

[63] COMSOL Navier-Stokes Equations https://www.comsol.com/multiphysics/navier-stokes-equations%20parent=modeling-conservation-mass-energy-momentum-0402-432-302 (accessed Nov. 27, 2023).

[64] Pivkin, I., Richardson, P., and Karniadakis, G. (2006). Blood flow velocity effects and role of activation delay time on growth and form of platelet thrombi. *Proceedings of the National Academy of Sciences of the United States of America 103*, DOI: 10.1073/pnas.0608546103.

[65] Throckmorton, A., Kapadia, J., Chopski, S., Bhavsar, S., Moskowitz, W., Gullquist, S., Gangemi, J., Haggerty, C., and Yoganathan, A. (2011). Numerical, Hydraulic, and Hemolytic Evaluation of an Intravascular Axial Flow Blood Pump to Mechanically Support Fontan Patients. *Annals of biomedical engineering 39*, 324–36.

[66] Carolus, T., *Ventilatoren: Aerodynamischer Entwurf – Konstruktive Lärmminderung – Optimierung*; Springer Vieweg Wiesbaden: 2020.

[67] Al-Azawy, M., Turan, A., and Revell, A. (2016). Investigating the impact of non-Newtonian blood models within a heart pump. *International journal for numerical methods in biomedical engineering 33*, DOI: 10.1002/cnm.2780.

[68] Simcenter STAR-CCM+ Documentation. Generalized Newtonian Fluids https://docs.sw.siemens.com/documentation/external/PL20201109101148301/en-US/userManual/userguide/html/index.html#page/STARCCMP%2FGUID-41D73864-09C1-4A27-AB15-15DF4E6BAF21.html%23wwID0EW6FAD (accessed Dec. 4, 2023).

[69] Simcenter STAR-CCM+ Documentation. Velocity Gradient and Invariants https://docs.sw.siemens.com/documentation/external/PL20201109101148301/en-US/userManual/userguide/html/index.html#page/STARCCMP%2FGUID-69CBCF59-4883-4B29-973C-9041D28EA654.html (accessed Feb. 6, 2024).

[70] Simcenter STAR-CCM+ Documentation. K-Omega Turbulence https://docs.sw.siemens.com/documentation/external/PL20201109101148301/en-US/userManual/userguide/html/index.html#page/STARCCMP%2FGUID-14F1432B-B915-42FE-9862-71D1B53BEA6B.html (accessed Dec. 5, 2023).

[71] Escher, A., Hubmann, E. J., Karner, B., Messner, B., Laufer, G., Kertzscher, U., Zimpfer, D., and Granegger, M. (2022). Linking Hydraulic Properties to Hemolytic Performance of Rotodynamic Blood Pumps. *Advanced Theory and Simulations 5*, 2200117.

[72] Granegger, M., Thamsen, B., Schlöglhofer, T., Lach, S., Escher, A., Haas, T., Meboldt, M., Schweiger, M., Hübler, M., and Zimpfer, D. (2020). Blood trauma potential of the HeartWare Ventricular Assist Device in pediatric patients. *The Journal of Thoracic and Cardiovascular Surgery 159*, 1519–1527.e1.

[73] Fatullayev, J., Samak, M., Sabashnikov, A., Zeriouh, M., Rahmanian, P. B., Choi, Y. H., Schmack, B., Kallenbach, K., Ruhparwar, A., Eghbalzadeh, K., Dohmen, P. M., Karck, M., Wippermann, J., Wahlers, T., Popov, A. F., Simon, A. R., and Weymann, A. (2015). Continuous-Flow Left Ventricular Assist Device Thrombosis: A Danger Foreseen is a Danger Avoided. *Medical science monitor basic research 21*, 141–144.

Appendix A

Berechnungsprogramm für Rotationsblutpumpen

INSTITUT FÜR
ENERGIETECHNIK
UND THERMODYNAMIK
Institute of Energy Systems and Thermodynamics

Projektarbeit

Berechnungsprogramm für Rotationsblutpumpen

unter der Leitung von

Marcus Granegger, PhD
Assistant Prof. Dipl.-Ing. Bernhard Semlitsch
E302 - Institut für Energietechnik und Thermodynamik

von

Stefan Maric, BSc
Matr.Nr. 01431093

Inhaltsverzeichnis

1 Einleitung **2**
1.1 Motivation 2
1.2 Ziel der Arbeit 4
1.3 Theorie 5
1.3.1 Cordier- Diagramm 8
1.3.2 Strömung im Laufrad 9
1.3.3 Auswahl der Leitvorrichtung 12

2 Methoden **17**
2.1 Pumpenentwurf 18
2.2 Pumpenvergleich 18
2.3 Entwurf des Spiralgehäuses 19
2.4 Überprüfung nach Cordier 19

3 Resultate **21**
3.1 Ergebnisse 21
3.2 Diskussion 26

Literatur **28**

Kapitel 1

Einleitung

1.1 Motivation

Weltweit leiden Millionen von Menschen an einer Herzinsuffizienz [15]. Dabei kann das Herz das benötigte Herzminutenvolumen (HMV), also den Volumenstrom des Blutes pro Minute, nicht mehr bereitstellen [10]. Die 5-Jahres Überlebenschance, ab diagnostizierter Herzinsuffizienz, liegt statistisch gesehen bei 57% und die 10-Jahres Überlebenschance bei nur 35% [20]. Schreitet die Herzinsuffizienz, während der medikamentösen Behandlung, weiter fort, werden operative oder palliative Therapien angewendet [30].

Ein bewährter operativer Eingriff zur Behandlung von Herzinsuffizienz ist die Herztransplantation [30]. Die Tatsache, dass der Bedarf an Organen größer als das Angebot ist und die gründliche Prüfung der Eignung der Patienten eine dementsprechende Wartezeit erfordert, erschweren jedoch die schnellstmögliche Behandlung dieser Patienten [7]. Zur Überbrückung dieser Zeiträume, oder als Destination-Therapie, werden in der Regel mechanische Kreislaufunterstützungssysteme, wie z. B. ventrikuläre Unterstützungssysteme, eingesetzt, um den Blutkreislauf des Patienten aufrecht zu erhalten [23, 26]. Hauptsächlich werden implantierbare Rotationsblutpumpen (RBP) als ventrikuläre Unterstützungssysteme, wie z.B. das Heart Mate 3 (siehe Abbildung 1.1), eingesetzt. RBP werden nach dem Prinzip der Kreiselpumpen entworfen, welche jedoch aufgrund der hohen Drehgeschwindigkeiten und der nicht-physiologischen Geometrie der Systeme ein besonderes Augenmerk auf die Hämokompatibilität erfordern. Das rotierende Laufrad der Pumpe erzeugt Scherbelastungen auf das geförderte Blut, welche bei nicht-physiologischer Höhe oder Dauer zu Blutschädigung führen können [27].

Unter Blutschädigung versteht man die Hämolyse (mechanische Zerstörung der roten Blutkörperchen), verminderte Funktion der weißen Blutkörperchen, Aktivierung der Blutplättchen und Veränderung der Gerinnungskaskade. Letzteres kann zu Thrombusbildung (Blutgerinnsel) und -embolien führen [14]. Thromboembolien sind Verstopfungen von Blutgefäßen, welche durch den Transport von Blutgerinnseln entstehen [11]. Solche Blutgerinnsel können, durch den Kontakt des Blutes mit dem körperfremden Material der Blutpumpe, in Zonen niedriger Geschwindigkeit entstehen [24].

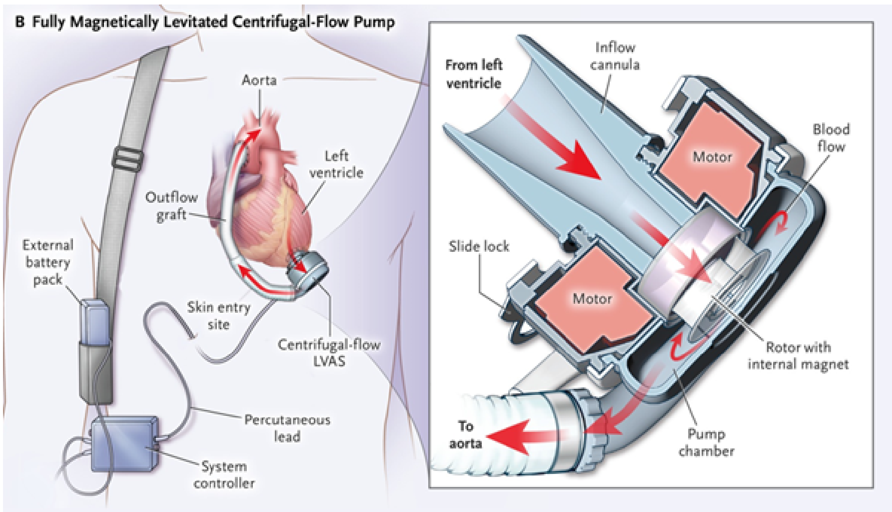

Abbildung 1.1: Darstellung einer implantierten Rotationsblutpumpe und Schnittdarstellung des Heart Mate 3, in Anlehnung an Mehra et al. [22]

Aufgrund der nicht-physiologischen Geometrie der Pumpen kann es zu Stagnationszonen kommen. Dies kann in Kombination mit den beschädigten Blutbestandteilen und durch den Kontakt mit dem künstlichen Material der Pumpe zu Thrombusbildung führen [2, 9, 27].

Speziell in der Pädiatrie fehlt es an implantierbaren Unterstützungssystemen für den Kreislauf, welche als zuverlässige Überbrückungslösung bis zur Transplantation verwendet werden können. Denn auch in Neugeborenen und Kleinkindern werden Herzinsuffizienzen diagnostiziert, welche sich in den meisten Fällen aus angeborenen Herzkrankheiten oder Kardiomyopathien entwickeln [13]. Allein in den USA sind im Durchschnitt über 500 pädiatrische Patienten (< 18 Jahre) pro Jahr auf der Warteliste für eine Herztransplantation gelistet [1].

Derzeit sind zur Behandlung pädiatrischer Fälle nur parakorporale Systeme, wie z.B. das Berlin Heart EXCOR, zugelassen. Als parakorporal beschreibt man ein System, in welchem sich die Blutpumpe außerhalb des Körpers befindet und mittels Kanülen und Schläuchen an das Herz und die Gefäße angeschlossen ist [18]. Jedoch liegt die Sterberate der Patienten mit einem Gewicht unter 10 kg, welche mit diesem System versorgt wurden, bei 38% [4]. Außerdem ist mit diesem System ein stationärer Krankenhausaufenthalt verbunden, da die mobile Einheit des Berlin Heart EXCOR erst bei größeren Pumpengrößen verwendet werden kann [32].
Die Konzeptionierung einer implantierbaren Rotationsblutpumpe für Säuglinge und Kleinkinder wird besonders aufgrund des kleinen Herzvolumens erschwert. Hierbei stehen neben den kleinen geometrischen Dimensionen, das geringe Herzzeitvolumen und die Hämokompatibilität im Fokus. Die technische Bewältigung dieser Herausforderungen ist von entscheidender Bedeutung, um den ungedeckten medizinischen Bedarf an implantierbaren Rotationsblutpumpen für den Einsatz in der Pädiatrie zu erfüllen [13].

1.2 Ziel der Arbeit

Diese Projektarbeit behandelt die Auslegung von Rotationsblutpumpen, basierend auf dem Prinzip der Kreiselpumpen, als linksventrikuläres Unterstützungssystem. Das Ziel ist es ein Berechnungsprogramm zu erstellen, welches unter Berücksichtigung der Funktionalität und der Effizienz die Auswahl der Auslegungsparameter ermöglicht. Die Entwicklung von Rotationsblutpumpen ist generell ein iterativer Prozess, bei dem zu Beginn Designparameter wie Volumenstrom, Wirkungsgrad und Laufradgeometrie angenommen werden müssen. Weiters folgt eine numerische Simulation, um die Funktion des Konzeptes zu überprüfen. Basierend auf der Analyse der Simulationsergebnisse werden die eingangs gewählten Parameter angepasst und es folgen weitere Simulation bis die Pumpe optimal ausgelegt ist. Die numerischen Simulationen sind jedoch Teil der anschließenden Masterarbeit und werde in Folge nicht näher beschrieben. Das in dieser Arbeit zu entwickelnde Berechnungsprogramm soll als Hilfe zum Entwurf von Rotationsblutpumpen, unabhängig von ihrer Größe und dem Einsatzbereich, dienen. Dieses Tool hat das Ziel, den Optimierungsprozess bei der Konzeptionierung von RBP zu vereinfachen und zu beschleunigen. Aus diesem Grund soll das Berechnungsprogramm neben einer Zeitersparnis, eine visuelle Hilfe, sowie die direkte Vergleichbarkeit unterschiedlicher

Parameter bieten. Speziell die Vergleichbarkeit spielt eine übergeordnete Rolle, da das Ziel der anschließenden Masterarbeit der Vergleich einer einstufigen Blutpumpe mit einem neuartigen Konzept einer zweistufigen Blutpumpe, für pädiatrische Patienten, ist.

1.3 Theorie

Rotationsblutpumpen haben die Aufgabe, einen spezifischen Volumenstrom Q an Blut zu fördern und eine spezifische Druckerhöhung H zu erreichen. Aktuell werden zur Laufrad- und Leitapparatauslegung von Rotationsblutpumpen die theoretischen Grundlagen von Kreiselpumpen zugrunde gelegt. Dieser Berechnung der Pumpengeometrie folgt ein iterativer Prozess, welcher zum Beispiel basierend auf der Analyse der Ergebnisse von Simulationen der numerischen Strömungsmechanik (CFD) die Auslegungsparameter anpasst. In diesen Simulationen werden die hydraulische Leistung der Pumpe sowie zusätzliche Parameter wie Scherspannungen und Geschwindigkeitsverteilungen betrachtet, welche Auskunft über die Belastung der Blutbestandteile und mögliche Stagnationsbereiche geben [21, 27, 29].
Der Pumpvorgang wird generell durch den Volumenstrom Q, die Druckerhöhung H und die Drehzahl n charakterisiert. Diese Parameter werden zur Auswahl der Laufradform und der Bauart der Pumpe verwendet. Die gängigen Laufradformen radial, halbaxial und axial sind in Abbildung 1.2 dargestellt [17]. Der spezifische Volumenstrom Q und die dabei zu erzielende Druckerhöhung H ergibt sich für Blutpumpen aus der individuellen Physiologie des Herz-Kreislaufsystems und kann sich von Patient zu Patient unterscheiden. Im Durchschnitt fördert das Herz eines gesunden Erwachsenen 6 - 8 Liter Blut pro Minute [31]. Bei Säuglingen steigt das Herzminutenvolumen mit dem Heranwachsen und wird in diesem Fall pro kg Gewicht angegeben. Studien zufolge liegt der Wert für das HMV pro Gewichtseinheit bei ca. 231 ml/kg*min [19]. Betrachtet man beispielsweise ein 4-Monate junges Kind, welches laut WHO ein gemitteltes Gewicht von 6,4 kg aufweist, besitzt dieses ein HMV von ca. 1,5 l/min [12]. Ähnliche Forschungsarbeiten zu pädiatrischen RBP streben bei einem Volumenfluss von 1,5 l/min eine Druckerhöhung von 100 mmHg an [33].

Um eine ausreichende Auswaschung und die Verhinderung von Thrombenbildung in Rotationsblutpumpen zu gewährleisten, werden die Spalten zwischen dem rotie-

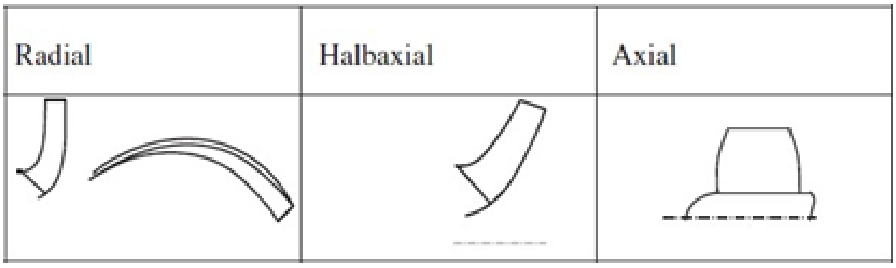

Abbildung 1.2: Laufradformen von Kreiselpumpen [17]

renden Laufrad und dem stationären Pumpengehäuse größer als bei industriellen Pumpen dimensioniert [16]. Aufgrund den dadurch auftretenden Rückströmungen vom Austritt zum Eintritt, kommt es zu Spaltströmen Qsp, welche damit zu einem Leistungsverlust beitragen. Das Laufrad muss somit den Volumenstrom

$$Q_{La} = Q + Q_{sp} \tag{1.1}$$

fördern, um den spezifischen Volumenstroms Q am Austritt der Pumpe sicherzustellen [17]. In Abbildung 1.3 wird eine Schnittdarstellung einer herkömmliche Spiralgehäusepumpe dargestellt. Die Detailansicht Z zeigt den Meridianschnitt des Laufrades mit den wichtigsten Bezeichnungen. Parameter am Eintritt des Laufrades (Saugkante) werden mit „1“ und Parameter am Austritt des Laufrades (Druckkante) mit „2“ notiert. Der Parameter d2 bezeichnet hier den Durchmesser des Laufradaustritts. Bei Schrägstellung des Laufradeintritts, wird als Durchmesser d_1 der Durchmesser d_{1b}

$$d_{1b} = \frac{d_{1a} + d_{1i}}{2} \tag{1.2}$$

verwendet. d_{1a} und d_{1i} bezeichnen den äußeren und inneren Durchmesser am Eintritt des Laufrades [17].

Um Pumpen möglichst effizient zu entwerfen, wurde die spezifische Drehzahl n_q

$$n_q = \frac{n}{(H/z_{st})^{0.75}} \tag{1.3}$$

eingeführt, welche eine Beziehung zwischen den charakteristischen Parametern eines Pumpvorgangs darstellt. Diese Kennzahl beschreibt das Verhältnis von Drehzahl n

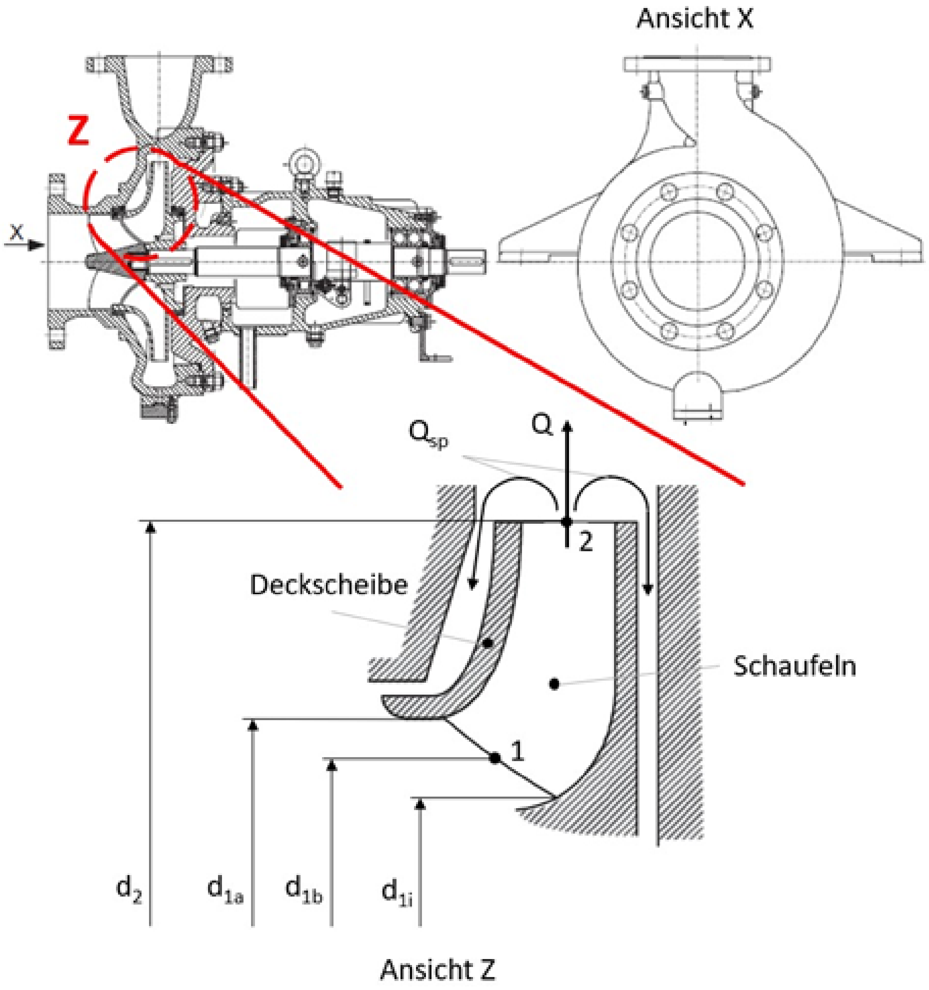

Abbildung 1.3: Schnittdarstellung einer einstufigen Radialpumpe mit Spiralgehäuse, in Anlehnung an Gülich et al., 2014, S 44, 116. [17]

(U/min), Volumenstrom Q (m^3/s) und Druckerhöhung H (m). Zur Betrachtung von mehrstufigen Pumpen wurde zusätzlich die Stufenanzahl z_{St} eingeführt. Die spezifische Drehzahl gibt Auskunft über die zu verwendende Laufradform für ein effizientes Pumpenkonzept. In einem Bereich von $n_q = 7 - 100$ sind Radialpumpen, $n_q = 35 - 160$ Halbaxialpumpen und $n_q > 160$ Axialpumpen nach Cordier (siehe folgender Abschnitt) am effizientesten. Der Wirkungsgrad der gesamten Pumpe hängt nicht allein von der Laufradform ab, sondern auch von der Gesamtkonstruktion und der absoluten Pumpengröße. Die hydraulischen Verluste in der Pumpe, sind zu Beginn nur schätzbar oder numerisch lösbar. Somit weicht die tatsächlich von der Pumpe erzeugte Druckerhöhung substanziell von der theoretisch verlustfreien

Druckerhöhung ab. Besitzen unterschiedliche Pumpen dieselbe spezifische Drehzahl, werden sie als geometrisch ähnliche Pumpen bezeichnet [17, 25]. Da in der anschließenden Masterarbeit eine Pumpe entworfen werden soll, welche eine Vergleichbarkeit zu einem zweistufigen Konzept aufweist, wird das Tool so entworfen, dass es die Möglichkeit bietet geometrisch ähnliche Pumpen zu konzipieren.

1.3.1 Cordier- Diagramm

Um eine Pumpe mit maximaler Effizienz auszulegen, wird das Cordier- Diagramm herangezogen (siehe Abbildung 1.4). Otto Cordier betrachtete insgesamt 120 Strömungsmaschinen im Betriebsbereich des höchsten Wirkungsgrades. In diesen Experimenten wurde für jede Strömungsmaschine in ihrem effizientesten Betriebspunkt, die Laufzahl

$$\sigma = n * \frac{\sqrt{Q}}{(2 * \Delta H_s)^{0.75}} * 2 * \sqrt{\pi} \tag{1.4}$$

und die Durchmesserzahl

$$\delta = d_2 * \frac{(2 * \Delta H_s)^{0.25}}{\sqrt{Q}} * \frac{\sqrt{\pi}}{2} \tag{1.5}$$

berechnet. In diesen Gleichungen wird die isentrope Enthalpiedifferenz $\Delta \mathrm{H}_s$ zwischen Ein- und Austritt der Pumpe und der Laufradaußendurchmesser d_2 verwendet. Die berechneten Werte der jeweiligen Maschinen wurden in einem gemeinsamen Diagramm festgehalten, welches auf der Abszisse die Durchmesserzahl und auf der Ordinate die Laufzahl anzeigt. Später wurde die spezifische Drehzahl n_q anstelle der Laufzahl σ verwendet [5, 25]. Als Weiterentwicklung wurde die Durchmesserzahl δ mit dem spezifischen Durchmesser D_q

$$D_q = d_2 * \frac{(H/z_{st})^{0.25}}{\sqrt{Q}} \tag{1.6}$$

ersetzt. Weiters wurde der Betriebsbereich besten Wirkungsgrades als ein bandförmiger Bereich in einem neuen Diagramm dargestellt (siehe Abbildung 1.5) [8].

Nach Auswahl der Pumpenparameter Q, H und n wird die spezifische Drehzahl

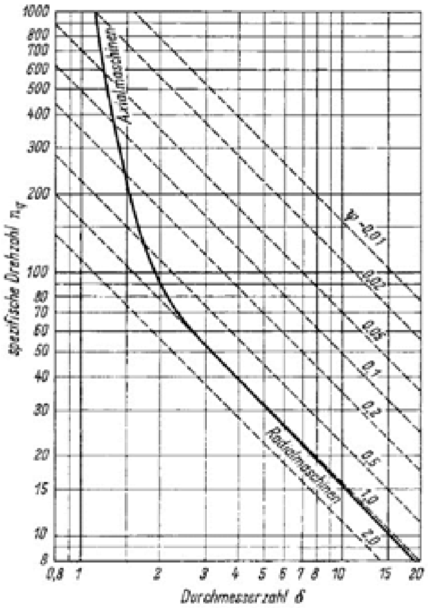

Abbildung 1.4: Cordier- Diagramm in Abhängigkeit der spezifischen Drehzahl und der Durchmesserzahl [25].

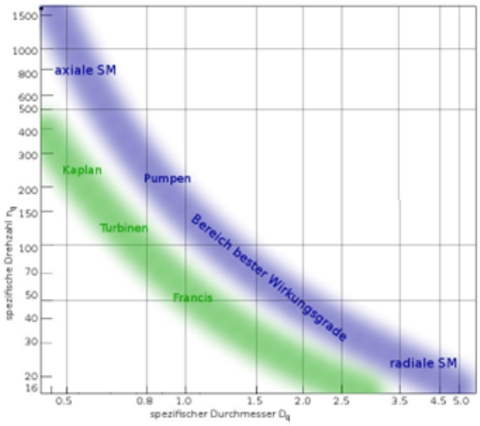

Abbildung 1.5: Weiterentwicklung des Cordier- Diagramms mit dem spezifischen Durchmesser [8].

n_q berechnet und in das Cordier- Diagramm eingetragen. Daraus ergibt sich eine beschränkte Auswahl an spezifischen Durchmessern D_q, welche in Kombination mit der spezifischen Drehzahl eine Laufradkonfiguration besten Wirkungsgrades versprechen. Umgekehrt kann durch Wahl des äußeren Durchmessers d_2 ein D_q ermittelt werden. Dieses wird verwendet, um aus dem Diagramm ein n_q abzulesen und somit eine Drehzahl für eine effiziente Konfiguration zu ermitteln. In Abbildung 1.5 wird ersichtlich, dass einerseits die axialen Strömungsmaschinen hohe spezifische Drehzahlen und niedrige spezifische Durchmesser aufweisen, andererseits haben die radialen Strömungsmaschinen niedrige spezifische Drehzahlen und hohe spezifische Durchmesser. In dem Bereich von n_q zwischen 40 bis 160 befinden sich die halbaxialen Laufräder [17].

1.3.2 Strömung im Laufrad

Die Strömung in Strömungsmaschinen wird in einem absoluten und einem relativen System beschrieben. Die Umfangsgeschwindigkeiten des Pumpenlaufrades, die Absolut- sowie Relativgeschwindigkeiten der Strömung können geometrisch in einem Geschwindigkeitsdreieck (siehe Abbildung 1.7) abgebildet werden. Um die vorherrschenden Geschwindigkeiten im Laufrad zu beschreiben, wird zunächst über die Drehzahl und die geometrischen Abmessungen des Pumpenlaufrades die Umfangsgeschwindigkeiten $u_{1,2}$

$$u_{1,2} = d_{1,2} * \pi * n \tag{1.7}$$

berechnet. Weiters werden die meridianen Absolutgeschwindigkeiten $c_{m,1,2}$

$$c_{m,1,2} = \frac{Q_{La}}{A_{1,2}} \tag{1.8}$$

aus dem vom Laufrad geförderten Volumenstrom Q_{La} und der Querschnittsfläche $A_{1,2}$, welche senkrecht zur Flussrichtung betrachtet wird, berechnet. Wie vorab beschrieben ist Q_{La} größer als der global geförderte Volumenstrom Q, da ein Teil des Fluides über die vorhandenen Spalten in den Einlass zurückfließt. Am Laufradeintritt und -austritt bewirken die Laufschaufeln, aufgrund ihrer endlichen Dicke, eine Versperrung des durchströmten Querschnittes. Somit wird $A_{1,2}$

$$A_{1,2} = (d_{1,2} * \pi - z_{Bl} * \frac{e_{1,2}}{sin(\beta_{1,2,B})}) * h_{1,2} \tag{1.9}$$

abzüglich der projizierten Fläche der Laufschaufeln betrachtet, wobei z_{Bl} die Anzahl der Laufschaufeln, $e_{1,2}$ die Dicke der Laufschaufeln, $\beta_{1,2,B}$ den Laufschaufelwinkel und $h_{1,2}$ die Höhe der Laufschaufeln beschreibt. Abbildung 1.6 zeigt die schematische Darstellung der projizierten Laufschaufeldicke am Laufradeintritt [17].

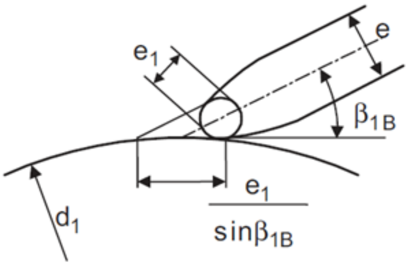

Abbildung 1.6: Einfluss der Laufschaufeldicke auf den Querschnitt des Laufschaufelkanals [17].

Für die Konzeptionierung eines Pumpenlaufrades wird angenommen, dass für den Auslegungspunkt die Strömungswinkel $\beta_{1,2}$ den Laufschaufelwinkeln $\beta_{1,2,B}$ entsprechen und die Anströmung drallfrei ($\alpha_1 = 90°$) erfolgt. Der Winkel $\beta_{1,B}$ wird spezifisch für jedes Pumpenkonzept berechnet, um eine drallfreie Anströmung zu gewährleisten. In Kombination mit dem gewählten Laufschaufelwinkel $\beta_{2,B}$ lassen sich, durch geometrische Beziehungen in den Geschwindigkeitsdreiecken (siehe Abbildung 1.7), die Anteile der Relativgeschwindigkeiten in Umfangsrichtung $\mathrm{w}_{u,1,2}$

$$w_{u,1,2} = \frac{c_{m,1,2}}{tan(\beta_{1,2})} \tag{1.10}$$

ermitteln.

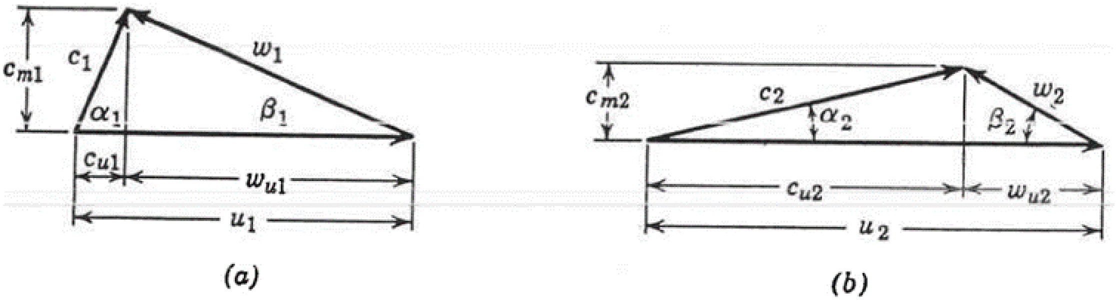

Abbildung 1.7: Geschwindigkeitsdreiecke für Laufradeintritt (a) und Laufradaustritt (b) [28].

Aus der Differenz der Umfangsgeschwindigkeiten und dem Anteil der Relativgeschwindigkeiten in Umfangsrichtung ergibt sich der Anteil der Absolutgeschwindigkeiten in Umfangsrichtung $\mathrm{c}_{u,1,2}$

$$c_{u,1,2} = u_{1,2} - w_{u,1,2} \tag{1.11}$$

Somit lassen sich, durch Anwendung des Satz des Pythagoras, die Absolutgeschwindigkeit $\mathrm{c}_{1,2}$

$$c_{1,2} = \sqrt{c_{m,1,2}^2 + c_{u,1,2}^2} \tag{1.12}$$

und Relativgeschwindigkeiten $\mathrm{w}_{1,2}$

$$w_{1,2} = \sqrt{c_{m,1,2}^2 + w_{u,1,2}^2} \tag{1.13}$$

berechnen [17].
Die Geschwindigkeitsänderungen von u, w und c am Laufradeintritt und -austritt beschreiben die verlustfreie spezifische Schaufelarbeit Y_{sch}

$$Y_{sch} = H_{th} * g = \frac{1}{2} * (u_2^2 - u_1^2 + w_1^2 - w_2^2 + c_2^2 - c_1^2) \tag{1.14}$$

aus welcher sich die theoretische Druckerhöhung H_{th} ergibt. Formel 1.14 zeigt die Abhängigkeit der Schaufelarbeit vom Zentrifugalanteil u_2^2 - u_1^2, der Verzögerung der Relativgeschwindigkeiten w_1^2 - w_2^2 im Schaufelkanal und der Beschleunigung der Absolutgeschwindigkeit c_2^2 - c_1^2 [25]. Dadurch, dass sich die Höhe der Verzögerung der Relativgeschwindigkeit direkt proportional auf die Druckerhöhung H auswirkt, ist man bestrebt diesen Wert so hoch wie möglich zu halten. Jedoch führt eine zu große Verzögerung im Laufrad zu ungewünschten Ablösungen der Strömung von den Laufschaufeln. Diese Ablösungen führen zu erhöhten hydraulischen Verlusten und zu Stagnationsbereichen [17, 27]. Das de Haller Kriterium beschreibt einen Grenzwert für das Verzögerungsverhältnis der Relativgeschwindigkeit am Laufradaustritt zu Laufradeintritt. Wird dieses Kriterium

$$\frac{w_2}{w_1} > 0.7 \tag{1.15}$$

nicht erfüllt, können Ablösungen der Strömung an den Grenzschichten entstehen [6]. Neuere Versuche ergaben einen Grenzwert von 0,55 – 0,6 [3].

1.3.3 Auswahl der Leitvorrichtung

Nachdem die Strömung das Laufrad verlässt, wird diese über einen Leitapparat bis zu einem Druckstutzen weitergeleitet. Während diesem Leitvorgang wird ein Teil der kinetischen Energie der Strömung möglichst verlustarm in statischen Druck umgewandelt. Die Leitvorrichtung wird basierend auf der Laufradgestaltung entworfen. Im Folgenden wird als Leitapparat das in Abbildung 1.8 ersichtliche Spiralgehäuse betrachtet. Das Spiralgehäuse ist ein gekrümmter Diffusor, welcher an den Umfang des Laufrades anschließt. Die Querschnittsformen von Spiralgehäusen können unterschiedlich ausgeführt werden. Die gängigsten Formen werden in Abbildung 1.9 gezeigt [17].

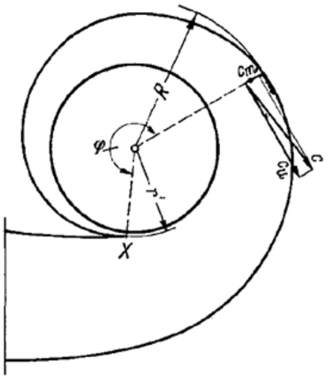

Abbildung 1.8: Prinzipskizze eines Spiralgehäuses mit einer Einfachspiral- Ausführung [25].

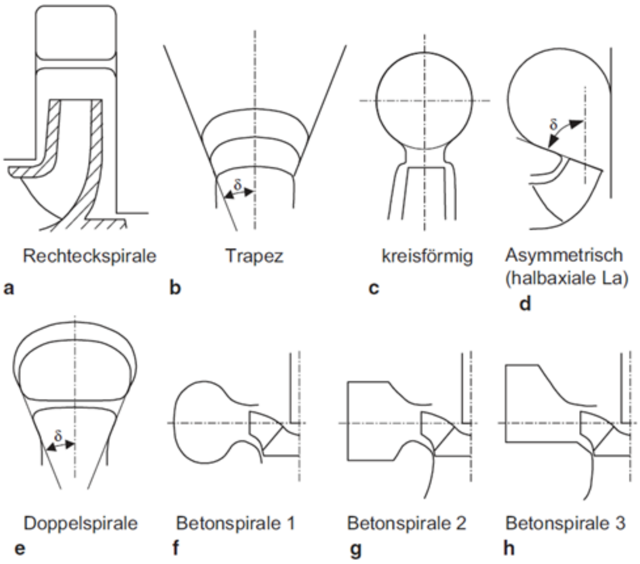

Abbildung 1.9: Gängige Querschnittsformen bei Spiralgehäusen [17].

Zwischen dem Laufrad und der Zunge (Verbindung von Anfangsquerschnitt der Spirale zu Druckstutzen) ist ein Abstand vorgesehen, um zusätzliche Verluste durch Druckpulsationen zu vermeiden. Der Durchmesser d_z, an dem die Zunge zu entwerfen ist, wird mit

$$d_z \geq d_2 * (1.03 + 0.1 * \frac{n_q}{n_{q,Ref}} + 0.07 * \frac{\rho}{\rho_{Ref}} * \frac{H}{H_{Ref}}) \tag{1.16}$$

beschrieben. Die Dichte ρ des Fördermediums fließt in diese Berechnung mit ein. Die Indizes „Ref“ beziehen sich auf Referenzwerte, welche für $n_{q,Ref} = 40$, $\rho_{Ref} = 1000$ kg/m^3 und $H_{Ref} = 1000$ m vorgegeben sind [17].
Bei der Berechnung des Flächenverlaufes des Querschnitts der Spirale betrachtet man zwei unterschiedliche Lösungsansätze:

Drallerhaltung

Der Endquerschnitt des Spiralgehäuses wird hier nach dem Drallsatz und der Drallerhaltung gestaltet. Der Drallsatz beschreibt das Impulsmoment, also den Drall, an einem Ort i innerhalb der Pumpe. Das Impulsmoment

$$M_J = \rho * Q * c_{u,i} * r_i \tag{1.17}$$

steht in Abhängigkeit zur Dichte des Fördermediums ρ, des Volumenstroms Q, der Absolutgeschwindigkeitskomponente in Umfangsrichtung $c_{u,i}$ und des radialen Abstandes r_i zum Betrachtungsort i. Betrachtet man nun zwei Punkte m und n, so besagt die Drallerhaltung

$$\cancel{\rho * Q *} c_{u,m} * r_m = \cancel{\rho * Q *} c_{u,n} * r_n \tag{1.18}$$

Da man in Strömungsmaschinen inkompressible Fluide (ρ=konstant) und einen konstanten Volumenstrom betrachtet, führt dies zu

$$c_{u,i} * r_i = K = konstant \tag{1.19}$$

Das Spiralgehäuses ist so auszulegen, dass der Drall in jedem Punkt i in der Spirale konstant ist. Somit muss jeder Querschnitt der Leitvorrichtung folgende Gleichung

$$\int_{r_z}^{r_A} \frac{b}{r} * dr = \frac{Q * \varphi}{360 * c_{u,2} * r_2} \tag{1.20}$$

erfüllen. Das Flächenintegral wird in Abbildung 1.10 veranschaulicht [17].

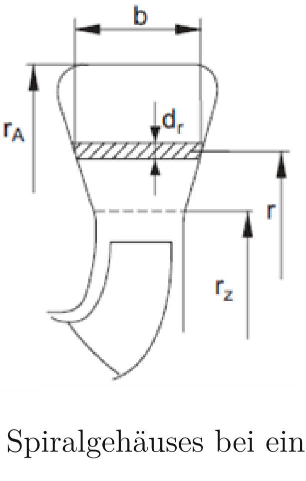

Abbildung 1.10: Schnitt des Spiralgehäuses bei einem beliebigen Winkel ϵ [17].

Geschwindigkeitserhaltung

Bei diesem Lösungsansatz wird das Spiralgehäuse so ausgelegt, dass die mittlere Geschwindigkeit in jedem Querschnitt konstant ist. Dieser Ansatz stützt sich zwar auf theoretische Überlegungen, jedoch wurden die Werte experimentell für den besten Wirkungsgrad ermittelt und in einem Diagramm (siehe Abbildung 1.11) in Abhängigkeit der spezifischen Drehzahl festgehalten. Die mittlere Geschwindigkeit c_3

$$c_3 = K_3 * \sqrt{2 * g * H} \tag{1.21}$$

wird nun mittels dem experimentell ermittelten Wert K_3, der Erdbeschleunigung g und der Druckerhöhung H beschrieben. Da sich diese Methode besonders im amerikanischen Raum etabliert hat, ist hier das amerikanische Einheitensystem zu verwenden [28].

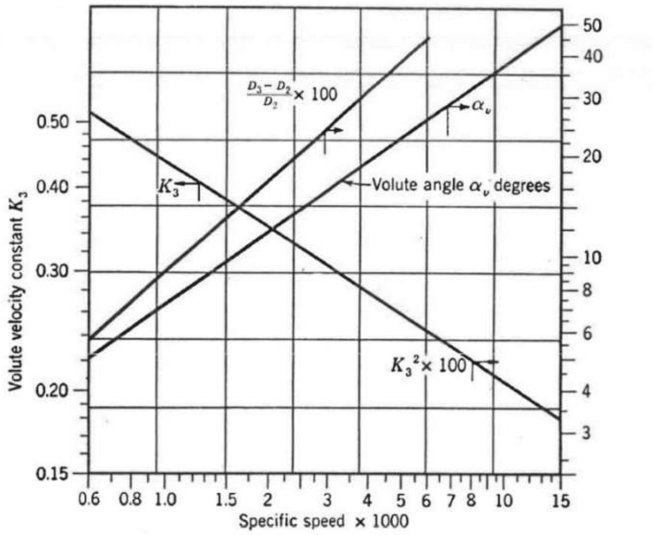

Abbildung 1.11: Experimentell ermittelte Parameter für die Auslegung des Spiralgehäuses nach konstanter mittlerer Geschwindigkeit [28].

Der Endquerschnitt des Spiralgehäuses $A_{Sp,360}$ wird durch die Beziehung zum Volumenstrom

$$A_{Sp,360} = \frac{Q}{c_3} \tag{1.22}$$

beschrieben. Der Querschnitt des Spiralgehäuses

$$A_{Sp,\varphi} = \frac{\varphi}{360} * \frac{Q}{c_3} \tag{1.23}$$

vergrößert sich proportional mit dem Winkel φ (siehe Abbildung 1.8) von der Position der Zunge bis zum Endquerschnitt [28].

Kapitel 2

Methoden

Zur Programmierung des Berechnungstools wurde der MATLAB App Designer von MathWorks verwendet. Für diesen Zweck wurde eine graphische Benutzeroberfläche (siehe Abbildung 3.1) erstellt, welche über ein Eingabefenster und Ausgabefenster verfügt. Weiters werden durch mehrere Reiter weitere Informationen wie die Geschwindigkeitsdreiecke, die Spiralgehäusegeometrie und das Cordier- Diagramm dargestellt.

Die im Rahmen der Projektarbeit betrachteten Konzepte zu Rotationsblutpumpen werden unter besonderer Berücksichtigung der Physiologie des Herz-Kreislaufsystems entwickelt. Um eine effiziente Pumpenkonzeptionierung zu beginnen, muss zunächst ein Betriebspunkt definiert werden. Folglich muss der Volumenfluss Q entsprechend dem HMV eines gesunden Menschen gewählt werden. Die Wahl der Drehzahl n erfolgt zu Beginn entweder auf Basis der Parameter von ähnlichen Rotationsblutpumpen, oder bei einem Pumpenvergleich über die spezifische Drehzahl nq. Näheres wird in den Kapiteln „Pumpenentwurf“ und „Pumpenvergleich“ beschrieben. Da die Blutpumpe letztendlich als Implantat im Thorax am linken Ventrikel eingesetzt wird (siehe Abbildung 1.1), ist man mit dem Bauraum durch die anatomischen Gegebenheiten begrenzt. Aufgrund dessen wird das Pumpenkonzept so klein wie möglich, aber so groß wie notwendig, ausgelegt.

Die Geschwindigkeiten in einer Pumpe werden durch den geförderten Volumenstrom Q_{La}, die Drehzahl n und die Geometrie des Laufrades beschrieben. Der rezirkulierende Förderstrom Q_{Sp}, welcher abhängig von der Pumpengeometrie und dem Betriebspunkt ist, wird als ein Bruchteil (ca. 20-25%) des Volumenstroms Q angenommen und kann iterativ angepasst werden. Da sich die Geometrie aus mehreren

Parametern, wie den Laufraddurchmessern $d_{1,2}$, der Anzahl der Laufschaufeln z_{Bl}, der Höhe $h_{1,2}$, Dicke $e_{1,2}$ sowie Winkel $\beta_{1,2}$ der Laufschaufeln, zusammensetzt, folgt ein iterativer Prozess zum Entwurf der Laufradgeometrie, damit die besprochenen Kriterien eingehalten werden. Die Druckerhöhung H wird aus den beschriebenen Pumpenparametern und einem geschätzten Wirkungsgrad η berechnet und muss der Physiologie des Herz-Kreislaufsystems entsprechen. Die Schätzung des Wirkungsgrades erfolgt durch die Analyse von Pumpen mit ähnlichen Dimensionen oder durch die Ergebnisse der nachfolgenden Simulation.

2.1 Pumpenentwurf

Bei einer neuen Pumpenauslegung muss eine Drehzahl vor Beginn des iterativen Prozesses (siehe Abbildung 2.1) angenommen werden. In Kombination mit dem benötigten Volumenstrom, der angenommenen Laufradgeometrie und einem geschätzten Wirkungsgrad wird die daraus resultierende Druckerhöhung berechnet. Gleicht der Wert nicht dem angestrebten Wert für H, ist die Drehzahl und/oder die Laufradgeometrie zu ändern, bis die geschätzte Druckerhöhung den Zielwert erreicht.

2.2 Pumpenvergleich

Um anhand eines bestehenden Pumpenentwurfes (Pumpe 1) eine geometrisch ähnliche Pumpe (Pumpe 2) auszulegen, werden zunächst die Parameter für die Berechnung der spezifischen Drehzahl und des spezifischen Durchmessers der Pumpe 1 benötigt (Q, H, n, d_2, z_{St}). Da für die anschließende Masterarbeit eine einstufige Pumpe mit demselben Volumenstrom Q und Druckerhöhung H der zu vergleichenden Pumpe zu entwerfen ist, werden durch die Bedingung der geometrischen Ähnlichkeit mit Hilfe von n_q und D_q die Drehzahl n und d_2 der Pumpe 2 berechnet. Basierend auf der berechneten Dimension d_2, wählt man die restlichen geometrischen Parameter des Laufrades und einen geschätzten Wirkungsgrad für die Pumpe 2 aus. Die weitere Berechnung ergibt eine geschätzte Druckerhöhung H, welche iterativ durch Änderung der Schaufelgeometrie an den Zielwert angepasst werden kann.

2.3 Entwurf des Spiralgehäuses

Das Spiralgehäuse kann nach der Berechnung des Laufrades entworfen werden. Die Querschnittsform des Spiralgehäuses wurde als kreisförmig festgelegt. Mit Hilfe von Gleichung 1.16 wird die Lage der Zunge in radialer Richtung berechnet. Es werden beide Lösungsansätze zur Berechnung des Flächenverlaufes des Spiralen-Querschnitts getrennt betrachtet und visuell dargestellt. Nach dem Vergleich der beiden Lösungen können konstruktive Entscheidungen getroffen werden.

2.4 Überprüfung nach Cordier

Zuletzt werden die aktuellen Werte für n_q und D_q in das Cordier- Diagramm (siehe Abbildung 1.5) eingetragen. Dies gibt Aufschluss, ob sich das Pumpenkonzept in dem Bereich besten Wirkungsgrades befindet.

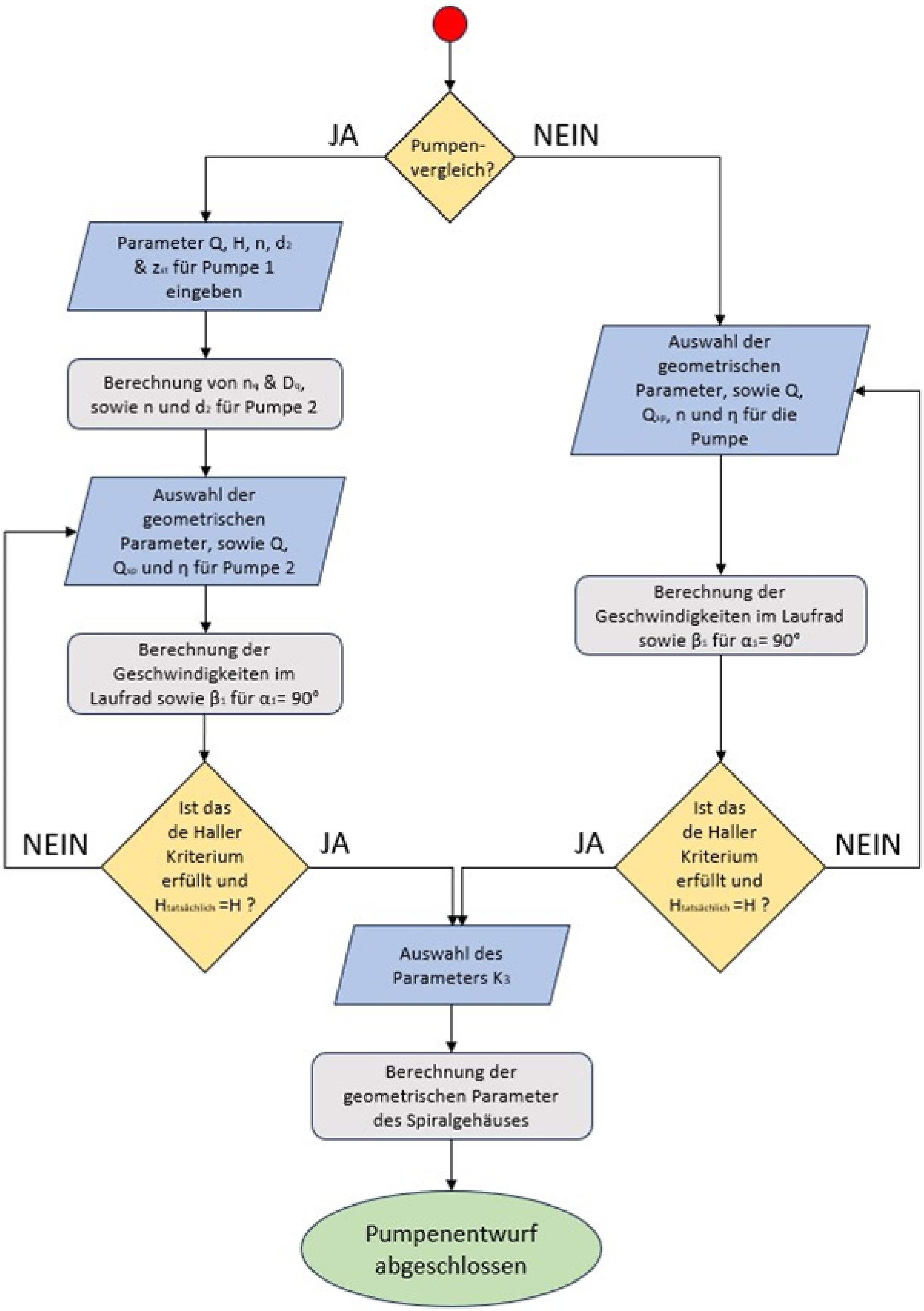

Abbildung 2.1: Flowchart zur Berechnung der Laufradgeometrie einer geometrisch ähnlichen Pumpe.

Kapitel 3

Resultate

3.1 Ergebnisse

In Abbildung 3.1 ist die Startseite des erstellten Berechnungsprogramms dargestellt. Dieses startet entweder mit dem Ausfüllen der „Eingabe Parameter Pumpe 1“ (Bereich 2) für den Zweck eines Pumpenvergleichs, oder direkt mit der „Eingabe Parameter Pumpe 2“ (Bereich 3) zur Auslegung eines neuen Pumpenentwurfs. Die Eingabe und die Ergebnisse der Berechnungen von Pumpe 1 können einfach durch Abwählen von „Pumpenvergleich“ (Bereich 1) ausgeblendet werden.

Nach dem Eintragen der Parameter der Pumpe 1 und der Betätigung des „Weiter“-Buttons, folgt die Ausgabe der Berechnung in „Ergebnisse Pumpe 1“. Hier werden die berechnete spezifische Drehzahl und der spezifische Durchmesser der Pumpe angezeigt. Zusätzlich wird, spezifisch für die anschließende Masterarbeit, die Drehzahl n und der äußere Durchmesser des Laufrades d_2 für eine einstufige Pumpe mit geometrischer Ähnlichkeit berechnet. Diese Berechnung folgt aus der Umformung der Gleichungen 1.3 und 1.6, mit der Annahme, dass die Werte für H, Q, n_q und D_q konstant bleiben.
Basierend auf den Ergebnissen von Pumpe 1, oder durch Wählen von eigenen Auslegungsparametern, werden die Werte in die „Eingabe Parameter Pumpe 2“ eingetragen. Klickt man auf „berechnen“ werden die Ergebnisse der neu ausgelegten Pumpe in „Ergebnisse Pumpe 2“ angezeigt. Im Bereich „Kriterien“ wird der Winkel β_1, welcher für eine drallfreie Anströmung zu verwenden ist, und der Wert für das de Haller- Kriterium des aktuellen Entwurfs angezeigt. Bei Erfüllung des de Haller-

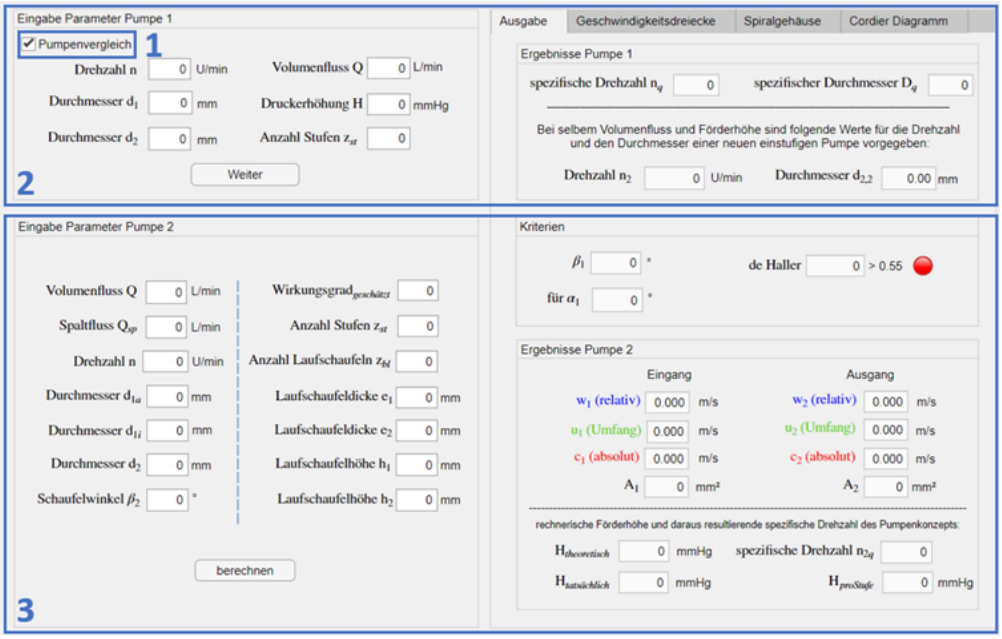

☑ Pumpenvergleich

Drehzahl n 0 U/min
Durchmesser d_1 0 mm
Durchmesser d_2 0 mm
Volumenfluss Q 0 L/min
Druckerhöhung H 0 mmHg
Anzahl Stufen z_{st} 0

spezifische Drehzahl n_q 0
spezifischer Durchmesser D_q 0

Bei selbem Volumenfluss und Förderhöhe sind folgende Werte für die Drehzahl und den Durchmesser einer neuen einstufigen Pumpe vorgegeben:

Drehzahl n_2 0 U/min
Durchmesser $d_{2,2}$ 0.00 mm

Volumenfluss Q 0 L/min
Spaltfluss Q_{sp} 0 L/min
Drehzahl n 0 U/min
Durchmesser d_{1a} 0 mm
Durchmesser d_{1i} 0 mm
Durchmesser d_2 0 mm
Schaufelwinkel β_2 0 °
Wirkungsgrad$_{geschätzt}$ 0
Anzahl Stufen z_{st} 0
Anzahl Laufschaufeln z_{bl} 0
Laufschaufeldicke e_1 0 mm
Laufschaufeldicke e_2 0 mm
Laufschaufelhöhe h_1 0 mm
Laufschaufelhöhe h_2 0 mm

β_1 0 °
für α_1 0 °
de Haller 0 > 0.55 🔴

	Eingang			Ausgang	
w_1 (relativ)	0.000	m/s	w_2 (relativ)	0.000	m/s
u_1 (Umfang)	0.000	m/s	u_2 (Umfang)	0.000	m/s
c_1 (absolut)	0.000	m/s	c_2 (absolut)	0.000	m/s
A_1	0	mm²	A_2	0	mm²

rechnerische Förderhöhe und daraus resultierende spezifische Drehzahl des Pumpenkonzepts:

$H_{theoretisch}$ 0 mmHg
$H_{tatsächlich}$ 0 mmHg
spezifische Drehzahl n_{2q} 0
$H_{proStufe}$ 0 mmHg

Abbildung 3.1: Startseite des Berechnungsprogramms für Rotationsblutpumpen.

Kriteriums ändert sich die Farbe der benachbarten Lampe von Rot auf Grün. Die Ergebnisse beinhalten die Geschwindigkeiten im Laufrad, die Querschnittsflächen von Laufradeintritt und -austritt, sowie die Druckerhöhungen $H_{theoretisch}$, $H_{tatsächlich}$ und $H_{proStufe}$. $H_{theoretisch}$ bezeichnet die verlustfreie Druckerhöhung durch das rotierende Laufrad und $H_{tatsächlich}$ gibt die tatsächliche Druckerhöhung, bei geschätztem Wirkungsgrad, an. $H_{proStufe}$ beschreibt, bei mehrstufiger Ausführung, die geschätzte Druckerhöhung je Pumpenstufe.
Im Reiter „Geschwindigkeitsdreiecke“ findet man die Vektordarstellung der berechneten Geschwindigkeiten in Form der besprochenen Geschwindigkeitsdreiecke für Eingang und Ausgang des Laufschaufelkanals (siehe Abbildung 3.2). Der Winkel α befindet sich zwischen der Absolut- und Umfangsgeschwindigkeit, der Winkel β befindet sich zwischen der Relativ- und Umfangsgeschwindigkeit.

Weiters wird im Reiter „Spiralgehäuse“ der theoretisch optimale Querschnittsverlauf des Spiralgehäuses berechnet (siehe Abbildung 3.3). Wie bereits erwähnt, werden die zwei gängigen Betrachtungsweisen (Drallerhaltung und konstante Geschwindigkeit) zur Berechnung verwendet. Zuallererst wird der Wert für K_3 abgefragt, welcher für die weitere Berechnung des Querschnittsverlaufs bei konstanter Geschwindigkeit benötigt wird. Klickt man auf „Auswahl“, öffnet sich ein weiteres Fenster, welches zur Auswahl des Parameters K_3 verwendet wird. In Abbildung 3.4 ist als Beispiel in

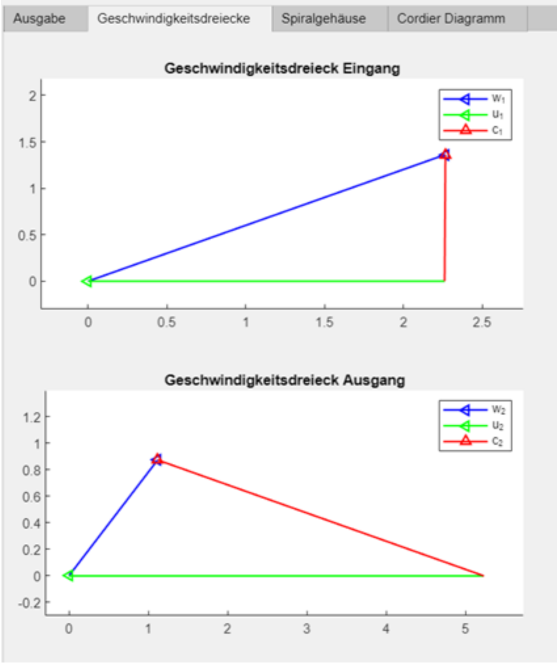

Abbildung 3.2: Darstellung der Geschwindigkeitsdreiecke des berechneten Laufradentwurfs.

Rot dargestellt, wie die spezifische Drehzahl in dem Diagramm an der Kurve für K_3 abgeschlagen und auf der Ordinate der Wert für den gesuchten Parameter abgelesen wird. Die Berechnung des Spiralgehäuses wird durch Klicken von „Spiralgehäuse entwerfen“ initiiert. Das leere Diagramm in Abbildung 3.3 wird nicht nur mit den berechneten Querschnittsflächen des Spiralgehäuses (in gedanklichen Schnitten bei 90°, 180°, 270° und 360°), sondern auch des Laufrades befüllt. Die dargestellten Querschnittsflächen des Laufrades stehen senkrecht zur Flussrichtung und befinden sich am Laufradeingang und -ausgang, jeweils direkt vor und nach den Laufschaufeln. Darunter werden der Durchmesser der Zungenposition und die Durchmesser des winkelabhängigen Kreisquerschnittes für das Spiralgehäuse angezeigt. Abbildung 3.5 veranschaulicht anhand eines Beispiels die Unterschiede in den Ergebnissen der Auslegungsbetrachtungen des Spiralgehäuses.

Zuletzt kann im Reiter „Cordier Diagramm“ eine finale Betrachtung der theoretischen Effizienz des Pumpenentwurfes erfolgen. In Abbildung 3.6 wird ein Beispiel eines solchen Entwurfes dargestellt. Im oberen Teil werden erneut die spezifische Drehzahl und der spezifische Durchmesser angeführt, um diese direkt in das Cordier Diagramm eintragen zu können. Nach dem Eintragen der Werte (hier exemplarisch in Rot dargestellt) wird der Betriebspunkt der konzipierten Pumpe ersichtlich.

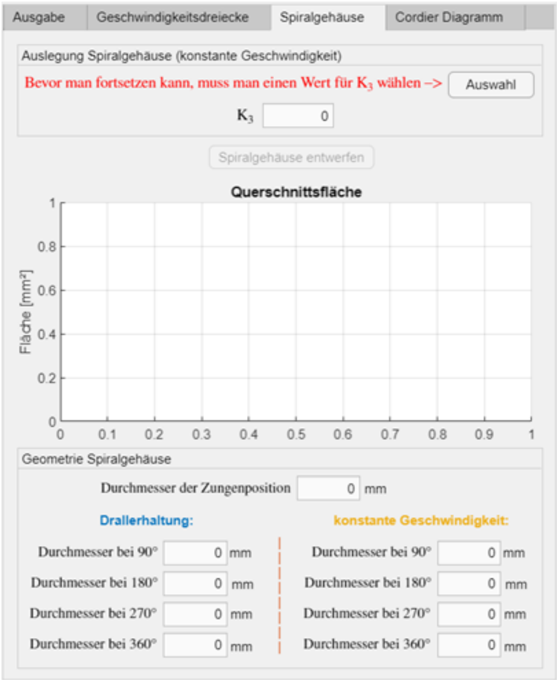

Bevor man fortsetzen kann, muss man einen Wert für K_3 wählen –>

K_3 0

Durchmesser der Zungenposition 0 mm

Drallerhaltung:		konstante Geschwindigkeit:	
Durchmesser bei 90°	0 mm	Durchmesser bei 90°	0 mm
Durchmesser bei 180°	0 mm	Durchmesser bei 180°	0 mm
Durchmesser bei 270°	0 mm	Durchmesser bei 270°	0 mm
Durchmesser bei 360°	0 mm	Durchmesser bei 360°	0 mm

Abbildung 3.3: Benutzeroberfläche für die Berechnung des Querschnittverlaufs des Spiralgehäuses.

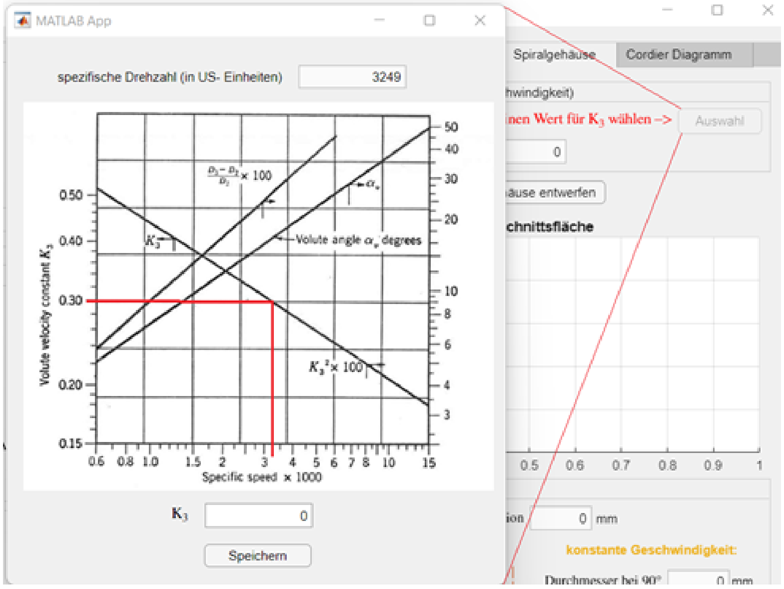

spezifische Drehzahl (in US- Einheiten) 3249

K_3 0

nen Wert für K_3 wählen –>

0

ion 0 mm

Durchmesser bei 90° 0 mm

Abbildung 3.4: Öffnen eines weiteren Fensters zur Auswahl der Konstante K_3.

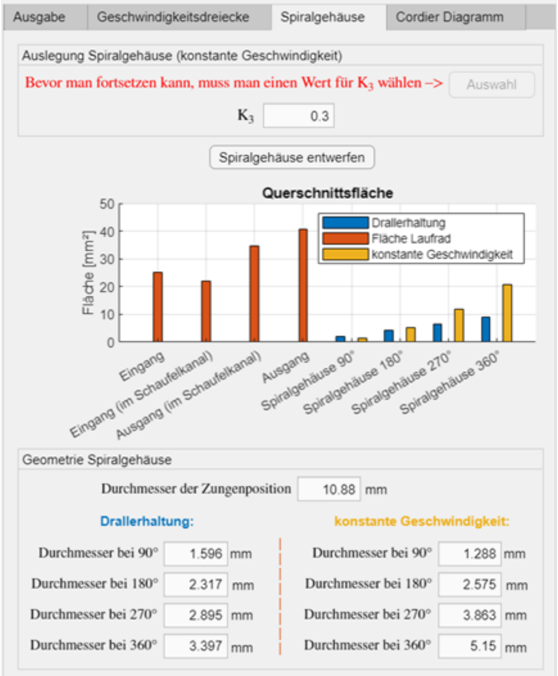

Auslegung Spiralgehäuse (konstante Geschwindigkeit)

Bevor man fortsetzen kann, muss man einen Wert für K_3 wählen –>

K_3 0.3

Geometrie Spiralgehäuse

Durchmesser der Zungenposition 10.88 mm

Drallerhaltung:		konstante Geschwindigkeit:	
Durchmesser bei 90°	1.596 mm	Durchmesser bei 90°	1.288 mm
Durchmesser bei 180°	2.317 mm	Durchmesser bei 180°	2.575 mm
Durchmesser bei 270°	2.895 mm	Durchmesser bei 270°	3.863 mm
Durchmesser bei 360°	3.397 mm	Durchmesser bei 360°	5.15 mm

Abbildung 3.5: Beispielentwurf eines Spiralgehäuses mit berechneten Durchmessern für die Querschnitte in den Positionen 90°, 180°, 270° und 360°, sowie graphischer Darstellung.

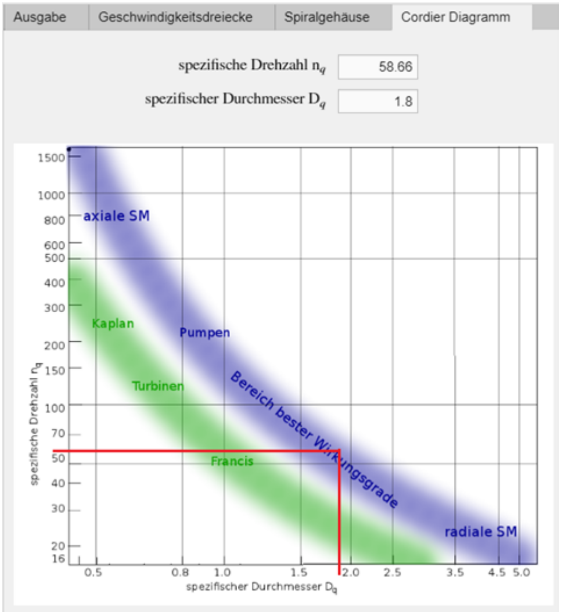

spezifische Drehzahl n_q 58.66

spezifischer Durchmesser D_q 1.8

Abbildung 3.6: Betrachtung der Effizienz der entworfenen Pumpe im Cordier Diagramm.

3.2 Diskussion

In dieser Projektarbeit wurde ein Berechnungsprogramm entwickelt, welches die Auslegung von Rotationsblutpumpen ermöglicht. Da der Entwurf von RBP ein iterativer Prozess ist, bietet dieses Programm eine effiziente computergestützte Hilfe zur Auswahl der geometrischen Abmessungen sowie der Betriebsparameter. Generell kann dieses Programm auch für die Berechnung von herkömmlichen Kreiselpumpen verwendet werden, da es auf deren theoretischer Grundlage beruht. Die detaillierte Betrachtung von RBP wird durch den variabel annehmbaren Spaltfluss Q_{Sp} und Wirkungsgrad η ermöglicht. Der Pumpenvergleich stellt eine Erweiterung des Programms dar, welches für die anschließende Masterarbeit Verwendung findet. Basierend auf einem bestehenden Pumpenkonzept gibt diese Option eine Empfehlung zur Auswahl der Dimension und der Drehzahl einer geometrisch ähnlichen Pumpe. Nach Auswahl der Pumpenparameter werden sowohl die Geschwindigkeiten am Eintritt und Austritt des Laufrades als auch die daraus resultierende Druckerhöhung berechnet und ausgegeben. Die Geschwindigkeiten werden, jeweils für den Eintritt und Austritt des Laufrades, graphisch in einem Geschwindigkeitsdreieck dargestellt. Weiters gibt das Programm die, auf das Laufrad abgestimmten, theoretisch optimalen Querschnittsgrößen des kreisförmigen Spiralgehäuses an. Zuletzt kann, mit Hilfe der Ausgabe der spezifischen Drehzahl und des spezifischen Durchmessers, der Betriebspunkt des Pumpenentwurfs in das Cordier- Diagramm eingetragen werden. Befindet sich der Punkt in dem bandförmigen Bereich im Diagramm, besitzt die betrachtete Pumpe nach Fister et al. den maximal möglichen Wirkungsgrad [8].

Jedoch basiert die Grundlage des Berechnungsprogramms auf einigen Annahmen und Erfahrungswerten. Die Schätzung des Wirkungsgrades und Spaltflusses führt zu Ungenauigkeiten in der Berechnung des Pumpenlaufrades. Diese Ungenauigkeiten können entweder durch Erfahrungswerte (bspw. Werte aus ähnlichen Forschungsarbeiten) oder Simulationsergebnisse minimiert werden. Die weiterführende Berechnung der Geschwindigkeiten stützt auf der Annahme der drallfreien Anströmung am Laufradeintritt. Ob sich die Strömung in der praktischen Anwendung ideal verhält muss in Versuchen ermittelt werden. Die Pumpe wird außerdem so konzipiert, dass das de Haller Kriterium (wenn möglich) erfüllt ist. Jedoch wurde der Grenzwert dieses Kriteriums mittels Gitterversuchen nach de Haller et al. ermittelt und in aktuelleren Forschungsarbeiten verändert [3, 6]. Ab welchem Grenzwert sich Strömungsablösungen in Rotationsblutpumpen entwickeln ist aber unklar. Zuletzt ist zu erwähnen, dass das Cordier- Diagramm im Jahr 1953 anhand der Messdaten von Versuchen an 120 unterschiedlichen Strömungsmaschinen (Ventilatoren, Verdichter und Pumpen) erstellt wurde [5]. Die Anwendbarkeit des Cordier- Diagramms auf die Größendimension von Rotationsblutpumpen wurde aber noch nicht erforscht.

Die auf das Blut wirkenden Scherspannungen, welche für die Hämokompatibilität von RBP entscheidend sind, können mit diesem Berechnungsprogramm nicht berechnet werden. Da die Scherspannungen durch die Geschwindigkeitsverhältnisse und Geometrie im betrachteten Ort der Pumpe beschrieben werden, werden diese in nachfolgenden Strömungssimulationen ermittelt. Weiters bietet das Programm keine Möglichkeit zur Berechnung von Stagnationszonen, welche die Thrombusbildung in der Pumpe begünstigen [2, 27]. Die Zonen niedriger Geschwindigkeit im Pumpenvolumen werden auch in den Ergebnissen der Strömungssimulationen veranschaulicht.

Das erstellte Berechnungsprogramm ist ein zuverlässiges Hilfsmittel zu der Auslegung von Pumpen. Dadurch wird eine Zeitersparnis im Vergleich zu der manuellen Berechnung erzielt, besonders bei iterativen Anpassungen der Geometrie. Außerdem bietet die Übersicht der berechneten Parameter eine strukturierte Veranschaulichung der Ergebnisse. Der spezielle Anwendungsfall der Blutförderung wird ermöglicht, wenn der Wirkungsgrad und der Spaltstrom entsprechend angepasst werden. Weiters gibt die graphische Darstellung der Geschwindigkeitsdreiecke Einblick auf das Strömungsverhalten im Laufrad der Pumpe. Mit Hilfe der berechneten optimalen Querschnittsflächen des Spiralgehäuses, wird die Konstruktion einer möglichst effizienten Pumpe erleichtert.

Dieses Berechnungsprogramm, einschließlich der optionalen Funktion des Pumpenvergleichs, hat bereits Verwendung für die anschließende Masterarbeit gefunden. Die iterative Anpassung des initialen Pumpenentwurfes, basierend auf den Simulationsergebnissen, wurde mit Hilfe des Programms erleichtert. Nach dem aktuellen Stand gibt es keine vergleichbaren Berechnungsprogramme für Rotationsblutpumpen.

Literatur

[1] Almond, C. S., Singh, T. P., Gauvreau, K., Piercey, G. E., Fynn-Thompson, F., Rycus, P. T., Bartlett, R. H. und Thiagarajan, R. R. (2011). Extracorporeal Membrane Oxygenation for Bridge to Heart Transplantation Among Children in the United States. *Circulation 123*, 2975–2984.

[2] careship Thrombose: Ursache, Symptome und Behandlung https://www.careship.de/senioren-ratgeber/thrombose/#:~:text=Die%20Virchow%2DTrias%20setzen%20sich,Str%C3%B6mungsgeschwindigkeit%20(durch%20Krampfadern%20oder%20Bettl%C3%A4gerigkeit) (besucht am 1. Aug. 2023).

[3] Carolus, T., *Ventilatoren*, 3. Auflage; Springer: 2012.

[4] Conway, J., St. Louis, J., Morales, D. L., Law, S., Tjossem, C. und Humpl, T. (2015). Delineating Survival Outcomes in Children <10 kg Bridged to Transplant or Recovery With the Berlin Heart EXCOR Ventricular Assist Device. *JACC: Heart Failure 3*, 70–77.

[5] Cordier, O., *Ähnlichkeitsbedingungen für Strömungsmaschinen*; BWK Band 5, Nr. 10: 1953.

[6] de Haller, P., *Das Verhalten von Tragflügelgittern in Axialverdichtern und im Windkanal.* BWK: 1953.

[7] Dipchand, A. I. und Laks, J. A. (2020). Pediatric heart transplantation: long-term outcomes. *Indian journal of thoracic and cardiovascular surgery 36*, 175–189.

[8] Fister, W., *Fluidenergiemaschinen*, Band 1: Physikalische Voraussetzungen, Kenngrößen, Elementarstufen der Strömungs- und Verdrängermaschinen.; Springer: 1984.

[9] Flexikon, D. Hämostase https://flexikon.doccheck.com/de/Blutgerinnung (besucht am 20. Juni 2023).

[10] Flexikon, D. Herzinsuffizienz https://flexikon.doccheck.com/de/Herzinsuffizienz (besucht am 20. Juni 2023).

[11] Flexikon, D. Thromboembolie https://flexikon.doccheck.com/de/Thromboembolie (besucht am 20. Juni 2023).

[12] for Disease Control, C. und Prevention WHO Growth Standards Are Recommended for Use in the U.S. for Infants and Children 0 to 2 Years of Age https://www.cdc.gov/growthcharts/who_charts.htm#print (besucht am 10. Juli 2023).

[13] Fox, C., Sarkisyan, H., Stevens, R., Arabia, F., Fischer, W., Rossano, J. und Throckmorton, A. (2019). New versatile dual-support pediatric heart pump. *Artificial organs 43*, 1055–1064.

[14] Fraser, K. H., Zhang, T., Taskin, M. E., Griffith, B. P. und Wu, Z. J. (2012). A Quantitative Comparison of Mechanical Blood Damage Parameters in Rotary Ventricular Assist Devices: Shear Stress, Exposure Time and Hemolysis Index. *Journal of Biomechanical Engineering 134*, 081002.

[15] Groenewegen, A., Rutten, F. H., Mosterd, A. und Hoes, A. W. (2020). Epidemiology of heart failure. *European Journal of Heart Failure 22*, 1342–1356.

[16] Gross-Hardt, S., Hesselmann, F., Arens, J. et al. (2019). Low-flow assessment of current ECMO/ECCO2R rotary blood pumps and the potential effect on hemocompatibility. *Crit Care 23*, DOI: https://doi.org/10.1186/s13054-019-2622-3.

[17] Gülich, J. F., *Kreiselpumpen, Handbuch für Entwicklung, Anlagenplanung und Betrieb*, 4. Auflage; Springer: 2013.

[18] Heart, B. EXCOR PEDIATRIC: Das Herzunterstützungssystem für junge Patienten https://www.berlinheart.de/patienten-angehoerige/excorr-pediatric/ (besucht am 13. Juli 2023).

[19] Hudson I, Houston A, Aitchison T, Holland B, Turner T. (1990). Reproducibility of measurements of cardiac output in newborn infants by Doppler ultrasound. *Archives of disease in childhood 65,1*, DOI: 10.1136/adc.65.1_spec_no.15.

[20] Jones, N. R., Roalfe, A. K., Adoki, I., Hobbs, F. R. und Taylor, C. J. (2019). Survival of patients with chronic heart failure in the community: a systematic review and meta-analysis. *European Journal of Heart Failure 21*, 1306–1325.

[21] Kapadia JY, Pierce KC, Poupore AK, Throckmorton AL. (2010). Hydraulic testing of intravascular axial flow blood pump designs with a protective cage of filaments for mechanical cavopulmonary assist. *ASAIO journal (American Society for Artificial Internal Organs : 1992) 56,1*, DOI: 10.1097/MAT.0b013e3181c5b046.

[22] Mehra, M. R., Naka, Y., Uriel, N., Goldstein, D. J., Cleveland, J. C., Colombo, P. C., Walsh, M. N., Milano, C. A., Patel, C. B., Jorde, U. P., Pagani, F. D., Aaronson, K. D., Dean, D. A., McCants, K., Itoh, A., Ewald, G. A., Horstmanshof, D., Long, J. W. und Salerno, C. (2017). A Fully Magnetically Levitated Circulatory Pump for Advanced Heart Failure. *New England Journal of Medicine 376*, PMID: 27959709, 440–450.

[23] Nicola, S.-S. Fortgeschrittene Herzinsuffizienz: Mehr als die Hälfte der Patienten überleben mit magnetischer Herzpumpe 5 Jahre https://www.aerzteblatt.de/archiv/228114/Fortgeschrittene-Herzinsuffizienz-Mehr-als-die-Haelfte-der-Patienten-ueberleben-mit-magnetischer-Herzpumpe-5-Jahre (besucht am 4. Juli 2023).

[24] Obidowski, D., Reorowicz, P., Witkowski, D., Sobczak, K. und Jóźwik, K. (2018). Methods for determination of stagnation in pneumatic ventricular assist devices. *The International Journal of Artificial Organs 41*, PMID: 30073903, 653–663.

[25] Pfleiderer, C., *Strömungsmaschinen*, 7. Auflage; Springer: 2005.

[26] Reiss, N. (2013). Herztransplantation vs. Destination-Therapie. *Zeitschrift für Herz-, Thorax- und Gefäßchirurgie 27*, 302–307.

[27] Smith, P. A., Wang, Y., Groß-Hardt, S. und Graefe, R., Chapter 10 - Hydraulic design in *Mechanical Circulatory and Respiratory Support*, Gregory, S. D., Stevens, M. C. und Fraser, J. F., Hrsg.; Academic Press: 2018, S. 301–334.

[28] Stepanoff, A. J., *centrifugal and axial flow pumps : theory, design, and application*, 2nd edition; KRIEGER PUBLISHING COMPANY: 1957.

[29] Throckmorton AL, Kapadia JY, Chopski SG, et al. (2011). Numerical, hydraulic, and hemolytic evaluation of an intravascular axial flow blood pump to mechanically support Fontan patients. *Annals of biomedical engineering 39,1*, DOI: 10.1007/s10439-010-0159-3.

[30] Vieira JL, M. M., Ventura HO (2020). Mechanical circulatory support devices in advanced heart failure: 2020 and beyond. *Progress in cardiovascular diseases*, DOI: 10.1016/j.pcad.2020.09.003.

[31] Winkhardt, M., *Das Herzkatheterlabor, Für kardiologisches Assistenz- und Pflegefachpersonal*, 3. Auflage; Springer: 2017.

[32] Woolley, J. R. e. a. (2013). First Berlin heart EXCOR pediatric VAD interhospital transports of nonambulatory patients with the Ikus stationary driver. *ASAIO journal (American Society for Artificial Internal Organs : 1992) 59,5*, DOI: 10.1097/MAT.0b013e31829e66d7.

[33] Wu J, F. Antaki J, Verkaik J, Snyder S, Ricci M. (2012). Computational Fluid Dynamics-Based Design Optimization for an Implantable Miniature Maglev Pediatric Ventricular Assist Device. *Journal of Fluids Engineering 134,4*, DOI: 10.1115/1.4005765.